

Direct-current Triboelectricity Generation by Electron Tunneling Transport

by

Jun Liu

A thesis submitted in partial fulfillment of the requirements for the degree of

Doctor of Philosophy

In

Materials Engineering

Department of Chemical and Materials Engineering
University of Alberta

© Jun Liu, 2018

Abstract

The direct conversion of mechanical energy into electricity by nanomaterial-based devices offers potential for green energy harvesting. One of the main challenges for mechanical energy harvesting technologies, such as piezoelectric or triboelectric generators, is to provide sufficient current density for powering electronics, which is generally limited by the high impedance of material systems. A conventional triboelectric nanogenerator converts frictional energy into electricity by producing alternating current (a.c.) triboelectricity. However, this approach is limited by low current density and the need for rectification. In this thesis, we show that continuous direct-current (d.c.) with a maximum density of 10^6 A m^{-2} can be directly generated by a sliding Schottky nanocontact without the application of an external voltage. We demonstrate this by sliding a conductive-atomic force microscope tip on a thin film of molybdenum disulfide (MoS_2). Finite element simulation reveals that the anomalously high current density can be attributed to the non-equilibrium carrier transport phenomenon enhanced by the strong local electrical field ($10^5\text{--}10^6 \text{ V m}^{-2}$) at the conductive nanoscale tip. We hypothesize that the charge transport may be induced by electronic excitation under friction, and the nanoscale current-voltage spectra analysis indicates that the rectifying Schottky barrier at the tip-sample interface plays a critical role in efficient d.c. energy harvesting.

Furthermore, we have observed sustainable tunneling current generation at an unbiased, triboelectrically charged metal-insulator-semiconductor (MIS) point contact consisting of p-type silicon, silicon oxide and a metal tip. It is found that the native thin oxide ($\sim 1.6 \text{ nm}$) on the silicon surface provides a natural pathway for the quantum mechanical tunneling of triboelectric charges. The charges are then collected by the semiconducting substrate, thereby generating

direct current (d.c.) with very high current density. The measured direct current (d.c.) shows an exponential decay with the thickness of oxide layer deposited with atomic layer deposition (ALD), confirming the quantum mechanical tunneling mechanism. It is proposed that the contact potential difference enhanced by triboelectric charging provides the potential difference between metal point contact and the substrate. With single metallic micro probe sliding on a moderately doped p-type silicon, an open circuit voltage (V_{oc}) of 300-400 mV and a short-circuit direct current (I_{sc}) of 3-5 μ A (a corresponding high current density, J , in the order of 1-10 A/m^2) have been observed. It is predicted by conductive-atomic force microscopy (C-AFM) experiment that the theoretical J can be as high as $10^4 A/m^2$. It has been proved that the d.c. triboelectricity generation by MIS frictional contact can be directly stored by charging capacitors. This concept has the potential as a green energy harvesting technique where a broad range of material candidates and device configurations could be used.

Preface

This thesis is an original work conducted by Jun Liu (Liu, J.) and under the supervision of Dr. Thomas Thundat (Thundat, T.).

Chapter 3 of this thesis has been published as Jun Liu, Ankur Goswami, Keren Jiang, Faheem Khan, Seokbeom Kim, Ryan McGee, Zhi Li, Zhiyu Hu, Jungchul Lee, and Thomas Thundat. "Direct-current triboelectricity generation by a sliding Schottky nanocontact on MoS₂ multilayers" *Nature nanotechnology* 13, no. 2 (2018): 112. J.Liu, K.J. and T.T. conceived the C-AFM study. A.G., R.McG. and J. Liu carried out the PLD synthesis of sample. F.K. and J.Liu designed and carried out the macroscale demonstration. Z.L. prepared the exfoliated MoS₂ sample and conducted Raman measurements. J.Liu performed FEM simulations. J.Liu, J.Lee and T.T. co-wrote the manuscript. S.K., J.Lee, and Z.H. helped with data analysis. All authors contributed to discussions.

Chapter 4 of this thesis has been published as Jun Liu, Mengmeng Miao, Keren Jiang¹, Faheem Khan¹, Ankur Goswami¹, Ryan McGee¹, Zhi Li, Lan Nguyen, Zhiyu Hu, Jungchul Lee, Ken Cadien and Thomas Thundat, "Sustained electron tunneling at unbiased metal-insulator-semiconductor triboelectric contacts", *Nano Energy* 48 (2018) 320–326. J.Liu, T.T. conceived the study. M. Miao carried out the ALD synthesis of sample. J.Liu and K.J. designed and carried out the C-AFM experiment and macroscale demonstration. All authors contributed to discussions.

“What made you to achieve success?” the reporter asked,

“Have you ever seen the scene of Los Angeles at 4 a.m.?”

---Kobe Bryant

Dedication to

The lovely Miss *Wanling Gu* & our adorable little friend *Jun-Jun*, for their courageous, selfless, and heartfelt company on this journey

Acknowledgements

First and foremost, I would like express my sincerest gratitude to my supervisor, Dr. Thomas Thundat, who has supported me throughout my PhD study with his amazing vision, immense knowledge, and great inspiration. I attribute the quality of my work as well as the level of my PhD degree to his patience, encouragement, enthusiasm, and motivation. As a young graduate student grew up in a conservative eastern culture, I have witnessed a huge transformation of myself from a passive leaner and follower, to an active and innovative discoverer with the spirit of adventure, the curiosity of observation, and the skill of critical thinking. These, without the great help and instruction from Dr. Thundat, would definitely never take place.

I offer my sincerest appreciation to all of our collaborators from/outside UofA, including Dr. Jungchul Lee from Sogang University in Korea, Prof. Zhiyu Hu from Shanghai Jiaotong University, Dr. Siddhartha Das from University of Maryland, and Prof. Ken Cadien & Prof. Jingli Luo from our department. Thank you very much for making our research work extraordinary. To my committee members, Dr. Jingli Luo, Dr. Natalia Semagina, and Dr. Shenqiang Ren, thanks a lot for your time and efforts for improving the quality of this thesis. For the great support of our research work, I would like to acknowledge the funding agencies: Canada Excellent Research Chair (CERC), Albert Innovate-Technology Future (AITF) Graduate Scholarship, and Captain Thomas Farrell Greenhalgh Memorial Graduate scholarship.

Rome was not built in a day, or with a man along. I would like to thank all my lab mates, Dr. Keren Jiang, Dr. Faheem Khan, Dr. Ankur Goswami, Dr. Zhi Li, Dr. Ravi Gaikwad, Dr. Tinu Abraham, Dr. Raj Naicker, Dr. Priyesh Dhandharia, Dr. Ryan McGee, Miss Yaqian Zhang, Mr. Inseok Chae and many others, for their great help and collaboration during my research in the lab, and sharing a lot of happiness and fun in the tedious research life. Specially, many thanks go to

the secretary of Dr. Thundat, Ms. Josie Nebo, departmental graduate assistant Ms. Lily Laser and Dr. Vinay Prasad, for their tremendous assistance in my PhD study.

I would also like to thank my student Miss Lan Nguyen and Mr. David Scott for helping with my experiments, the co-op undergraduates Miss Rebecca Kostiuk and Miss Allison Larocque for grabbing my shoes all the time (I still don't know why they have to do that...), and my office mate Mr. Darren Majak. Mr. Majak could have earned a better life in Hollywood with his beauty, but he decided to pursue a master degree in engineering. My roommates, Dr. Shuai Guo and Mr. Duanshun Li, and many other friends I met in Edmonton, thanks for leaving me a lot of great memory in these years, and I wish all of you guys have a bright future.

I would like to say thank you to my parents, Mr. Shengtao Liu and Mrs. Ping Zhang, for their great patience, sacrificing, and encouragement. Words cannot deliver my gratitude to their understanding and support on this journey. I believe, the best way to make up for my missing days with you in the past ten years, during which I have been far away from home pursuing my dream, is to grow into a great man you will be proud of. I would also like to thank my grandparents Mr. Guanhui Liu (R.I.P.) and Mrs. Xiao-e Cai (R.I.P.), for enlightening my dream on my early ages, and blessing me from heaven after they passed away.

My special thanks go to the amazing lady Miss Wanling Gu, who, without hesitation, fell in a ten-thousand-miles' distance relationship with me. I would never forget the days and nights we cheered each other from a small cellphone screen, saving money for air tickets and counting down the days left for reunion. I would like to thank her for helping me nail through the darkest nights on this journey, and I want her to know that she is part of my soul, ever forever, no matter what.

Table of Contents

Abstract.....	ii
Preface.....	iv
Acknowledgements	vi
Table of Contents	viii
List of Figures.....	xii
List of Publication during PhD Study.....	xix
Chapter 1 Introduction.....	1
1.1 The fundamentals of energy harvesting.....	1
1.2 Nano/micro mechanical energy harvesting technologies	4
1.2.1 Electromagnetic nano/micro energy harvesting.....	6
1.2.2 Piezoelectric nano/micro energy harvesting	8
1.2.3 Electrochemistry-based nano/micro mechanical energy harvesting.....	11
1.2.4 Triboelectric nano/micro energy harvesting	12
1.3 Charge transfer in frictional contact system	19
1.3.1 Theories of contact electrification	20
1.3.1.1 Metal-metal contact system	22
1.3.1.2 Metal-insulator contact system	25
1.3.1.3 Insulator-insulator contact system	31
1.3.1.4 Identical material contact system.....	34
1.3.2 AFM study of contact electrification	34
1.4 Energy dissipation in friction.....	41
Chapter 2 Methodology and experimental section	45

2.1	Material synthesis	45
2.1.1	Synthesis of MoS ₂ thin film by pulsed laser deposition (PLD)	45
2.1.2	Synthesis of SiO _x by Atomic layer deposition (ALD).....	46
2.1.3	Preparation of electrical contact by magnetron sputtering	48
2.2	Material Characterization.....	49
2.2.1	Scanning electron microscopy (SEM) characterization.....	49
2.2.2	Raman spectra characterization	51
2.2.3	X-ray photoelectron spectroscopy (XPS) characterization.....	52
2.3	Conductive-atomic force microscopy (C-AFM) characterization	54
2.3.1	AFM operation.....	54
2.3.2	Determine Cantilever Spring Constant by Thermal Tune	57
2.3.3	C-AFM measurement.....	59
2.3.4	Probe-sample contact area estimation.....	64
2.4	Finite Element Method (FEM) simulation.....	69
2.5	Electrical measurement of the generator performance	69
2.5.1	V , I and P output as a function of load resistance R	69
2.5.2	Charging capacitor with DC triboelectricity.....	70
Chapter 3 Direct-current triboelectricity generation by sliding-Schottky nanocontact on MoS₂ multilayers		71
3.1	Introduction.....	72
3.2	Characteristics of C-AFM current output	74
3.3	Artifact exclusion.....	76
3.3.1	Current amplifier calibration.....	76
3.3.2	False engagement.....	77
3.3.3	Laser spot position	77
3.4	C-AFM measurement on other materials.....	78

3.4.1	Ag and SiO ₂	79
3.4.2	p-type Si	79
3.4.3	PEG polymer.....	80
3.5	In-situ C-AFM <i>I-V</i> characterization.....	82
3.6	C-AFM <i>I-V</i> data analysis	89
3.7	Voltage output and electric field characteristics.....	93
3.8	The proposed charge transfer mechanism.....	96
3.9	Contact force-dependent C-AFM current output.....	98
3.10	Scan number- and velocity-dependent C-AFM current output.....	103
3.11	C-AFM measurement on the exfoliated MoS ₂ sample	105
3.12	Conclusion	106
Chapter 4 Sustained electron tunneling at unbiased metal-insulator-semiconductor triboelectric contacts.....		108
4.1	Introduction.....	109
4.2	Current output characteristics of the MIS triboelectric contact	110
4.2.1	C-AFM current mapping.....	110
4.2.2	Macroscale current generation	114
4.2.3	Oxide thickness-dependent current output.....	116
4.3	Voltage output characteristics of the MIS triboelectric contact.....	118
4.3.1	Macroscale voltage output	118
4.3.2	Bias-dependent C-AFM current output	121
4.3.3	Oxide thickness-dependent voltage output	122
4.4	Influence of metal work function on V_{oc} direction	123

4.5	Si doping type/concentration-dependent V_{oc} output	126
4.6	Discussion of tribo-tunneling transport mechanism	127
4.7	Conclusion	129
Chapter 5 Scaling-up of the tribo-tunneling concept for practical application		130
5.1	Macro-scale demonstration of d.c. generation on MoS ₂ sample	130
5.2	Power generation with silicon-based tribo-tunneling system	132
5.2.1	V, I, P output vs. electric load R	132
5.2.2	Doping type/concentration-dependent V, I, P output vs. electric load R	135
5.2.3	Charging capacitor with d.c. triboelectricity.....	137
5.2.4	Automatic motor system.....	139
5.2.5	Design and fabrication of tip array system	141
Chapter 6 Conclusion and future work		144
6.1	Conclusion	144
6.2	Future work.....	146
Bibliography		147

List of Figures

Figure 1-1 Projection of global energy consumption by energy source	2
Figure 1-2 Magnitude of power and its corresponding applications	5
Figure 1-3 A hexagonal unit cell with non-symmetry crystal structure.	9
Figure 1-4 The four fundamental modes of triboelectric nanogenerators	15
Figure 1-5 Classical electromagnetic generator vs triboelectric nanogeneraotor	17
Figure 1-6 Energy band diagram of metal-metal system before and after contact.	22
Figure 1-7 Schematic indication of the variation of capacitance (C) and resistance (R) between two metal surfaces as a function of their separation z	23
Figure 1-8 Charge on a Cr sphere after contact with a sphere of another metal, plotted against the contact potential difference (V_{CPD}) between the metal and Cr.....	25
Figure 1-9 Surface states and contact electrification	26
Figure 1-10 Potential energy of an electron as a function of the distance x from the centre of a trap in the insulator	29
Figure 1-11 Two-way charge transfer between HOMO (donor) and LUMO (acceptor)	31
Figure 1-12 Possible scenarios of contact electrification and experimental KFM surface potential maps.	36
Figure 1-13 Triboelectric charge generation by friction between AFM probe and SiO_2	37
Figure 1-14 Patterning of the surface triboelectric charges on an insulator surface.....	38
Figure 1-15 Surface potential distributions of the Parylene film including the areas that were rubbed by Pt coated AFM tip at different bias.....	39
Figure 1-16 Polarization switching and surface potential distribution of the P(VDF-TrFE) thin film.....	40

Figure 1-17 Prandtl-Tomlinson model: A point mass in a periodic potential.	42
Figure 1-18 Different energy dissipation in friction	43
Figure 2-1 Pulsed laser deposition system (left); Working principle of PLD (right).	46
Figure 2-2 Schematics of the PEALD SiO _x deposition process	47
Figure 2-3 Electron beam evaporation system (left); Working principle of electron beam evaporation system (right).	48
Figure 2-4 Magnetron sputtering system (left); Working principle of magnetron sputtering system (right).	49
Figure 2-5 SEM image of MoS ₂ thin film deposited by PLD.....	50
Figure 2-6 3D layer structure of MoS ₂	50
Figure 2-7 Wulff construction for a MoS ₂ nanocluster exposing the (0001) basal plane	51
Figure 2-8 Raman spectra of MoS ₂ thin film deposited by PLD	52
Figure 2-9 Decomposition XPS peaks of MoS ₂ thin film deposited by PLD.....	53
Figure 2-10 Illustration of an AFM cantilever system.....	54
Figure 2-11 The effect of tip-to-sample distance on the force interaction between tip and sample	55
Figure 2-12 Illustration of a basic AFM system	56
Figure 2-13 Thermal tune of the AFM cantilever.....	59
Figure 2-14 Tunneling AFM (and Conductive AFM) Block Diagram.....	60
Figure 2-15 Bruker Icon C-AFM system with TUNA module.....	61
Figure 2-16 Bruker DTRCH-AM tip holder for TUNA module	62
Figure 2-17 SEM image of ACCESS-EFM Pt/Ir-coated conductive AFM tip from AppNano, US.	62

Figure 2-18 Schematic of Hertz model.....	64
Figure 2-19 Schematic of JKR model.....	65
Figure 2-20 Schematic of DMT model.....	66
Figure 2-21 Force curves and information that can be obtained from them.....	68
Figure 2-22 Electrical testing platform.....	70
Figure 3-1 (a) Working principle of conventional TENGs considering a metal-insulator system. (b) Schematic of nanoscale DC harvesting.....	73
Figure 3-2 (a) and (c) are AFM topographic images of MoS ₂ thin films at different scales and their corresponding C-AFM current mapping in (b) and (d). (e) Cross-sectional line analysis of the tribo-excited current on (d (marked by white dashed line))......	75
Figure 3-3 <i>I-V</i> characterization with a 100 MΩ standard calibration resistor.	76
Figure 3-4 C-AFM current signal under false engagement.....	77
Figure 3-5 Laser position-dependent C-AFM signal on MoS ₂	78
Figure 3-6 C-AFM current measured on (a) Ag sample and (b) SiO ₂ sample.	79
Figure 3-7 C-AFM measurement on p-type Si. (a) Topography and (b) current map.....	80
Figure 3-8 C-AFM current measured on spin-coated PEG polymer thin film on Au substrate. (a) Topography and (b) current map.	81
Figure 3-9 Cyclic <i>I-V</i> measurement on the PLD-synthesized MoS ₂ /Ag sample using probe station. (a) Sample surface in direct contact with Cu probe. (b) Pt/Cr top electrode was deposited in advance and in contact with the Cu probe.	83
Figure 3-10 (a) AFM topographic image of three adjacent MoS ₂ crystal grains marked as 1, 2, and 3. Their corresponding C-AFM current map is shown in (b).	84
Figure 3-11 Cross-sectional line analysis of the current as marked on 3-10(b).....	84

Figure 3-12 C-AFM I - V spectra on grains 1.....	85
Figure 3-13 C-AFM I - V spectra on grains 2.....	86
Figure 3-14 C-AFM I - V spectra on grains 3.....	87
Figure 3-15 (a) AFM topographic image of one MoS ₂ grain and its (b) corresponding C-AFM current map. (c) and (d) shows the I - V spectra of the location #1-14 as marked in (b).....	88
Figure 3-16 (a) Forward I - V spectrum (#1-9) fitted with thermionic emission model (Eq. 3-1). (b) Reverse I - V spectrum (#10-18) fitted with thermionic emission model. (c) Estimated ideality factor n and energy barrier Φ_B from fitting result in (b).....	91
Figure 3-17 C-AFM current map on the single crystal grain in Fig. 1c with the sample bias V of (a) -2 mV, (b) 0 mV, (d) 7 mV, (e) 8 mV, and (f) 10 mV.	94
Figure 3-18 (a) Simulated electric field distribution at the tip-sample interface. (b) 2D Model for finite element modeling. (c) Line analysis of electric field E vs. distance to tip d at the tip-sample interface simulated by FEM.....	95
Figure 3-19 Energy band diagram of the tip-sample interfaces and the proposed charge transfer mechanism.	97
Figure 3-20 (a) Tip-sample adhesion mapping of MoS ₂ . (b) Histogram of the adhesion distribution. (c) Typical force curve in PeakForce QNM measurement.....	99
.....	100
Figure 3-20 (a) and (b) are AFM cantilever force F vs. Piezo-scanner position Z and C-AFM current I vs. Z , respectively. (c) and (d) are their corresponding graphs in time domain.	102
Figure 3-21 (a) Topography of MoS ₂ sample and (b-f) its corresponding current output for multiple scans (#1-5). (g) Average and peak C-AFM current as a function of scan #.	104
Figure 3-22 Velocity-dependent C-AFM current data.....	104

Figure 3-23 (a) AFM topographic image of exfoliated MoS₂ layers and (c) corresponding C-AFM current map. (b) and (d) show line analysis labeled in (a) and (c), respectively. (e) and (f) are optical microscope images of the scan area of (a) and (g), respectively. (g) AFM topographic image of the silver paste-MoS₂ boundary. From line analysis in (h), atomic layer thickness can be seen..... 106

Figure 4-1 Schematic of C-AFM characterization of triboelectric current generation..... 111

Figure 4-2 Force-dependent current signal. 112

Figure 4-3 (a) The distance of probe-Si/SiO_x interface d_0-d_{indent} and contact area A as a function of applied force F (modeled by DMT theory, see Methods for details). (b) Average C-AFM current density J_{ave} as a function of d_0-d_{indent} . The dashed line is the exponential decay fitting result..... 113

Figure 4-4 (a) Schematic of the macroscale MIS frictional contact system. (b) and (c) shows the linearly reciprocating and circularly rotating modes, respectively. 115

Figure 4-5 (a) and (b) shows short-circuit current (I_{sc}) under the linearly reciprocating mode and the circularly rotating modes, respectively. 116

Figure 4-6 I_{sc} vs. d . Silicon samples with different surface oxide thickness were prepared by atomic layer deposition (ALD). 117

Figure 4-7 Open-circuit voltage (V_{oc}) under (a) a linearly reciprocating mode and (b) a circularly rotating modes, respectively. 118

Figure 4-8 Band diagrams of MIS frictional contact under (a) non-equilibrium, $\Phi_{\text{m}} > \Phi_{\text{s}}$ and (b) equilibrium, $\Phi_{\text{m}} > \Phi_{\text{s}}$ 120

Figure 4-9 Bias voltage-dependent current maps.. 121

Figure 4-10 Band diagrams of MIS frictional contact under external bias..... 122

Figure 4-11 Oxide-dependent open-circuit voltage out and local electric field	123
Figure 4-12 V_{oc} output for probes made of different metallic materials (a) Cu, (b) Au, and (c) Al.	125
Figure 4-13 Si doping type/concentration-dependent V_{oc} output.....	126
Figure 5-1 Manually driven system (a) Schematic of the setup. (b) Optical microscopy image of the connector front.	131
Figure 5-2 V and I output as a function of electrical load R . The solid curves for V and I are the fitting results by Eq. 5-2 and 5-3, respectively.	133
Figure 5-3 J and power density as a function of R . The power output (P) vs. R is fitted with Eq. 5-4 in Methods.	134
Figure 5-4 V across electrical load R with 10 M Ω , 400 k Ω , 100 k Ω and 20 k Ω recorded by an oscilloscope.....	135
Figure 5-5 I output as a function of electrical load R with different p type-Si doping concentration.....	136
Figure 5-6 V output as a function of electrical load R with different p type-Si doping concentration.....	137
Figure 5-7 (a) Schematic of the testing I-V testing system; (b) I-V curve of the MIS structure	138
Figure 5-8 Time-dependent voltage built-up of a capacitor C (80 μ F) charged by the d.c. triboelectricity.....	139
Figure 5-9 Controlling system for the automatic motor	140
Figure 5-10 A homemade automatic motor system; The contact force and sliding speed can be controlled by a spring-connected probe and the motor, respectively.	140

Figure 5-11 (a) Triboelectric voltage output (top) and its corresponding motor drive voltage vs. time (bottom) 141

Figure 5-12 A prototype of tip array system..... 142

Figure 5-13 3D printed tip array system 143

List of Publication during PhD Study

- [1] Jun Liu, Ankur Goswami, Keren Jiang, Faheem Khan, Seokbeom Kim, Ryan McGee, Zhi Li, Zhiyu Hu, Jungchul Lee, and Thomas Thundat. "Direct-current triboelectricity generation by a sliding Schottky nanocontact on MoS₂ multilayers" *Nature Nanotechnology* 13, no. 2 (2018): 112.
- [2] Jun Liu, Mengmeng Miao, Keren Jiang¹, Faheem Khan¹, Ankur Goswami¹, Ryan McGee¹, Zhi Li, Lan Nguyen, Zhiyu Hu, Jungchul Lee, Ken Cadien and Thomas Thundat, "Sustained electron tunneling at unbiased metal-insulator-semiconductor triboelectric contacts", *Nano Energy*, 48 (2018) 320–326
- [3] Jun Liu, Kovur Prashanthi, Zhi Li, Ryan T. McGee, Kaveh Ahadi, and Thomas Thundat. "Strain-induced electrostatic enhancements of BiFeO₃ nanowire loops" *Physical Chemistry Chemical Physics* 18, no. 33 (2016): 22772-22777.
- [4] Jun Liu, Ravi Gaikwad, Aharnish Hande, Siddhartha Das, and Thomas Thundat. "Mapping and quantifying surface charges on clay nanoparticles" *Langmuir* 31, no. 38 (2015): 10469-10476.
- [5] Li, Zhi, Jun Liu, Keren Jiang, and Thomas Thundat. "Carbonized nanocellulose sustainably boosts the performance of activated carbon in ionic liquid supercapacitors." *Nano Energy* 25 (2016): 161-169.
- [6] Chen, Qiang, Jun Liu, Thomas Thundat, Murray R. Gray, and Qi Liu. "Spatially resolved organic coating on clay minerals in bitumen froth revealed by atomic force microscopy adhesion mapping" *Fuel* 191 (2017): 283-289.
- [7] Zhang, Ya-Qian, Hong-Biao Tao, Jun Liu, Yi-Fei Sun, Jian Chen, Bin Hua, Thomas Thundat, and Jing-Li Luo. "A rational design for enhanced oxygen reduction: Strongly coupled silver nanoparticles and engineered perovskite nanofibers" *Nano energy* 38 (2017): 392-400.

Chapter 1 Introduction

1.1 The fundamentals of energy harvesting

In the past decades, energy harvesting materials, devices and systems have become emerging research areas, motivated by the growing demand for energy consumption in all aspects of human activities: from manufacturing and transportation tools, to electronics and nano/microscale devices (*e.g.* implantable biomedical devices, miniaturized sensor networks, microelectromechanical systems (MEMS)).¹⁻⁴ Meanwhile, growing energy consumption is driven by the increasing world population. According to the latest report released by U.S. Energy Information Administration (EIA), the world energy consumption is projected to rise 28% between 2015 and 2040.⁴ It is predicted that substantial contribution for energy consumption would come from developing countries (45-50% increase), as a sacrifice for pursuing economic development (Fig.1-1).⁴ Although fossil fuels (*e.g.* petroleum, coal, and natural gas) still dominate the energy sources of human beings, they are generally considered to be not renewable due to the much faster depletion rate compared to their millions of years' formation.⁴ Besides, our heavy rely on fossil fuels has brought up many serious environmental issues such as air/water pollution and global warming, which are severely threatening the human being's living as well as the ecological system on earth. Therefore, finding renewable energy alternatives is extremely vital for the sustainable development of the human society.

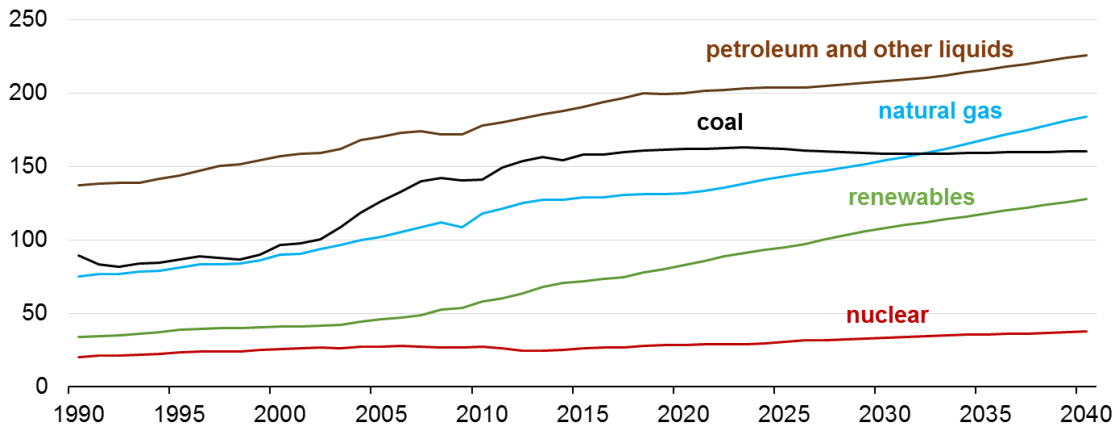


Figure 1-1 Projection of global energy consumption by energy source. Unit for y axis: quadrillion Btu⁴

As a matter of fact, we are living in an ‘ocean’ of energy: a mole of air contains 6.23×10^{26} molecules, which occupies $\sim 24 \text{ dm}^3$ at room temperature and atmospheric pressure. The total thermal energy of them can be calculated by $nk_{\text{B}}T$, where n , k_{B} and T is molecule number, Boltzmann constant and temperature, respectively. Accordingly, 1 m^3 air surrounding us contains $\sim 2560 \text{ J}$ thermal energy, which is sufficient to light a 15 W incandescent bulb for more than 10 minutes! Another example can be found in Earth's oceanic tides. Tidal forces are periodic variations in gravitational attraction exerted by celestial bodies, which contains a huge amount of energy over 75 TW ($1 \text{ terawatt} = 10^{12} \text{ W}$) around the world. Other examples are relatively well known such as solar energy, wind energy, nuclear energy *etc.*

It is therefore apparent that many options are available for renewable energy harvesting from nature, and then what would be the secret ‘recipe’ for an efficient harvesting? Generally, the modern conception of energy harvesting is considered as a process that converts those natural energy resources into electricity, *i.e.* the presence and motion of electric charges. Unfortunately, most of the energy resources around us are randomly distributed. In contrast, a directional

electric charge motion is always associated with certain ‘field’ or ‘gradient’. Namely, one would need a ‘source’ as well as a ‘drain’ of energy in order to induce a directional charge flow: gravitational field makes water flow from higher places to lower ones, which drives electromagnetic generator in a hydropower station and generate an alternative current (AC) electricity⁵; in a photovoltaic device, built-in electrostatic field in a semiconductor p-n junction can separate the photo-excited electron-hole pairs generating a direct current (DC)⁶; The ‘field’ in thermoelectric materials is originated from the temperature gradient in the materials, giving rise to a chemical potential gradient of the electrons/holes⁷; Piezoelectric generator works based on the electrical polarization from positive-negative ion center separation under external mechanical stress⁸. Accordingly, an important indication we can learn from the above examples is that creating a physical ‘gradient’ is the key for harvesting electricity for practical applications. This conception, as will be showing in this thesis, serves as the main methodology for exploring new strategies for triboelectricity harvesting.

Basically, a complete energy harvesting system includes energy capture, transduction, power conditioning, energy storage and electronic load, which covers a broad range of technologies and relies on quite a broad range of fundamental science.⁹ Specifically, the electrical characteristics of initial electric power harvested from environment will affect the design and optimization of the following steps. For example, the open-circuit voltage output from a solar cell (0.5~0.7 V) is determined by the relative Fermi-energy different between the p- and n-type silicon⁶. Parallel and series connection of the single unit would be needed for increasing current and voltage output, respectively. The most of electricity harvested from vibrational energy in environment is AC with varying frequency, which needs to be rectified into DC and conditioned for practical applications.^{1,3} In this thesis, we would be comparing the fundamental differences of the

electricity characteristic between the power generated by conventional triboelectric nanogenerators and the one generated by our new strategy.

1.2 Nano/micro mechanical energy harvesting technologies

Generally, the terminology ‘nano/micro energy’ in literatures often refers to different aspects of the energy harvesting system. Firstly, ‘nano/micro’ refers to dimension of the energy harvesting system that can produce power at microwatts level. They are capable of collecting environmental energy and drive miniaturized electronics such as sensors, actuators and implanted bio-devices. This is largely driven by the growing demand on the proliferation of these devices. Fixed devices where mains connection would be impractical or involve excessive installation costs would also prefer small environmental energy harvesters. Generally, the fabrication of those small energy harvesting units rely on highly parallel fabrication techniques common to the semiconductor and MEMS industries. From a material point of view, a number of new energy harvesting technologies with great performances are enabled by the newly-found novel physical/chemical properties of nanomaterials. Nanotechnologies such as nano/microfabrication, quantum dot synthesis, super lattice deposition, *etc.* have boosted the material performance in various energy harvesting technologies. Last but not the least, modern nanoscale characterization tools such as scanning probe microscopy (SPM) have helped researchers investigate the fundamental science of energy harvesting materials, which in turn benefit the development of new concepts and technologies. ^{1,3}

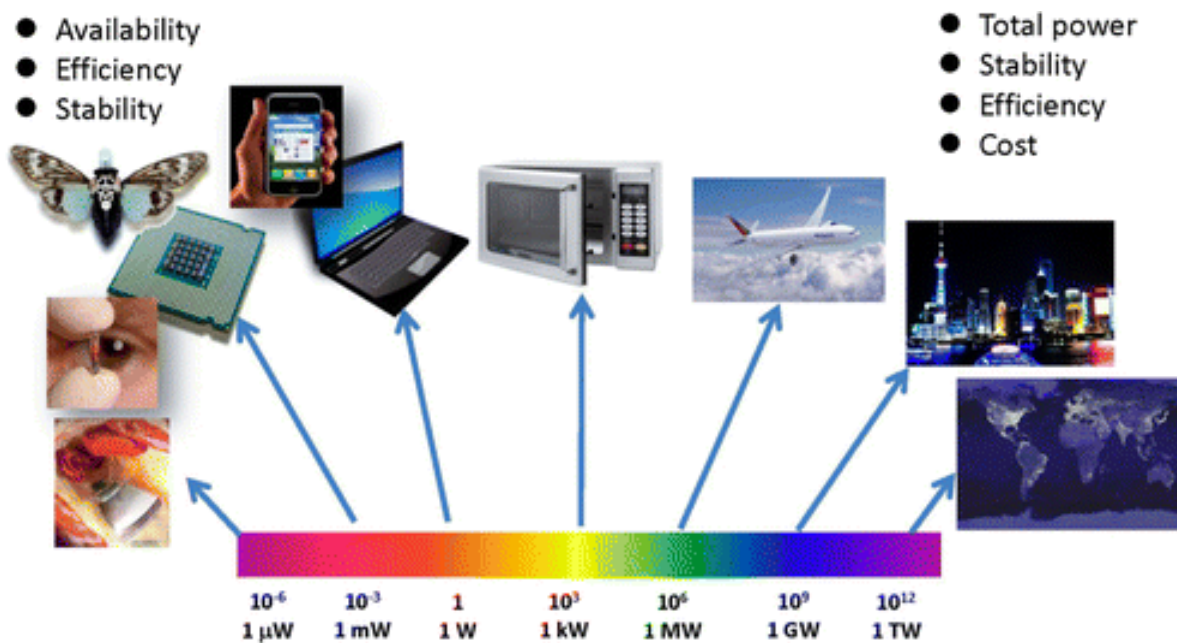


Figure 1-2 Magnitude of power and its corresponding applications.¹⁰ (Reprinted with permission from ACS publications)

As we mentioned in the last chapter, there are many new energy harvesting technologies that have been developed to date, which can be basically classified in terms of their energy sources: photovoltaic technology has been utilized to harvest electricity from solar energy⁶; photocatalysis or photoelectrocatalysis have been developed for converting/ storing solar energy into chemical energy^{11,12}; thermoelectric materials and pyroelectric materials are capable of converting static thermal gradient and varying thermal gradient into electricity, respectively^{7,13}; bioenergy can be harvested from materials derived from biological sources¹⁴, *etc.*

Among those emerging new energy technologies, mechanical energy harvesting is one of the most intensively studied research area ever since the electromagnetic generators was discovered in the years of 1831-1832 by Michael Faraday. It has been utilized in hydropower stations for more than a century. Meanwhile, the same mechanism has been applied in wind turbine, with which wind power can be harvested in various locations. Specifically, the past decade has

witnessed a fast growing of piezoelectric and triboelectric energy harvesting technologies, where nanomaterials and nanotechnologies have play an important role on those fundamental breakthrough. Accordingly, the following part would summarize some of the main progress that has been made in nano/micro mechanical energy harvesting technologies.

1.2.1 Electromagnetic nano/micro energy harvesting

Electromagnetism-based power generation technology has been developed since the early 1930s, which is still one of the main ways of generating electric power nowadays. The basic principle is Faraday's law of electromagnetic induction: a potential difference can be induced between the ends of the conductor when is moved through a magnetic field. Technically, a coil of wire rotates in a magnetic field produces an alternating current. The voltage V , or electromotive force (emf), induced in a circuit is proportional to the time rate of change of the magnetic flux linkage of that circuit¹:

$$V = N \frac{d\phi}{dt}, \quad (1-1)$$

where N and ϕ is the number of coil turn and the average flux linkage per turn, respectively. The instantaneous power P_e extracted by the electromagnetic force $F_{em}(t)$ is given by the product of the force $F_{em}(t)$ and the velocity dx/dt ¹:

$$P_e = F_{em}(t) \frac{dx}{dt}, \quad (1-2)$$

which is dissipated in the coil and load as expressed by¹:

$$P_e = F_{em}(t) \frac{dx}{dt} = \frac{v^2}{R_L + R_C + j\omega L_C}, \quad (1-3)$$

where R_L , R_C and L_C is load resistance, coil resistance and coil inductance, respectively.

In some special applications where miniaturized devices are needed, the size of energy harvesting unit has to be decreased such that vibrational energy can be harvested from environment. To this end, micro-scale coil pattern prepared by photolithography techniques is highly desirable. Such coil patterns can be fabricated on various substrates such as silicon and flexible substrates. For example, Williams *et al.*¹⁵ developed a system containing a spring-mass subsystem attached to a GaAs wafer and a planar integrated coil on a gold coated wafer after a lift-off processing. It is estimated that a 50 μm inertial mass displacement would produce 1 μW at 70 Hz and 100 μW at 330 Hz. Wang *et al.*¹⁶ reported a micro-machined electromagnetic generator combining an integrated coil with an electroplated copper planar spring. The electroplated spring formed on a silicon substrate is prepared by KOH etching. A NeFeB permanent magnet is manually glued to the centre of the spring with a maximum output around 60 mV generated from 14.7 m/s^2 acceleration. In another attempt, microcantilever-based electromagnetic generator has been developed: an array of microcantilevers comprising inertial mass and integrated coil are placed close to a common fixed magnet.¹⁷ Electric power can be harvested from cantilever vibrational movement. The theoretical power output and voltage output of single cantilever is ~ 6 nW and 1.4 mV, respectively, at a resonant frequency of 58 kHz.¹⁷

Provided a generator is properly designed without constrain on size, the electromagnetic-based method is a very efficient approach for the kinetic energy-electricity conversion. Since the electricity power output relies only on relative velocity and change in magnetic flux, an electromagnetic generator will not be limited in amplitude by the fatigue strength of, for instance, piezoelectric materials. And also, they have the broadest frequency bandwidth over which energy can be harvested compared with other methods, due to the high level of electromagnetic damping

achievable. However, the performance of micro-scale electromagnetic generators is largely limited by the possible density of coil turns fabricated with integrated circuit technology. It is also clear from the fundamental principles that the miniaturization of coil pattern reduces power output level considerably ($0.1 \mu\text{W}/\text{ms}^2$ for a 1 cm^3 device vs. $10000 \mu\text{W}/\text{ms}^2$ for a 100 cm^3 device). Therefore, the major challenge for electromagnetic nano/micro energy harvesting technology is to overcome the negative dimension-effect.^{1,3}

1.2.2 Piezoelectric nano/micro energy harvesting

The piezoelectric effect is understood as the linear electromechanical interaction between the mechanical and the electrical state in non-central symmetric structured materials (e.g. ZnO, PZT (lead zirconate titanate), BaTiO₃, etc.).^{8,18,19} For example, a hexagonal unit cell has no center of symmetry. In the absence of an applied force the centers of mass for positive and negative ions coincide with each other (Fig. 3, top-left). When a strain is applied to the materials, piezoelectric polarization charges are induced at the two ends of the crystal along certain orientations: under an applied force along y , the centers of mass for positive and negative ions are shifted which results in a net dipole moment P along y (Fig. 1-3, top-right); when the force is along a different direction, along x , there may not be a resulting net dipole moment in that direction though there may be a net P along a different direction y (Fig. 1-3, bottom).

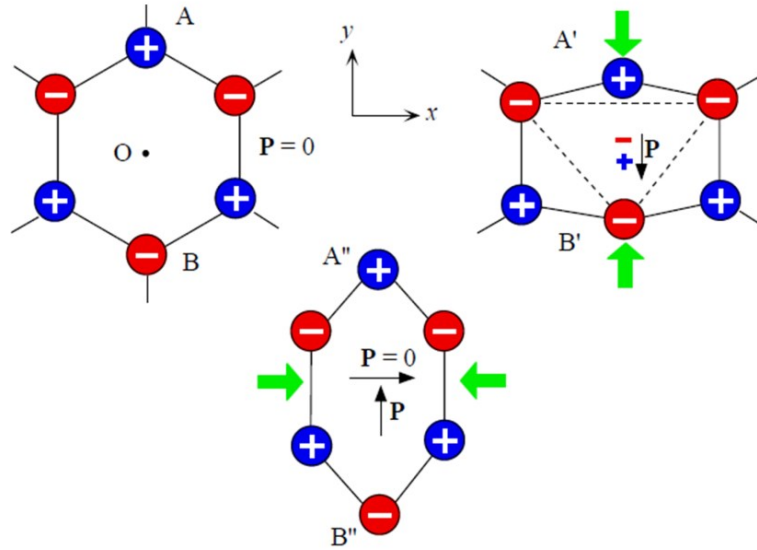


Figure 1-3 A hexagonal unit cell with non-symmetry crystal structure: in the absence of strain (top- left); under an applied strain along y (top-right); under an applied strain along y (bottom).

If T_j is the applied mechanical stress along j direction and P_i is the induced polarization along the i direction, then P_i is determined by:

$$P_i = d_{ij}T_j, \quad (1-4)$$

where d_{ij} is the piezoelectric coefficient. The typical d value for piezoelectric materials is on the order of 10^{-11} - 10^{-12} mV^{-1} . The presence of this stress-induced polarization in all unit cell results in a macroscopic straining-oriented electric potential, which is known as piezopotential. To date, piezoelectric materials have been used in various applications such as spark generators, displacement transducers, accelerometers, and microphones.^{1,3}

Piezoelectric material-based systems are good candidates for vibrational energy harvesting at small-scale. The most typical examples are cantilever systems coated with functional piezoelectric thin film. Piezoelectricity can be generated by the cantilever vibration excited by

environmental vibration, which provides varying strain to the piezoelectric thin film. Roundy, S., *et al.*²⁰ reported a PZT-coated cantilever generator with an 1 cm^3 volume, which can harvest $190 \text{ }\mu\text{W}$ power from acceleration of 2.5 ms^{-2} at 120 Hz . However, the coupling strength decays fast at micro-scale and relatively large load impedances are required for achieving the optimal working condition. Meanwhile, aging issues such as depolarization and brittleness are presented as drawbacks of the piezoelectric materials. For low-frequency applications, such as those related to wearable sensors, polymer-based materials (e.g., dielectric elastomers) are valid alternatives to ceramics due to their flexibility, inexpensiveness, and durability.

An important breakthrough for piezoelectric energy harvesting is the concept of piezoelectric nanogenerators proposed by ZL Wang's group from Georgia Tech in 2006. It was initially revealed by AFM techniques that ZnO nanowires show a strong piezoelectric response under the AFM probe stress.²¹ A power output of $10 \text{ pW}/\mu\text{m}^2$ has been reported. While piezoelectricity is an integrated volume effect, the piezoelectric response found in ZnO nanowires is proved to be a surface polarization-related phenomenon. They have also demonstrated DC piezoelectricity output by a ZnO nanowire array nanogenerator system driven by ultrasonic wave, where a zigzag electrode acts as an array of parallel integrated metal tips that can generate and collect output electricity from the nanowires.²² To scale up the power output, various device configurations such as vertical nanowire integrated nanogenerator (VING)²³, lateral nanowire integrated nanogenerator (LING)²³ and nanocomposite electrical generators (NEG) (vertically grown piezoelectric nanostructure with polymer matrix)^{24,25} have been developed. Although nanogenerators are considered as potential candidates for powering portable electronics and microsensors, the typical piezoelectric voltage output is on the order of $10\text{-}100 \text{ mV}$ with an electrical load R on the order of $100 \text{ M}\Omega$, limited by the physical mechanism and large

impedance of the system. Thus, the current and power output is low, which still needs significant enhancement for practical application. Generally, piezoelectric materials-based harvesters are good choices for high-frequency, low-strain deformations. However, they lack the elasticity needed for harvesting large strains.

1.2.3 Electrochemistry-based nano/micro mechanical energy harvesting

Electrochemistry-based harvesters have emerged as a new strategy for mechanical energy harvesting application. Sangtae Kim *et al.*²⁶ reported a device consisting of two identical Li-alloyed Si as electrodes, separated by electrolyte-soaked polymer membranes. It works based on stress–voltage coupling in electrochemically alloyed electrodes. It was demonstrated that lithium ion (Li^+) migration can be driven by the chemical potential difference induced by the bending-induced asymmetric stresses. The lithium ion migration results in electricity output from the device. A V_{oc} of 23 mV, I_{sc} of 14.5 μA , and power density of 0.48 $\mu\text{W}/\text{cm}^2$ at 0.3 Hz has been reported.

Another interesting design based on electrochemical system is modulating the capacitance of electrode by external strain. Shi Hyeong Kim, *et al.*²⁷ reported a carbon nanotube yarn twist harvester, of which the 3D spiral structure can response to the external tensile or torsional strain and thus results in a capacitance modulation. Due to the existence of a chemical potential between the harvester electrode (carbon nanotube yarn twist) and the surrounding electrolyte, an equilibrium charge on the electrode can be generated by immersing the electrode into an electrolyte, which can be used for energy harvesting. By testing the harvester in a simulated

ocean environment (0.6 M NaCl), they have reported a peak power output of ~ 94 W/kg under a 30 % stretch and deformation frequency above 6 Hz.

Using ionic polymer composite is another derivative is for mechanical energy harvesting. Ying Hou, *et al.*²⁸ reported an ionic polymer-based p–n junction structure for low frequency vibrational energy harvesting. It features with very slow decaying of the induced potential as a function of time, thus making it as an efficient way of harvesting mechanical energy at very low frequency. It works based on non-equilibrium space charge transfer at the p-n junction interface under compressive stress. The p–n junction structure can rectify the ion flow and thereby allows a net direct current output. Upon a low-frequency mechanical compression (0.1 Hz), an open circuit voltage of ~ 122 mV, a current density of ~ 1 $\mu\text{A}/\text{cm}^2$, and a corresponding volumetric power density ~ 2 $\mu\text{W}/\text{cm}^3$ have been reported. Similarly, Hao shao, et al. demonstrated the d.c. power out using a metal-conducting polymer (PPy) Schottky diode structure, reporting a current density as high as 62.4 $\mu\text{A}/\text{cm}^2$ and voltage of 0.7 V. It is concluded that one of the two metal electrodes should form a Schottky contact with the polymer, while the one needs to have an Ohmic contact with it.²⁹

1.2.4 Triboelectric nano/micro energy harvesting

The recent years have witnessed a fast growing technique called triboelectric nanogenerator (TENG), which is able to convert frictional energy into electricity. As a pioneer of the technology, ZL Wang's group from Georgia Tech developed the concept by observing an 'unexpected' electricity output signal during a piezoelectricity experiment in 2012. Basically, TENGs work based on contact electrification, coupled with electrostatic induction and capacitance modulation.

Contact electrification, which will be discussed with more details in Section 1.3.2, is a well-known phenomenon that two materials can be electrically charged when rubbing against each other.^{10,30}

Given that an insulating material is involved in contact electrification, electrostatic charges would be built up on the surface. If there is a metal electrode present on the back side of this insulator, image charges would be developed (i.e. charge induction). The triboelectric potential results from the separation of the two materials with an opposite sign of electrostatic charges. By modulating the capacitor system, a dielectric displacement a.c. current can be generated¹⁰:

$$i = \frac{dQ}{dt} = \frac{CdV}{dt} + \frac{VdC}{dt}, \quad (1-5)$$

As per the working mechanism of TENGs, there are four basic operation modes being developed: vertical contact-separation mode, in-plane sliding mode, single-electrode mode, and freestanding triboelectric layer mode.³¹ In vertical separation mode, the two charged materials coated with top and bottom electrodes are charged with opposite charges upon contact. They are vibrated vertically by external force such that a varying electric potential is generated. At the same time, the capacitance of the systems also oscillates due to the changing capacitor distance. As a result, electrons flow back and forth in the circuit in response to the varying potential, generating a.c. electricity. Gunag Zhu, *et al.*³² reported a vertical mode TENG consisting a polymer layer and a gold nanoparticle-decorated metal layer, which is capable of generating an open-circuit voltage of ~200 V, a short-circuit current of ~2 mA, and a corresponding area power density of ~313 W/m². It is found that the gold nanoparticle decoration can dramatically enhance the performance, which they believe is mainly due to a higher effective contact area between the two materials. They also developed a folded flexible TENG structure with multi-layered generator units, which can be used as an insole and harvest mechanical pressure during walking.

The TENGs based on lateral sliding mode shares the same device configuration as the ones based on vertical mode. Instead of being vertically vibrated, the two dielectric materials slide with respect to each other under an external force. The image charges on the top and bottom electrodes flow back and forth in order to balance the varying potential difference. In this case, the capacitance oscillates as a result of changing area of the capacitor systems.^{33,34} It is noted that the sliding mode is not only limited to the linear motion between the contact materials, but also refers to cylindrical rotation or disc rotation friction mode. Peng Bai, *et al.*³⁵ demonstrated a cylindrical rotating TENG based on a core-shell structure. Polymer nanoparticles are made on surface in order to strengthen the charge transfer. A power density of 36.9 W/m² (short-circuit current of 90 μ A and open-circuit voltage of 410 V) has been reported at a linear rotational velocity of 1.33 m/s (a rotation rate of 1000 r/min). Ling Long *et al.*³⁶ developed a segmentally structured disk TENG and did a thorough investigation on the relationship between the rotation speed and the electrical output. A significant improvement of the rotation disc-based TENG is achieved by using radial arrays of micro-sized sectors on the contact surfaces, enabling a high output power of 1.5 W (area power density of 19 mW/cm²) at an efficiency of 24%.³⁷ It is reported that various ambient motions, including light wind, tap water flow and normal body movement can be harvested by this type of generator.

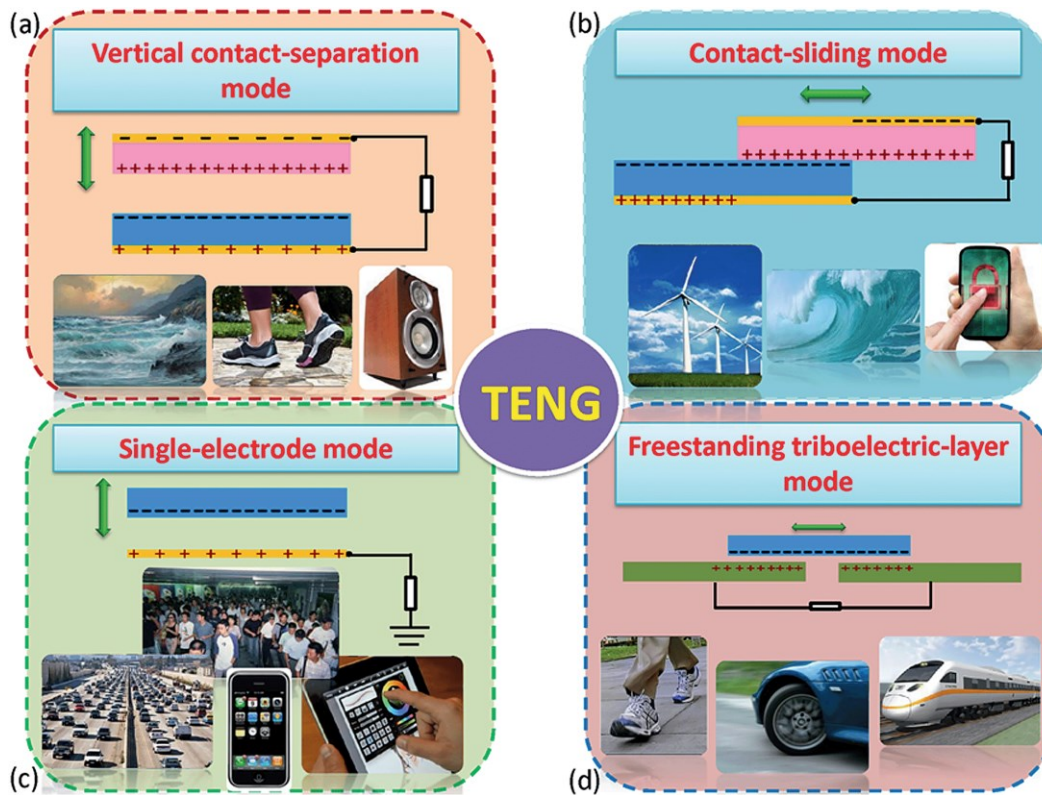


Figure 1-4 The four fundamental modes of triboelectric nanogenerators: (a) vertical contactseparation mode; (b) in-plane contact-sliding mode; (c) single-electrode mode; and (d) freestanding triboelectric-layer mode.³¹ (Reprinted with permission from RCS publications)

In some cases, the devices cannot be directly connected to the load, such as a human walking on a floor. In order to address this problem, single-electrode mode has been developed for TENGs. Basically, the bottom material is grounded such that the potential change of the electrode can be maintained. Ya Yang, *et al.*³⁸ reported a TENG based on single-electrode mode that can produce an open-circuit voltage up to 1100 V, a short-circuit current density of 6 mA/m², and a maximum power density of 350 mW/m² on a load of 100 MΩ. It is utilized for making a self-powered displacement vector sensor system. The single-electrode mode can also be used in the cases of vertical motion under the same mechanism.

Freestanding triboelectric-layer mode is another derivative of TENG, where a dielectric layer moves on a pair of bottom electrodes as shown in Fig. 1-4. When the moving dielectric layer approach and depart from the electrodes, electrons in the circuit connecting the two bottom electrodes oscillate back and forth in order to balance the varying triboelectric potential. Thus an a.c. power is generated. Sihong Wang *et al.*³⁹ reported such a freestanding triboelectric-layer TENG using a fluorinated ethylene propylene (FEP) as the freestanding triboelectric layer, and two acrylic-supported Al as bottom electrodes. An open-circuit voltage of 14 KV, a short-circuit current density of 3.2 mA/m², and a maximum power output density of 6.7 W/m² on a load of 1 GΩ.

Recently, a new idea of applying TENG for ocean energy harvesting has been proposed.⁴⁰⁻⁴² The ocean energy is considered as an important renewable and clean energy source, featured with low oscillation frequency (<2 Hz) and varying amplitude. At low frequency regime (<5 Hz), experimental results show that the power output with TENG surpasses that with traditional electromagnetic generator (EMG).⁴¹ Besides, TENG has much light weight density compared with EMG. Fig.1-5 illustrates the working principle of a typical TENG for ocean energy harvesting is similar to the freestanding triboelectric-layer mode as introduced above.⁴¹ Instead of using planar structure, hollow spherical structure with two fixed dielectric layers being fixed on the wall and a mobile dielectric ball are included.⁴³ The enclosed hollow structure provides a good isolation between water and electronic parts. Driven by water motion, the dielectric ball inside can move around freely a full degree of freedom, resulting in varying triboelectric potential and thus power output in the system as explained in the freestanding triboelectric –layer mode. In addition to the rolling spherical structure (10 mW for single unit), various other device configurations has been developed so far for water motion energy harvesting, such as wavy-

electrode structure (0.64 MW/km^2)⁴⁴, duck-shaped structure (1.4 W/m^2)⁴⁵ and air-driven membrane structure (13.2 W/m^2)⁴⁶. It is suggested that a hybrid energy harvesting system consisting of wind turbine, solar panels and TENG networks (1.15 MW/km^2) may be used in the future.⁴¹

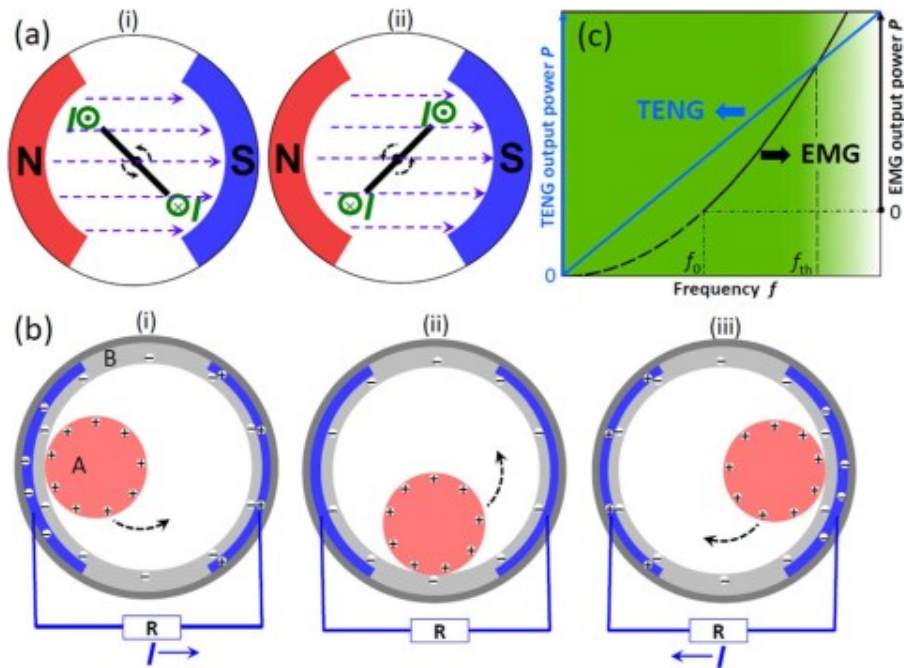


Figure 1-5 Classical electromagnetic generator (EMG) vs triboelectric nanogenerator (TENG). Working mechanism of (a) EMG based on electromagnetic induction (b) TENG by coupling of triboelectrification effect and electrostatic induction. (c) Output power of EMG and TENG vs. operation frequency f .⁴¹ (Reprinted with permission from Elsevier Publishing Group)

To harvest energy from difference environmental sources, various hybrid systems have been developed. Yunlong Zi, *et al.*⁴⁷ reported a triboelectric–pyroelectric–piezoelectric hybrid cell composed of a sliding mode TENG and a pyroelectric–piezoelectric nanogenerator (PPENG). Besides the triboelectricity output, thermal energy (friction-induced heat) and piezoelectricity

can be harvested by a piece of 110 μm -thick polarized polyvinylidene fluoride (PVDF) deposited with Cu electrodes. The hybrid cell has been demonstrated to extend the illumination time of a LED and charge a supercapacitor at a charging rate about twice of that charged by the TENG along. A hybrid solar cell and TENG has been demonstrated by Yang *et al.*⁴⁸, where a flexible transparent polydimethylsiloxane (PDMS) nanowire-based TENG serves as the mechanical energy harvesting unit as well as a protection layer for Si solar cell. Yang *et al.*⁴⁹ also reported a hybrid thermoelectric-TENG system consisting of a polyamide (PA)-perfluoroalkoxy (PFA) polymer film-based TENG, a Bi_2Te_3 -based thermoelectric cell, and a silicon (Si)-based solar cell. They also developed an integration system of an electrochemical cell for converting chemical energy into electricity and a top PDMS-based TENG layer for mechanical energy harvesting.⁴⁹ It is found that embedding of BaTiO_3 nanoparticles into PDMS matrix can dramatically enhance the performance by increasing the relative permittivity of the composite and thus enhancing the TENG voltage output. Such hybrid system has been used for driving biosensors and lighting up to 30 green LED.

Since the first prototype being reported in 2012, the power output of TENG has been improved significantly reaching $\sim 500 \text{ W/m}^2$. A wide range of applications for energy harvesting have been proposed, from small scale self-powered systems and processes, to large-scale ocean energy scavenging. For the self-powered systems, it has been successfully demonstrated in powering motion sensors such as displacement sensors³⁸, pressure sensors⁵⁰, acceleration sensors⁵¹, vibration sensors⁵², *etc.* A self-powered smart keyboard system is a very interesting design based on TENG.⁵³ The application has also been extended for chemical detection⁵⁴, transistor⁵⁵, and mass spectrum technologies⁵⁶. Compared to other mechanical energy harvesting methods, TENG has many unique advantages such its high power output, low weight, low cost

and simple fabrication. However, some drawbacks also exist such as its pulsed output, high impedance, and low durability. Beside the extensive study based on conventional polymer-based TENGs, a new concept of TENG based on tunneling transport in metal-semiconductor contact has recently been demonstrated. Instead of producing dielectric displacement a.c. current, we found that a continuous d.c. current with high current density can be generated based on different working principle.⁵⁷

1.3 Charge transfer in frictional contact system

Friction-related phenomenon is one of the earliest fundamental physics that human has paid attention to. Even in the very early stage of human civilization, our ancestors have already mastered the skills of making fire from drilling in wood, which is perhaps the earliest energy harvesting technique we have ever developed. On another hand, the triboelectric phenomenon that friction can result in electrostatic charges on contact materials has also been observed about hundreds years ago. As a matter of fact, these observations imply two fundamental physical processes occurring in friction: energy transfer and electronic charge transfer. Although it has been discovered and investigated for a long history, the fundamental aspects of energy dissipation process in friction are not fully understood, mainly due to the multiple and complicated physical processes being involved. Since friction plays an important role in various human activities, from mechanical manufacturing and geology, to bio-engineering and nanogenerators, it has been an intensively studied area attracting tremendous research interest from multi-disciplines such as physics, chemistry, mechanical engineering, *etc.*^{58,59}

The earliest scientific understanding of friction was summarized in the 18th century by Amontons' law: the force of friction is directly proportional to the applied load (the ratio is

known as friction coefficient), and is independent of the apparent area of contact or the sliding velocity. However, it is not necessarily true for single asperity contacts at nanoscale, which is revealed by modern characterization tools such as atomic force microscopy (AFM).⁵⁹ At atomic level, friction is the interaction between electron clouds of contact atoms from two materials. It has been proposed that the interaction between periodic potential of lattice structures of the two contact materials results in the so-called ‘stick-slip’ friction mode.^{59,60} However, if the elasticity of the material is stiff and the potential corrugation is sufficiently enough, the displaced interfaces may reach mechanical equilibrium at all points and slide without stick–slip (e.g. smooth frictionless sliding).⁵⁹

For triboelectric energy harvesting application, the main challenge is to understand the fundamental process of charge excitation, transfer and conduction in the frictional contact system, which, unfortunately, is extremely challenging because of the complicated dynamic electronic environment at the sliding interface. In this section, we are going to discuss some of our understanding regarding the elementary process in friction from different angles.

1.3.1 Theories of contact electrification

Many people have the experience of being electrically shocked by charges in dry winter time. The phenomenon that two materials get electrically charged by being touched or rubbed is known as ‘contact electrification’. Specifically, it is also referred to ‘triboelectrification’ when the two materials are rubbed against each other. Contact electrification has been mostly considered as a hazard in industry, such as explosion caused by sparks and destroying MOS transistor by electrostatic charges carried by person. On another hand, contact electrification is

useful in various situations, including spray-painting, particle separation, electrostatic printing, and mechanical energy harvesting techniques. The latter, especially, is the one we are interested in for energy harvesting purpose. The triboelectric charges generated from impact, sliding or rotation serves as the resources for triboelectricity output.

Although triboelectric phenomenon has been observed and studied for hundreds of years, the origin of triboelectrification is still controversial, even with opposite charging behavior being reported for the same type of materials systems.⁵⁸ In recent years, there is a growing research interest in controlling/manipulating the triboelectric phenomenon, driven by the fast development of triboelectric nanogenerator (TENG) technique for energy harvesting.^{10,57} With modern research tools such as electrostatic force microscopy (EFM), Kelvin probe force microscopy (KPFM), conductive-AFM (C-AFM), people's understanding towards fundamental aspects of triboelectric process has been enhanced. Nevertheless, it is still a debating research topic that fascinates many scientists nowadays.

As per the materials system involved in contact electrification, it can be classified as metal-metal contact, metal-insulator contact, insulator-insulator contact, and metal-semiconductor contact. Specifically, conventional TENGs have been utilizing insulator-insulator contact or metal-insulator contact for dielectric displacement current generation. Recently, tunneling current-based direct current generator has been developed by our research group, providing another approach for harvesting triboelectricity. To further improve the performance of any kind of mechanical energy harvesting techniques, it is vital to understand the fundamental process in contact electrification.

1.3.1.1 Metal-metal contact system

Although plenty of debates still exist, the theory of contact electrification of metal-metal frictional contact is relatively mature, which is supported by many solid experimental evidences. It is based on the premise that charge transfer is a result of surface potential (or fermi-level E_F in the case of metal-metal contact) alignment in order to reach a thermodynamic equilibrium at the contact interface.⁵⁸

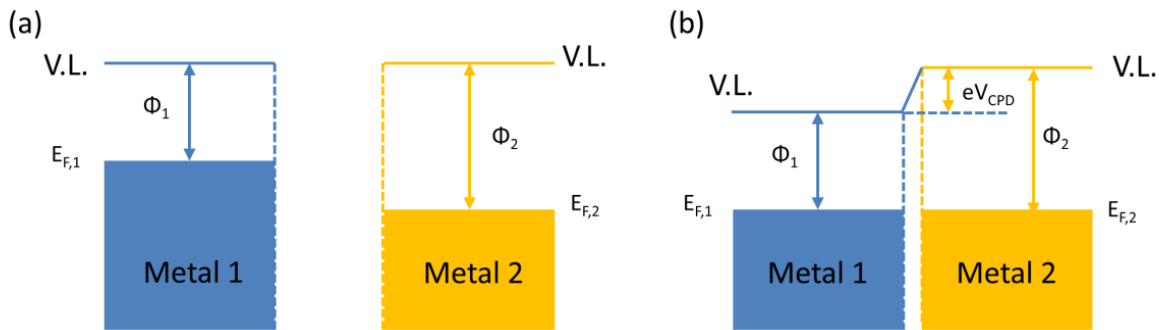


Figure 1-6 Energy band diagram of metal-metal system (a) before and (b) after contact.

As is shown in Fig. 1-6, metal 1 and metal 2 has work function (e.g. the minimum energy for an electron in the metal to escape into the vacuum level) of φ_1 and φ_2 , respectively. At ordinary temperature ($kT \ll E_F$), it is considered that the energy states below E_F are fully occupied by electrons, while those above E_F are empty. It is worth mentioning here that this premise becomes tricky in the case of metal-insulator contact as will be discussed later, since the concept of E_F is not valid in describing electronic structure of insulators. Before contact, there is a contact potential difference V_{CPD} between the two metals, which is determined by the work function difference:

$$V_{\text{CPD}} = (\varphi_1 - \varphi_2)/e, \quad (1-6)$$

When the two metals are brought into intimate contact as shown in Fig. 1-6, the V_{CPD} would drive the electrons to flow from metal 1 to metal 2 until the fermi-energy level of them becomes identical. The amount of charge transferred in this process is given by the product of V_{CPD} and the effective capacitance between them. When they are separated after contact, back tunneling of electrons occurs in order to maintain thermodynamic equilibrium (i.e., to maintain the V_{CPD}). During the separation process, the capacitance C would slowly decrease while the resistance R rises rapidly as quantum mechanical tunneling of electrons decays exponentially as a function of distance (Fig. 1-7). As a result, the time constant RC for the redistribution of charges between the two metals varies approximately as R . To simplify the analysis, it is assumed that the charge tunneling ceases after the separation distance reaches a critical value z_0 . It is suggested by Harper that $z_0 \sim 1 \text{ nm}$.⁶¹

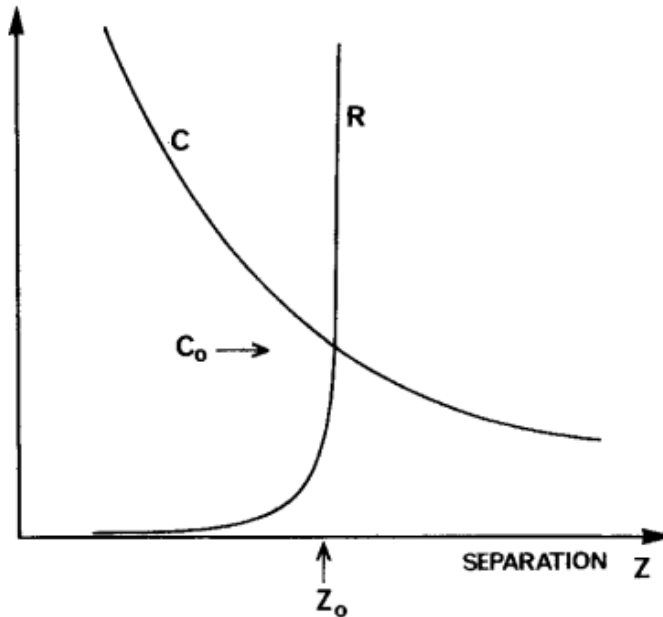


Figure 1-7 Schematic indication of the variation of capacitance (C) and resistance (R) between two metal surfaces as a function of their separation z . z_0 represents the critical

value above which charge tunneling ceases. C_0 is its corresponding capacitance at z_0 .⁵⁸

(Reprinted with permission from Taylor & Francis Group)

According to this assumption, the charge on metals after separation is approximated to be:

$$Q = C_0 V_{\text{CPD}}, \quad (1-7)$$

where C_0 is its corresponding capacitance at z_0 . Figure 1-8 summarizes the experimental data of charge on a Chromium (Cr) sphere after contact with a sphere of another metal with varying work potential.⁶¹ It is plotted against V_{CPD} between the metal and Cr. It can be seen that Q shows a proportional tendency with respect to V_{CPD} , the slope however, deviates from the theoretical value (C_0) predicted from Eq. 1-7. This is due to the fact that the material surface has an average roughness on the range of 100 nm, which is much higher than the theoretical z_0 (~1 nm). Therefore, the effective C_0 is determined by the surface roughness of the contact materials in real cases.

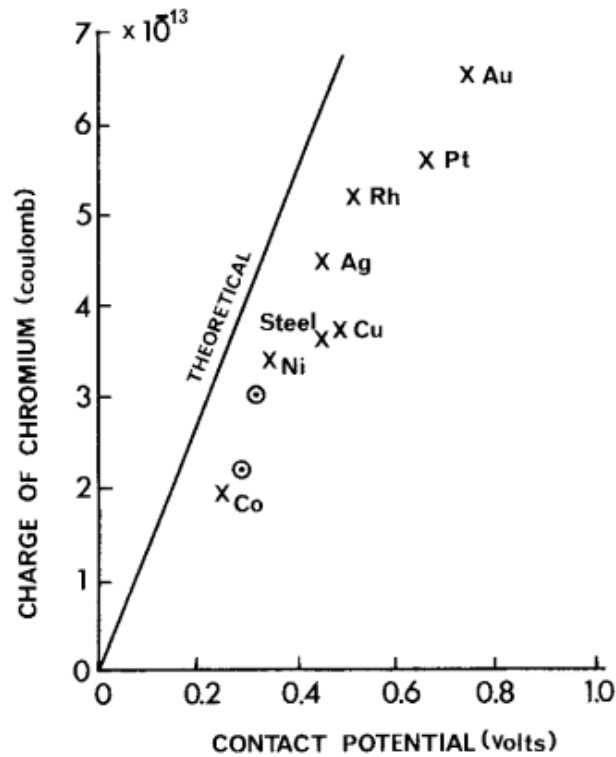


Figure 1-8 Charge on a Cr sphere after contact with a sphere of another metal, plotted against the contact potential difference (V_{CPD}) between the metal and Cr. The line marked 'theoretical' is the prediction of a theory based on tunnelling between closely separated smooth metals.⁵⁸ (Reprinted with permission from Taylor & Francis Group)

1.3.1.2 Metal-insulator contact system

Compared to the metal-metal contact systems, metal-insulator contact systems are much more complicated because multiple processes may be involved. Except for evidences that work function of metal and its correlation with the chemical properties of the insulator have a significant influence on the charge transfer process, other mechanisms such as ion transfer, and

materials transfer carrying charges have also been proposed. Here, we would first start our discussion from an electron transfer point of view.

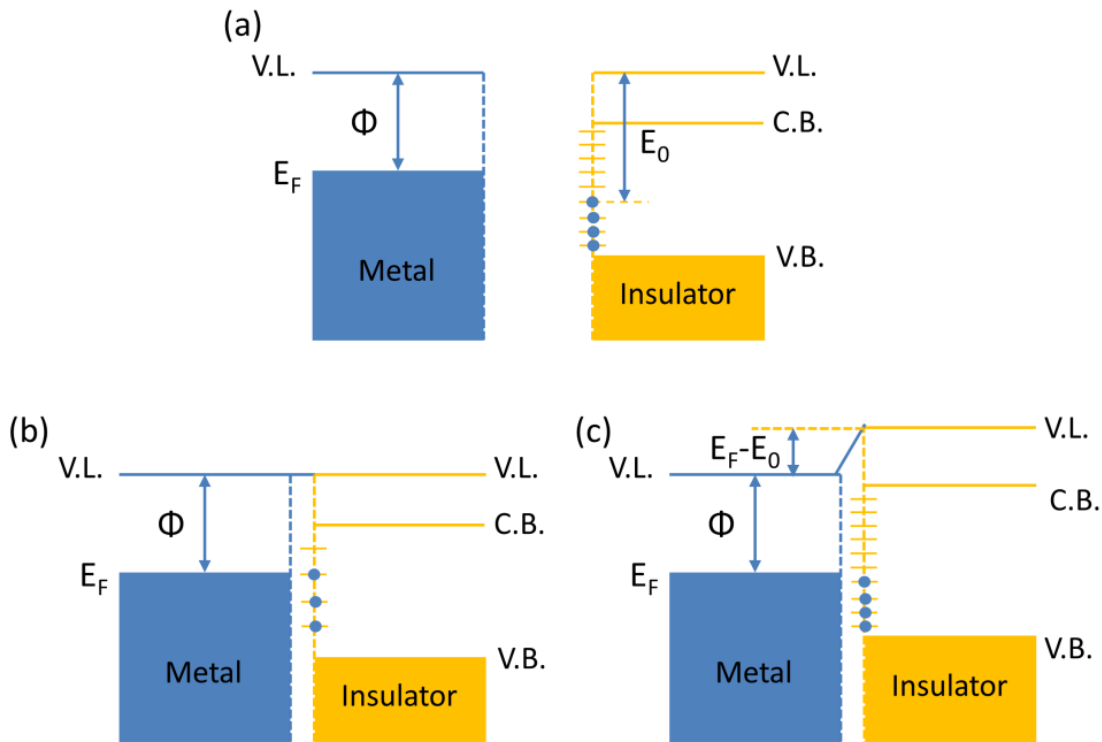


Figure 1-9 Surface states and contact electrification. (a) The insulator is uncharged and the surface states are filled at energies below the neutral level E , and empty above. (b) When the insulator is brought into contact with metal, surface states below the Fermi level will fill, but those above remain empty. If the density of surface states is low (b), the number of electrons which transfer to the insulator is equal to the number of surface states with energy between E and E_F . The electric field between the metal and the insulator is too small to shift the insulator energy levels appreciably. In the opposite limit of high surface state density (c) the surface states need only be filled to a level very slightly above E to create a very strong electric field. This field raises the energy of all the insulator states;

charge transfer ceases, in the first approximation, when the neutral level E_0 is raised to the Fermi level of the metal.

Suppose we have a metal with work function of φ and an insulator with surface neutral level E_0 (the surface state energy level below which are occupied with electrons, above which are empty), and $\varphi < E_0$. (Fig. 1-9a) Upon contact, electron transfer happens from the metal to the insulator under a thermodynamic non-equilibrium condition. Unlike the electrons transfer from continuous energy level to another, electrons are trapped on the surface states existing at the insulator surface, resulting in an electric field E between the metal and the insulator:

$$E = \sigma/\epsilon_0, \quad (1-8)$$

where σ is the surface charge density, and ϵ_0 is the vacuum permittivity. If the metal and the insulator are separated by a small distance z (of the order of atomic dimension), the energy levels in the insulator will be shifted by an amount of $ez\sigma/\epsilon_0$. When the surface state density is low, this energy shift can be neglected, and all the surface states above E_0 but below the metal E_F will be filled up electrons (Fig.1-9b). The number of electrons transferred from metal to insulator can be expressed by⁵⁸:

$$N = \int_{E_0}^{E_F} n(E) dE, \quad (1-9)$$

where $n(E)$ is the density of surface states. It can also be used to describe the case when $\varphi > E_0$ by simply changing the position of E_F and E_0 in the integral symbol. On the contrary, if the surface state density is high, then the shift of energy level on the insulator cannot be neglected. (Fig. 1-9c) This situation can be imagined as the unfilled energy levels on the insulator side are raised immediately after the very first electrons enter into the insulator, such that the charge transfer will cease when the highest filled level reaches the metal E_F level. In this case, the surface charge density can be expressed by²:

$$\sigma = \varepsilon_0(E_F - E_0)/ze, \quad (1-10)$$

which holds no matter what $n(E)$ is, as long as it is high enough.

A more sophisticated description of metal-insulator contact electrification has been developed by J. Lowell⁶² from a quantum mechanical point of view. As is shown in Fig.1-10a, a trap state at insulator surface is represented by a square potential well with a width of $2a$ and a depth of V . The distance between the trap state and metal surface is z . Figure 1-10b shows the wave function distribution of the metal-insulator trap state contact. The transition between the metal electronic states and the insulator surface states are concerned. Suppose $\phi > E_0$, and the initial wave function of electrons in insulator trap state is $\psi(0)$. At the instant of contact, the wave function of the electrons in insulator trap will propagate into the empty sates in metal as a function of time⁶²:

$$\Psi(t) = \int_{-\infty}^{+\infty} a(E)u(E) \exp\left(-\frac{iEt}{\hbar}\right) N(E)dE, \quad (1-11)$$

$$\text{where } a(E) = \int_{-\infty}^{+\infty} \Psi(t)u^*(E) dx \quad (1-12)$$

where $u(E)$ are eigenfunctions of the potential as shown in Fig. 1-10b, $N(E)$ is the number of these eigenfunctions in the energy range from E to $(E+dE)$.

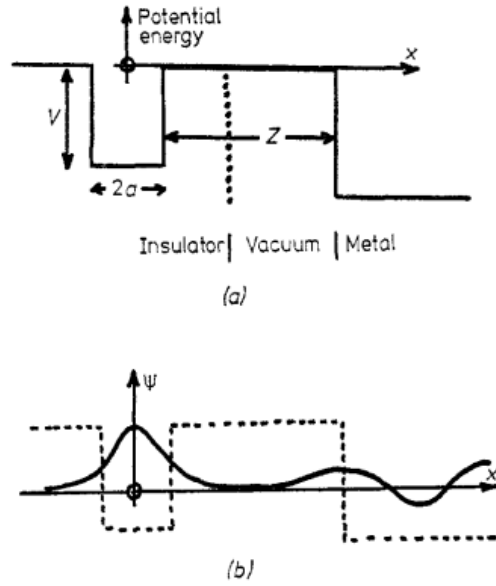


Figure 1-10 (a) Potential energy of an electron as a function of the distance x from the centre of a trap in the insulator, represented by a square well of depth V and width $2a$. The potential is assumed to be continuous across the vacuum/insulator interface (dotted line) for the reasons given in the text. (b) Form of the eigenfunctions (near resonance) of the potential shown in (a).⁶² (Reprinted with permission from IOP science)

It is summarized that⁶²:

$$\Psi(t) = \Psi(0) \exp[-t\tau^{-1} \exp(-2\mu_0 z)], \quad (1-13)$$

$$\text{where } \tau = \hbar(1 + k_0 a)/E_0, \quad (1-14)$$

where E_0 is the initial energy of the electron in the insulator trap, and $k_0^2 = 2mE_0/\hbar^2$. Therefore, the probability of finding the electron in the trap decreases exponentially with time constant τ . Suppose the traps states are initially full and subsequently empty into the metal, the probability of finding an electrons at a distance z from the metal surface is proportional to $|\Psi(t)|^2$ (or, the number of electrons N per unit area of surface is proportional to $|\Psi(t)|^2$). The total charge density per unit area of the insulator at time t can be expressed by⁶²:

$$\sigma = \int_0^\infty ne[1 - |\Psi(t)|^2] dz, \quad (1-15)$$

where n is the number of traps per unit volume in insulator assuming the traps are uniformly distributed in space. Combining Eq. 1-15 and Eq. 1-13, and introducing $\theta = 2t/\tau \exp(-2\mu_0 z)$ gives⁶²:

$$\sigma = \frac{ne}{2\mu_0} \int_0^{2t/\tau} \frac{1 - \exp(-\theta)}{\theta} d\theta, \quad (1-16)$$

Since E_0 is Eq. 1-14 is of the order of an electron volt, τ is estimated of the order of 10^{-15} s, which is much smaller than the t we shall be interested in. Therefore, for $t \gg \tau$, Eq.1-16 can be approximated to be⁶²:

$$\sigma = \left(\frac{ne}{2\mu_0} \right) \ln \left(\frac{t}{\tau'} \right), \quad (1-17)$$

$$\text{where } \tau' = 0.28 (1 + k_0 a) \hbar / E_0, \quad (1-18)$$

The numerical estimation of the term $(1/2\mu_0)\ln(t/\tau')$ is ~ 2 nm, which is equivalent to the tunneling depth of electrons between the insulator and the metal. It is worth mentioned here that thermodynamic equilibrium is not necessarily reached in a single contact. This is supported by the experimental results that repeated contact increase the accumulated surface charge. It is predicted that the charge transfer is fast in the very beginning upon contact, and will get slower and saturated with time. It should also be pointed out that the surface states distribution at the insulator surface may not be uniform^{58,62}.

When an inorganic material such as polymer is involved, the ionic contribution may not be neglected. Lieng-Huang Lee⁶³ proposed a dual mechanism for metal-polymer contact electrification as a non-equilibrium two-step process consisting of instantaneous bond-forming and bond-breaking. According to this theory, the interaction energy ΔE_{INT} between the two molecules can be expressed as⁶³:

$$\Delta E_{\text{INT}} \approx -\frac{Q_N Q_E}{\epsilon R} + \frac{2(C_N C_E \beta)^2}{E_{\text{HOMO}} - E_{\text{LUMO}}}, \quad (1-19)$$

where ΔE_{INT} is the difference in energy of the molecules before and after the interaction; Q_N , Q_E are the total charges for the nucleophile N and electrophile E, respectively; C_N and C_E are the coefficients of the atomic orbital N and E, respectively; β is the resonance integral; ϵ is the permittivity or dielectric constant of the medium, and R is the distance between N and E. The first term in Eq. 1-19 represents the Coulombic or electrostatic contribution, which is long-range and ionic. The second term is the frontier orbital or charge transfer contribution, which is short range and electronic. It is proposed that a bidirectional charging may coexist, and a back-transfer process can take place simultaneously in an entirely different manner than back-tunneling, when the distance among molecular interaction is less than 4 angstrom. (Fig. 1-11)

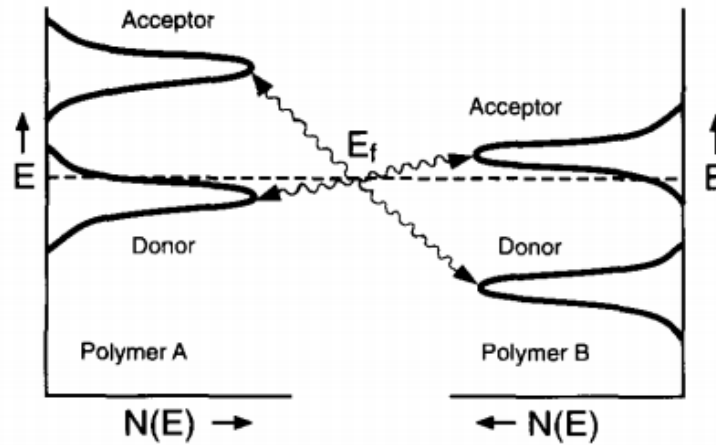


Figure 1-11 Two-way charge transfer between HOMO (donor) and LUMO (acceptor)⁶³

(Reprinted with permission from Elsevier Publishing Group)

1.3.1.3 Insulator-insulator contact system

For the insulator-insulator frictional contact system, it is proposed that the working principle is similar to that of the metal-insulator system: the contact brings the Fermi levels of the metal and

the insulator into coincidence. The sign of the triboelectric charges persisting at the insulator surface is correlated with the contact potential difference.⁵⁸ Although the fundamental understanding of the phenomenon remains elusive, a vast amount of experimental results allow us to summarize triboelectric series (Table 1-1), showing the inclination of triboelectric charge polarity in different materials.¹⁰

Table 1-1 Triboelectric series¹⁰ (Reprinted with permission from ACS publications)

 <p>Positive</p>	Polyformaldehyde 1.3-1.4	(continued)	 <p>Negative</p>
	Etylcellulose	Polyester (Dacron)	
	Polyamide 11	Polyisobutylene	
	Polyamide 6-6	Polyuretane flexible sponge	
	Melanime formol	Polyethylene Terephthalate	
	Wool, knitted	Polyvinyl butyral	
	Silk, woven	Polychlorobutadiene	
	Aluminum	Natural rubber	
	paper	Polyacrilonitrile	
	Cotton, woven	Acrylonitrile-vinyl chloride	
	Steel	Polybisphenol carbonate	
	Wood	Polychloroether	
	Hard rubber	Polyvinylidene chloride (Saran)	
	Nickel, copper	Polystyrene	
	Sulfur	Polyethylene	
	Brass, silver	Polypropylene	
	Acetate, Rayon	Polyimide (Kapton)	
	Polymethyl methacrylate (Lucite)	Polyvinyl Chloride (PVC)	
	Polyvinyl alcohol	Polydimethylsiloxane (PDMS)	
	(continued)	Polytetrafluoroethylene (Teflon)	
 <p>Positive</p>	Aniline-formol resin	Polyvinyl alcohol	 <p>Negative</p>
	Polyformaldehyde 1.3-1.4	Polyester (Dacron) (PET)	
	Etylcellulose	Polyisobutylene	
	Polyamide 11	Polyuretane flexible sponge	
	Polyamide 6-6	Polyethylene terephthalate	
	Melanime formol	Polyvinyl butyral	
	Wool, knitted	Formo-phenolique, hardened	
	Silk, woven	Polychlorobutadiene	
	Polyethylene glycol succinate	Butadiene-acrylonitrile copolymer	
	Cellulose	Nature rubber	
	Cellulose acetate	Polyacrilonitrile	
	Polyethylene glycol adipate	Acrylonitrile-vinyl chloride	
	Polydiallyl phthalate	Polybisphenol carbonate	
	Cellulose (regenerated) sponge	Polychloroether	
	Cotton, woven	Polyvinylidene chloride (Saran)	
	Polyurethane elastomer	Poly(2,6-dimethyl polyphenyleneoxide)	
	Styrene-acrylonitrile copolymer	Polystyrene	
	Styrene-butadiene copolymer	Polyethylene	
	Wood	Polypropylene	
	Hard rubber	Polydiphenyl propane carbonate	
Acetate, Rayon	Polyimide (Kapton)		
Polymethyl methacrylate (Lucite)	Polyethylene terephthalate		
Polyvinyl alcohol	Polyvinyl Chloride (PVC)		
(continued)	Polytrifluorochloroethylene		
	Polytetrafluoroethylene (Teflon)		

1.3.1.4 Identical material contact system

Interestingly, it is evident that even the identical insulating materials brought into contact may result in net charge transfer. This is apparently not plausible to be explained by the Fermi-level alignment-based theory. It is supposed that a degree of asymmetry is often present when two objects are rubbed together.⁵⁸ Mario M. Apodaca *et al.*⁶⁴ found that the contact between two atomically flat pieces of identical insulators can result in charge separation, of which the amount of charge increases as increasing contact time. Their experimental result suggests that the charge amount Q , instead of being proportional to the contact area A , actually scales with its square root $A^{1/2}$. They assert that the contact electrification between identical materials is driven by the inherent, molecular-scale fluctuations in the surface composition or structure of the material. The concept that random, microscopic-level fluctuations may translate into macroscopic charge accumulation may also be used to describe the famous Lord Kelvin' thunderstorm experiment, where electrostatic induction comes from the oppositely charged water drops from the same bucket. In some cases, temperature difference can also cause the asymmetry, such as charge transfer resulting from ice collision, which plays a crucial role in the development of the strong electric fields and induce lightning in clouds.

1.3.2 AFM study of contact electrification

With the advances in nanotechnology, atomic force microscopy (AFM)-based techniques have been developed and applied to investigate the fundamental aspects of friction. Especially, the electrical-AFM techniques such as Kelvin probe force microscopy (KPFM), electrostatic force microscopy (EFM), and conductive AFM (C-AFM) have shown their powerful capability in

characterizing contact electrification phenomenon at nanoscale. KPFM works based on ascertaining contact potential difference between the probe tip and the sample, which provides a direct characterization of triboelectrification-induced surface potential variation. Mostly, KPFM works based on a dual-pass mode, where the AFM probe records the surface topography in the first scanning, followed by a topography retracing with a lift height.⁶⁵ The surface potential difference can be determined either by amplitude or frequency modulation of the AFM probe, with a low frequency AC electrical signal (1~2 Hz) adding to the high frequency one (of the order of KHz, for driving the cantilever oscillation).⁶⁵

As we discussed in the last chapter, it is proposed that the contact electrification may not necessarily follows a uniform charge transfer process with single direction. This is experimentally proved by H. T. Baytekin *et al.*⁶⁶ by observing a mosaic surface charge distribution in contact electrification with KPFM technique. Fig. 1-12 A shows the comparison between the traditional view of uniform charge transfer and the non-uniform mosaic charge transfer. The KPFM surface potential mapping shows that whereas each contact-electrified piece develops a net charge of either positive or negative polarity, each surface supports a random “mosaic” of oppositely charged regions of nanoscopic dimensions (Fig. 1-12B). These mosaics of surface charge have the same topological characteristics for different types of electrified dielectrics and accommodate significantly more charge per unit area than previously thought.

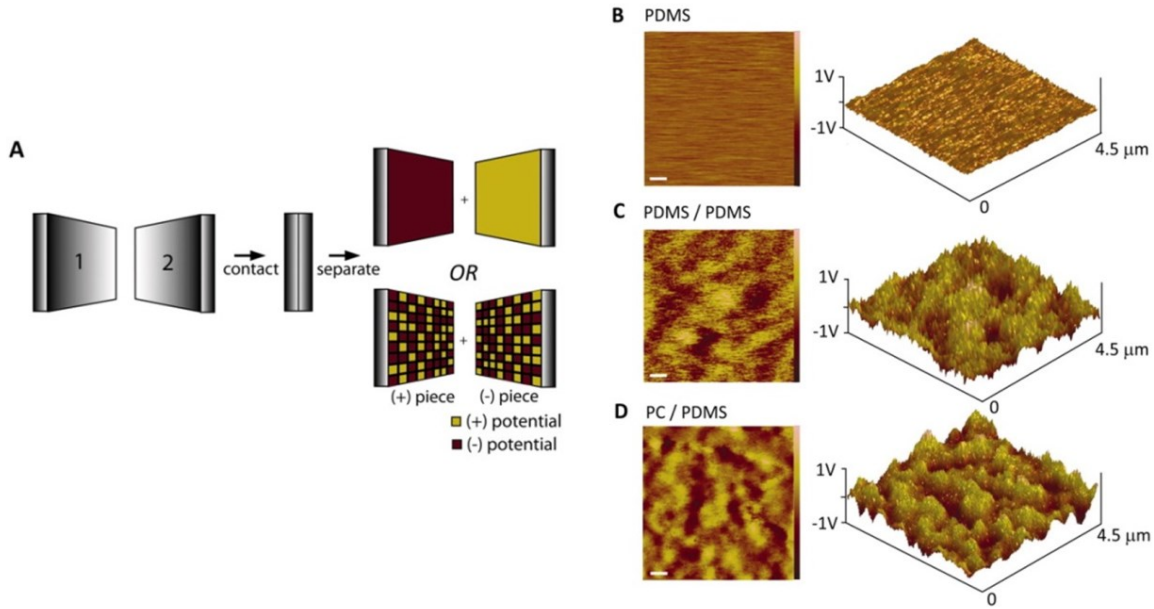


Figure 1-12 Possible scenarios of contact electrification and experimental KFM surface potential maps. The traditional view (A, upper right) assumes that upon contact and separation, one surface charges uniformly positively and the other, uniformly negatively. In contrast, the mosaic picture (A, lower right) assumes that each surface is a union of regions that have different propensities to accept or donate charge. The map in (B) corresponds to PDMS before contact electrification. Contact-charged surfaces in (C) and (D) feature a mosaic of (+) and (-) regions. (C) PDMS charged negatively against another PDMS piece. (D) PC contact-charged positively against PDMS.⁶⁶ (Reprinted with permission from AAAS Publishing Group)

Yu Sheng Zhou, *et al.*⁶⁷ conducted an in-situ quantitative study of nanoscale triboelectrification and patterning. They systematically characterized the triboelectric charge distribution, multifriction effect on charge transfer, as well as subsequent charge diffusion on the dielectric

surface. By knowing the surface potential difference ΔV , the surface charge density can be calculated by (suppose a SiO₂ dielectric layer is the substrate):

$$\sigma = \frac{\Delta V \epsilon_0 \epsilon_{\text{SiO}_2}}{t_{\text{SiO}_2}}, \quad (1-20)$$

Where where ϵ_0 is the vacuum dielectric constant and ϵ_{SiO_2} and t_{SiO_2} are the relative dielectric constant and thickness of SiO₂, respectively. It is found that the triboelectric charges accumulated from multifriction and eventually reached to saturated concentrations of $(-150 \pm 8) \mu\text{C}/\text{m}^2$ and $(105 \pm 6) \mu\text{C}/\text{m}^2$, respectively. The charge diffusion coefficients on SiO₂ surface were measured to be $(1.10 \pm 0.03) \times 10^{-15} \text{ m}^2/\text{s}$ for the positive charge and $(0.19 \pm 0.01) \times 10^{-15} \text{ m}^2/\text{s}$ for the negative charges.

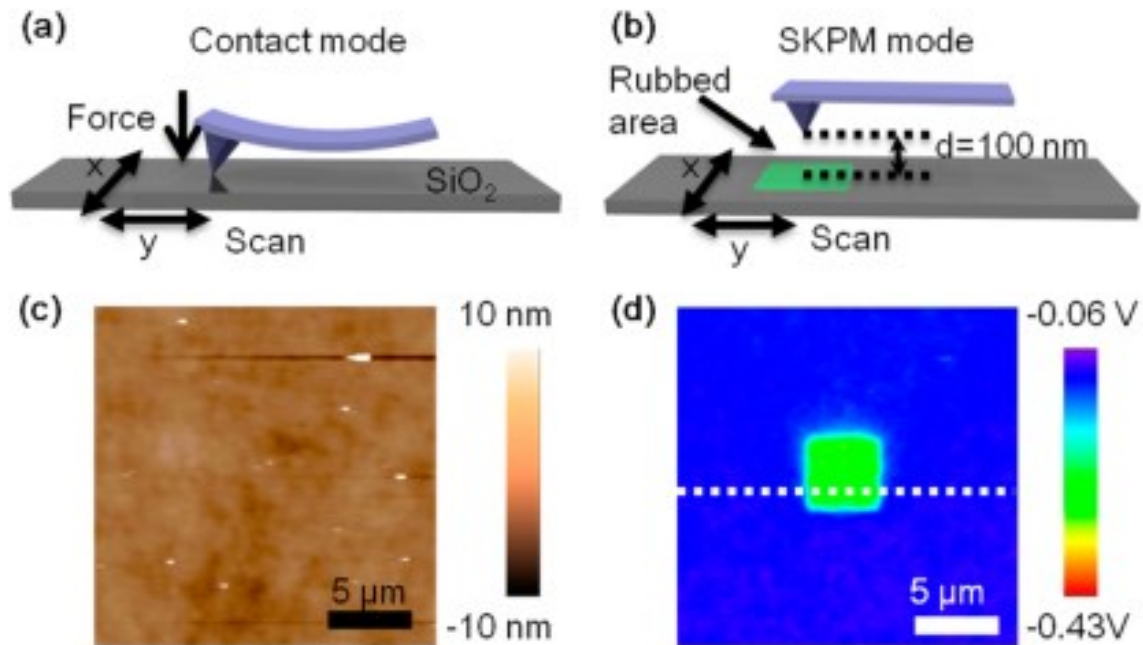


Figure 1-13 (a) triboelectric charge generation by friction between AFM probe and SiO₂ and (b) subsequent surface potential characterization in the KPFM mode. (c) AFM topography the sample and its corresponding (d) KPFM surface potential mapping.⁶⁷

(Reprinted with permission from ACS publications)

They also demonstrated using triboelectrification between the AFM probe and sample for nanopatterning of surface charges without assistance of external electric field, which is considered to a promising potential application for directed self-assembly of charged nanostructures for nanoelectronic devices. (Fig. 1-14)

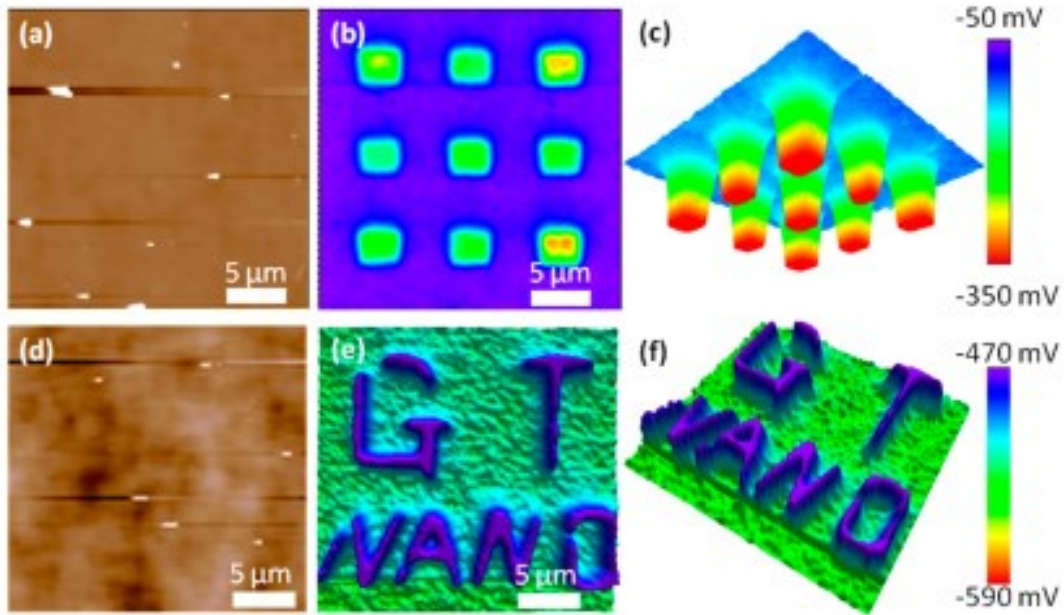


Figure 1-14 Patterning of the surface triboelectric charges on an insulator surface. Patterning of negative charges: (a) surface topography image and (b) 2D and (c) 3D images of charge density after patterning. Patterning of positive charges: (d) surface topography image and (e) top and (f) side views of 3D images of charge density after patterning ⁶⁷

(Reprinted with permission from ACS publications)

Y. Zhou *et al.*⁶⁸ also introduced an approach to purposely manipulate the contact electrification process both in polarity and magnitude of the charge transfer through an applied electric field between two materials. A theoretical model was derived to elaborate the dependence of transferred charge density on different parameters such as externally applied bias and the

thickness of dielectric layer at the equilibrium status. It is found that the modulation effect is stronger on a thinner dielectric layer.

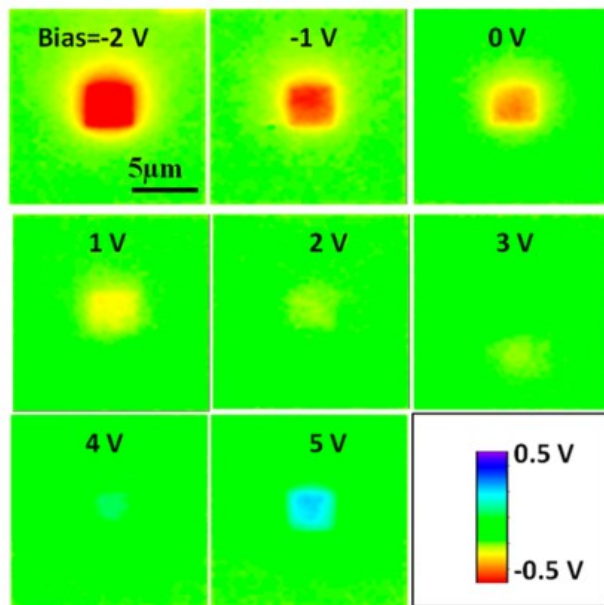


Figure 1-15(a) Surface potential distributions of the Parylene film including the areas that were rubbed by Pt coated AFM tip at different bias from -2 to 5 V ⁶⁸ (Reprinted with permission from ACS publications)

S. Li *et al.*⁶⁹ suggested that the contact electrification during the scanning process itself may introduce an additional contribution in the overall signal, which may causes misinterpretation of the characterization result. It happens when the probe enters into the repulsive force regime of a tip-sample interaction, and this can be detected by the phase shift of the probe vibration. It is suggested that decreasing the free amplitude, increasing the set-point amplitude, and using probes with a lower spring constant may suppress the interference.

K.Y. Lee *et al.*⁷⁰ reported a controllable charge transfer by ferroelectric polarization mediated triboelectricity. They found that both the amount and direction of charge transfer in triboelectric

materials can be controlled by ferroelectric polarization state, which is achieved by poling the ferroelectric co-polymer sample with the scanning of biased AFM tip. The results show that the surface potential of the positively (negatively) poled area becomes smaller (larger) after rubbing the film surface with the AFM tip. (Fig. 1-16).

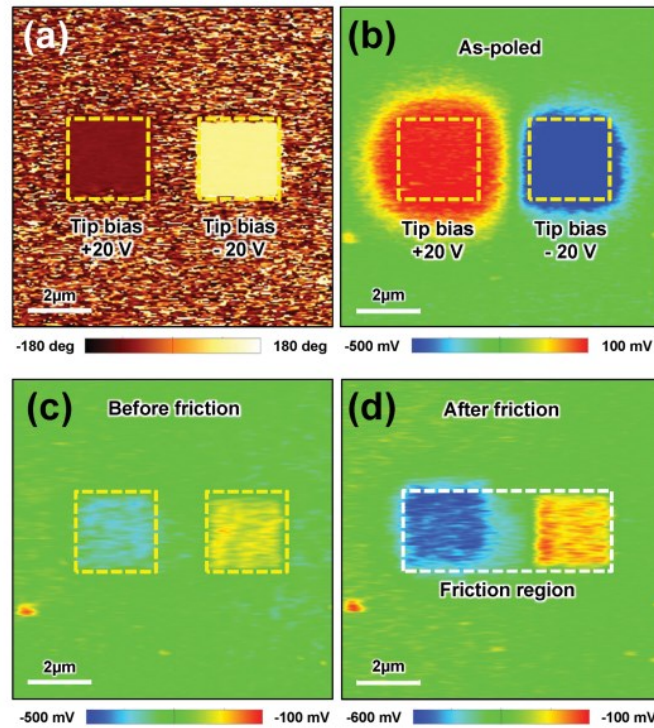


Figure 1-16 Polarization switching and surface potential distribution of the P(VDF-TrFE) thin film: a) PFM phase image after the poling process and b) KPFM images after the poling process, c) after 12 h of the poling process, and d) after friction over an area indicated with white dotted line of the P(VDF-TrFE) thin film. The left (right) yellow dotted square indicates the positively (negatively) poled area by applying +20 V (-20 V) to the conductive probe during the poling process.⁷⁰ (Reprinted with permission from Wiley Publishing Group)

Recently, a new phenomenon of tribo-tunneling direct current generation has been discovered by our group. C-AFM techniques, which are able to collect topography and current distribution simultaneously, have been used to characterize the phenomenon.⁵⁷ It is found that the phenomenon has a different working principle comparing to the traditional dielectric displacement a.c. triboelectricity generation. Instead, it is related to the direct charge transfer at the frictional interface under a thermodynamically non-equilibrium condition. This will be detailed presented in Chapter 3 and 4.

1.4 Energy dissipation in friction

To understand the fundamental aspects of energy dissipation in friction is to understand how mechanical kinetic energy ($1/2 mv^2$) of the moving parts is converted into various excitations of the surrounding media. Upon frictional contact, the fluctuating electric fields emanating from charges in the two materials would interact with each other, dissipating the frictional energy in multiple ways, including phonon excitation, electronic excitation, and chemical reaction. More often than not, those elementary dissipation processes may happen simultaneously, which brings the difficulty of quantitative study of each individual contribution. Nevertheless, a lot of effort has been dedicated to understand those dissipation pathways by nimbly designed experiments with a strict control of experimental conditions.⁵⁹

The atomic-scale mechanism of friction is summarized by ‘Prandtl-Tomlinson’ model, which has been successfully used as the basis for many mechanism studies of friction.⁷¹ According to this model, the friction process for a single asperity is simplified as the one dimensional movement of a point mass in a periodic atomic interface potential with wave number k . An external force F is applied to the point mass. It is assumed that the movement is damped proportional to velocity v ⁷¹:

$$m\ddot{x} = F - \eta\dot{x} - N \sin kx, \quad (1-21)$$

where x is the coordinate of the body, m its mass, F the external force acting upon it, η the damping coefficient, N the amplitude of the periodic force, and k the wave number.



Figure 1-17 Prandtl-Tomlinson model: A point mass in a periodic potential.

Equation 1-21 indicates that, every macroscopic movement of the body, from a microscopic point of view, is a superposition of a constant speed and a periodic oscillation. The interface atoms undergo an elastic displacement, resulting in a collective vibration of surface crystal structure. The vibrational energy of the interface atoms is transferred to the bulk material in the form of propagating phonons. It can also be damped by electron-hole pair excitations in metals. Under a sufficiently high external force, the friction can also lead to rupture of surface chemical bonds.

Generally, phonon contribution is considered to dominate the frictional energy dissipation process, as we all have the experience of warming our hands by rubbing them against each other. Given a metal or semiconductor is involved however, electronic excitation may also play an important role manifesting itself in different ways. It is proposed that the moving atoms may drag the electrons dissipating frictional energy into the excitation of electrons to unoccupied levels (electron-hole pair excitation).^{59,72} A variety of phenomena are related to the coupling between atomic motion and electrons, such as resistivity variation of thin films due to adsorption^{73,74}, the appearance of infrared anti-absorption peaks⁷⁵⁻⁷⁷, and the broadening of vibrational peaks^{78,79}. Experimental results suggest that a noncontact friction may result from the

electric field fluctuations between two materials sliding close to each other without real contact.

⁸⁰ It is also found by AFM studies on semiconductor that electronic effects can contribute appreciably in the friction between contacting solids. ^{81,82}

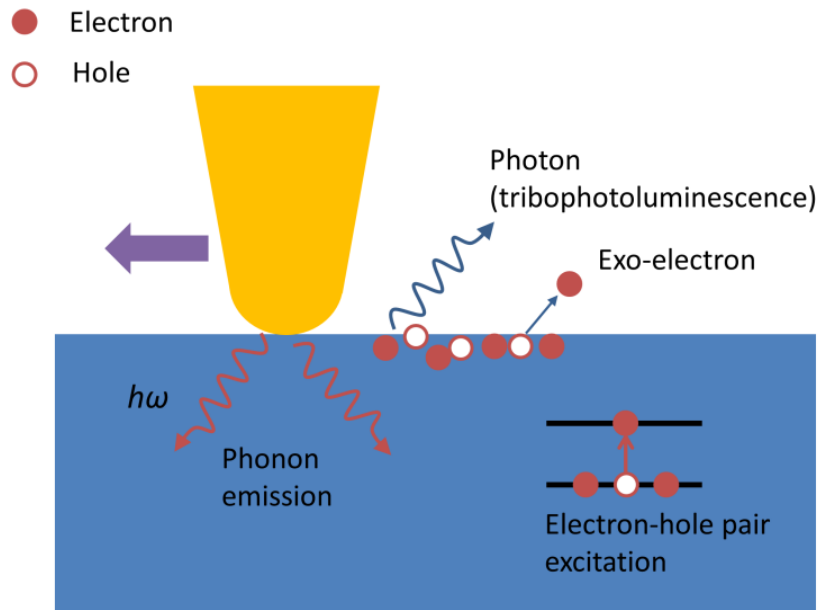


Figure 1-18 Different energy dissipation in friction as mediated by phonon emission and electron–hole excitation, exo-electron emission, and triboluminescence

Frictional electronic excitation may decay via various routes as well. Heat can be generated by e-h pair recombination. High-energy electron excitations may give rise to electron emission (exoelectron emission) in surfaces with low work function, which is due to the relaxation of non-equilibrium electronic states. It is believed that the electrons are excited by the remaining energy being stored in the defects of materials. Tagawa *et al.*⁸³ reported that, the larger friction coefficient is, the higher exo-electron emission intensity can be observed. Exoelectron emission

has shown broad application, including disruptions in coatings, rupture of oxide films, and detection of cracks.

Triboluminescence is another phenomenon that is related to electronic excitation. It is an optical phenomenon in which light is generated through the breaking of chemical bonds in a material when it is pulled apart, ripped, scratched, crushed, or rubbed. It is a well-known phenomenon that people can observe in daily life by wrinkling their cloth or peeling adhesive tape. Prof. Seth Putterman group from UCLA has been working on triboluminescence for years. In their research, X-ray signal has been detected by high speed data collection equipment when tape is peeled apart.⁸⁴ The experimental results suggest that the flash contain nanosecond X-ray pulses whose emissions are correlated with radio frequency pulses and with slips in the force required to peel the pressure-sensitive adhesive tape. They have developed and commercialized the idea of peeling the adhesive tape as triboelectric x-ray sources.

Chapter 2 Methodology and experimental section

The phenomenon of tribo-tunneling direct current generation was first discovered in MoS₂ material system, where pulsed laser deposition (PLD) method has been used for sample preparation. To reveal the basic features and working mechanism of the fundamental process, a series of systematic C-AFM based studies, combined with material characterization and finite element method (FEM) simulation, have been conducted. To further reveal the charge transfer process, insulator thickness dependent experiments have been conducted in metal-Si frictional materials system, where SiO₂ layer with different thickness were finely prepared and controlled by atomic layer deposition (ALD) method. For the proof of concept, a microprobe-based generator prototype has been developed. Electrical measurement has been performed to evaluate the power generation performance of the prototype.

2.1 Material synthesis

2.1.1 Synthesis of MoS₂ thin film by pulsed laser deposition (PLD)

Pulsed laser deposition (PLD) is a physical vapor deposition (PVD) technique where a high-power pulsed laser beam is focused inside a vacuum chamber to strike a target of the material that is to be deposited. This material is vaporized from the target (in a plasma plume) which deposits it as a thin film on a substrate (such as a silicon wafer facing the target). This process can occur in ultrahigh vacuum or in the presence of a background gas, such as oxygen which is commonly used when depositing oxides to fully oxygenate the deposited films.

MoS₂ thin films were synthesized via PLD. Cleaned substrates were placed onto a sample stage and loaded into a PLD chamber (Excel Instruments, Mumbai, India) which also contained a stoichiometric MoS₂ target. The chamber was evacuated to a pressure in the order of $\sim 10^{-5}$ Torr prior to deposition in order to ensure the quality of the film by preventing oxidation of the substrate and the deposited film. The chamber was subsequently pressurized by Ar gas to 11 mTorr and the substrate was heated to 500 °C prior to deposition. Ultrashort (20 ns width) pulses from an excimer laser (KrF, $\lambda=248$ nm, Coherent, GmbH) were directed to the target with a fluence of 1.2 J/cm² energy density at a 5 Hz repetition rate. Deposition time was 300 seconds, and the substrate was allowed to cool down to room temperature in Ar atmosphere.

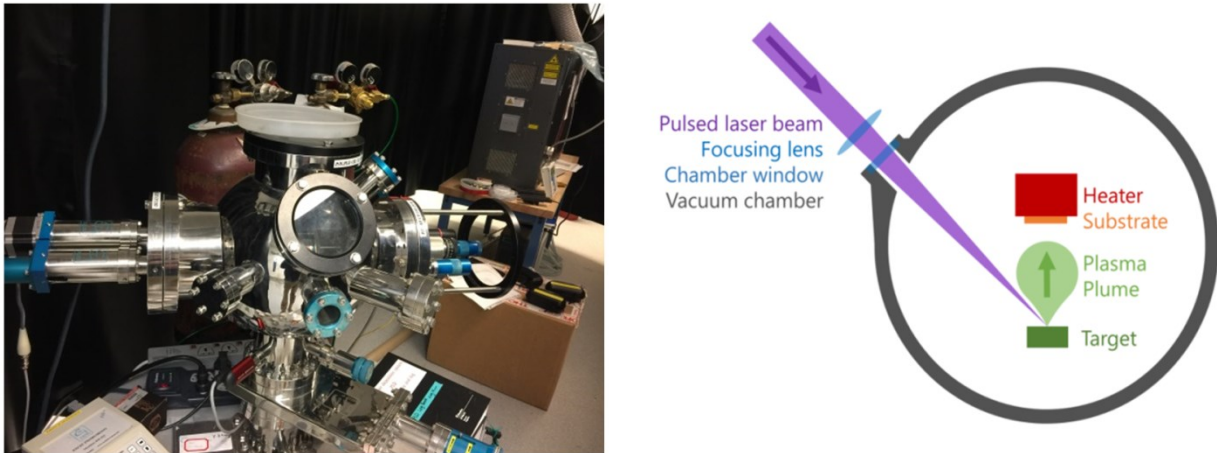


Figure 2-1 Pulsed laser deposition system (left); Working principle of PLD (right).

2.1.2 Synthesis of SiO_x by Atomic layer deposition (ALD)

Samples with different SiO_x thicknesses were prepared by plasma-enhanced atomic layer deposition (PEALD) in an ALD-150LX reactor (Kurt J. Lesker, USA).

Tris(dimethylamino)silane (3DMASi, Sigma-Aldrich), oxygen gas (Praxair), and argon gas (99.999%, Praxair) were used as precursor, reactant and carrier gas, respectively.⁸⁵ Temperature settings for 3DMASi ampoule, ALD valve, reactant line, chamber wall, and substrate is room temperature, 95 °C, 110 °C, 50 °C, and 50 °C, respectively. Each ALD cycle includes: 3DMASi dose (0.04 s), Ar purge (8 s), oxygen plasma dose (8 s) and Ar purge (5 s). The ALD film growth was in situ monitored by spectroscopic ellipsometry (SE, M2000DI from J. A. Woollam). The growth rate of SiO_x was about 0.92 Å/cycle, characterized with a Cauchy model.

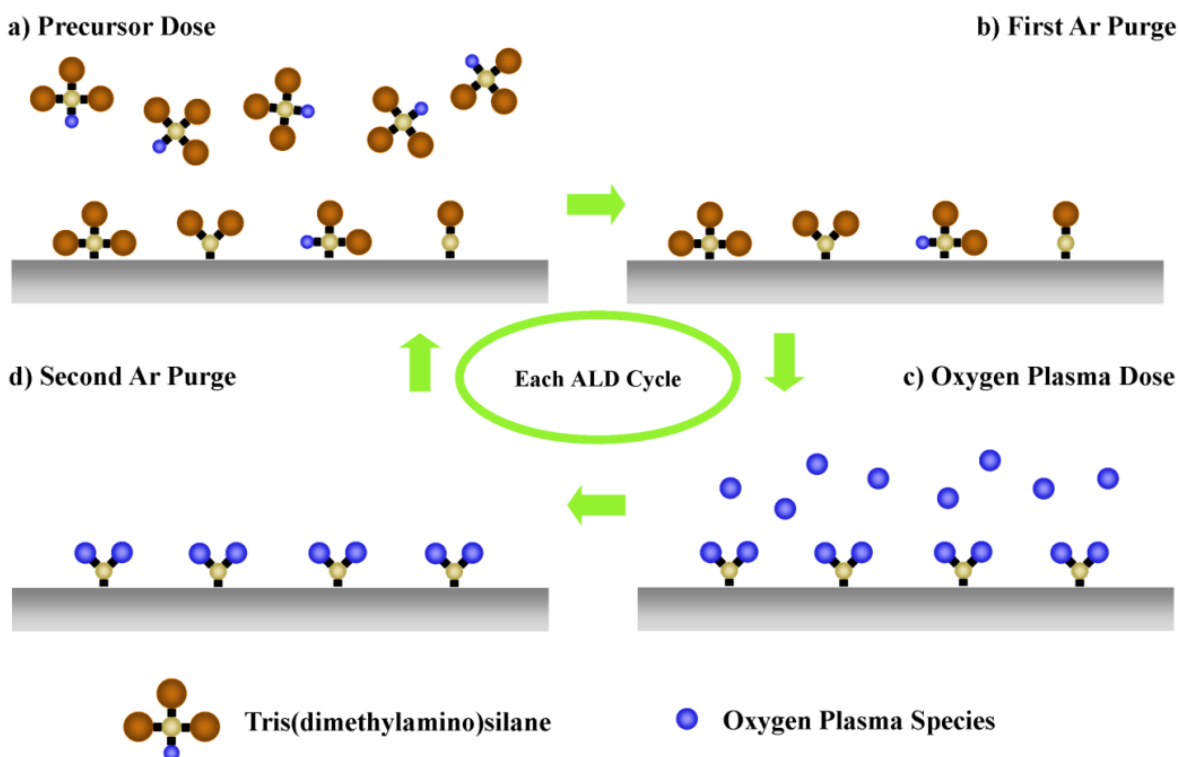


Figure 2-2 Schematics of the PEALD SiO_x deposition process. Each ALD cycle includes four steps: a) 3DMASi dose (0.04 s), b) Ar purge (8 s) to remove reacted precursor molecules and byproducts, c) Oxygen plasma dose (8 s), and d) Ar purge (5 s) to remove reacted plasma species and byproducts.

2.1.3 Preparation of electrical contact by magnetron sputtering

In order to achieve a complete circuit of the nanogenerator system, a bottom ohmic contact is needed. It has been reported that Ag forms a good ohmic contact with MoS₂, and also facilitates the MoS₂ growth by PLD. An electron beam evaporation system (Kurt J. Lesker) has been used to deposit Ag on the Si wafers. The thickness of Ag film is 30 nm, with a 5 nm Cr adhesion layer deposited in advance.

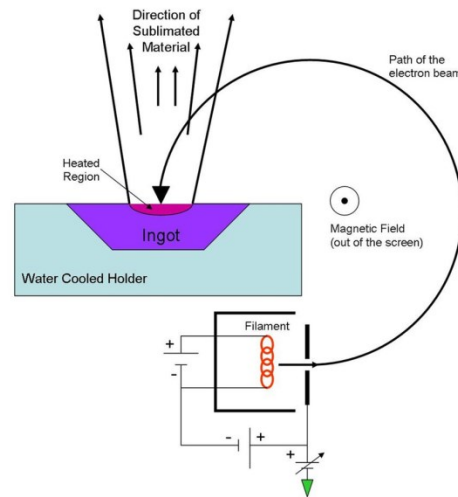


Figure 2-3 Electron beam evaporation system (left); Working principle of electron beam evaporation system (right).

As for the doped Si system, Al is used for achieving the ohmic contact due to its low work function. The magnetron sputtering system (Kurt J. Lesker) has been used to deposit 100 nm bottom contact.

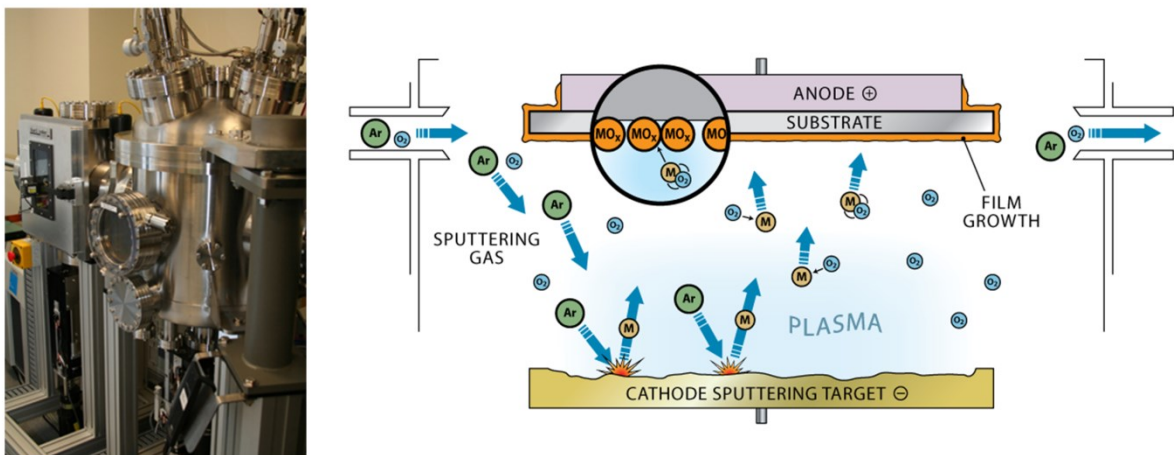


Figure 2-4 Magnetron sputtering system (left); Working principle of magnetron sputtering system (right).

2.2 Material Characterization

2.2.1 Scanning electron microscopy (SEM) characterization

SEM characterization was conducted with a Zeiss Sigma 300 VP-FESEM. It has been reported that MoS₂ can be successfully deposited on Ag using PLD, while other metallic materials such as Al, Ni, Cu show poor capabilities as substrates.⁸⁶ From Fig. 2-5, MoS₂ grains with good crystal quality are discernible. Hexagonal shape of MoS₂ is evident in the magnified image, which is in line with the AFM results in main text. Molybdenum disulfide is an inorganic compound composed of molybdenum and sulfur, which is classified as a transition metal dichalcogenide. All forms of MoS₂ have a layered structure, in which a plane of molybdenum atoms is sandwiched by planes of sulfide ions. These three strata form a monolayer of MoS₂. Bulk MoS₂

consists of stacked monolayers, which are held together by weak van der Waals interactions. Figure 2-7 shows the Wulff construction for a MoS_2 nanocluster exposing the (0001) basal plane.

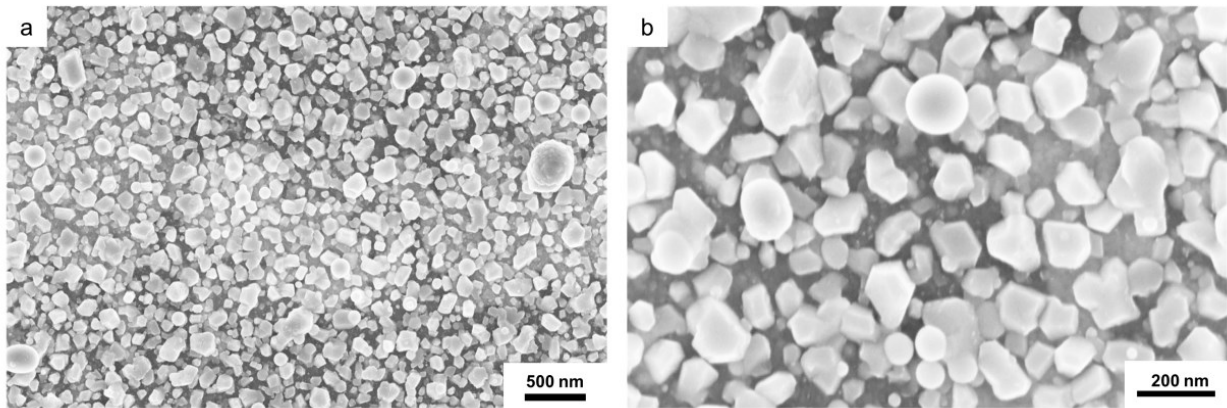


Figure 2-5 SEM image of MoS_2 thin film deposited by PLD

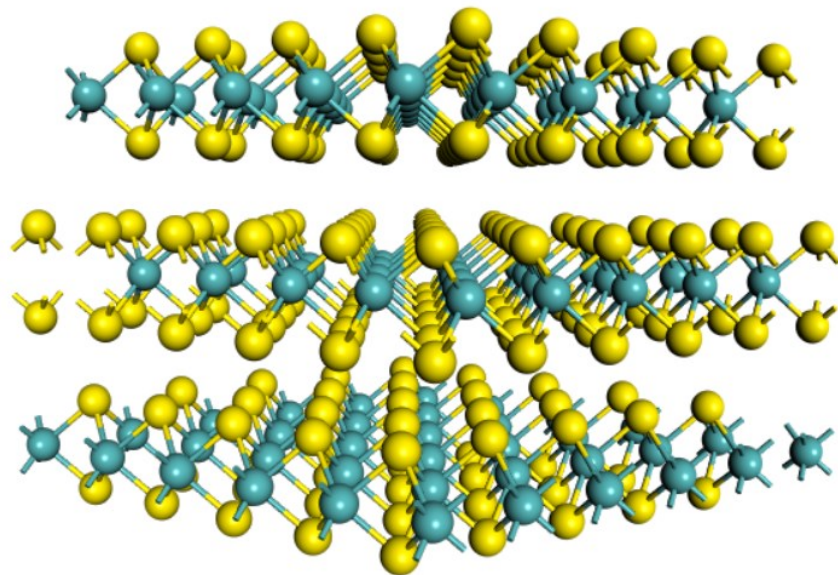


Figure 2-6 3D layer structure of MoS_2

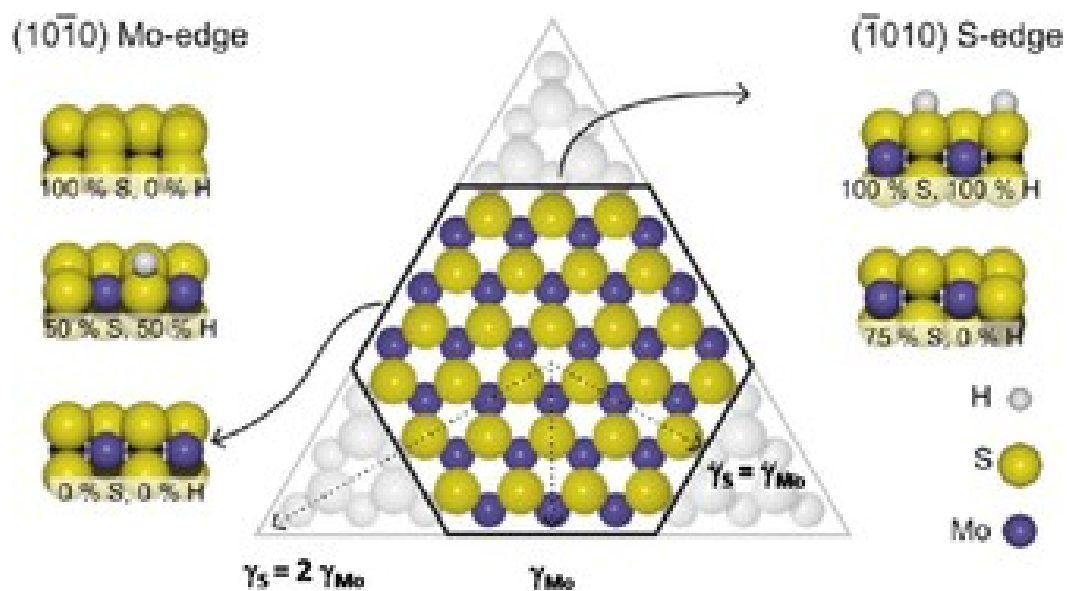


Figure 2-7 Wulff construction for a MoS₂ nanocluster exposing the (0001) basal plane⁸⁷

(Reprinted with permission from Wiley Publishing Group)

2.2.2 Raman spectra characterization

Raman spectroscopy characterization was conducted with a Thermo Nicolet Almega XR Raman Microscope. The observed peaks correspond to the E and A_{1g} mode oscillation of Mo-S bonding.⁸⁶

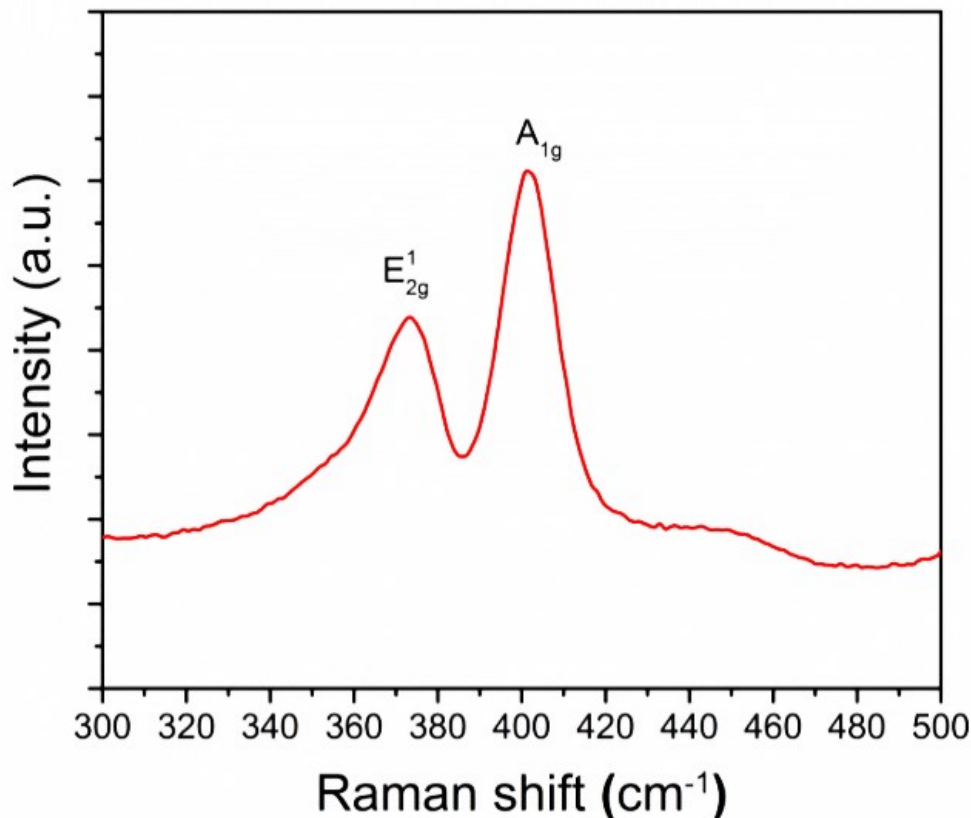


Figure 2-8 Raman spectra of MoS₂ thin film deposited by PLD

2.2.3 X-ray photoelectron spectroscopy (XPS) characterization

XPS characterization was conducted with a Kratos AXIS 165. The collected spectra were analyzed by using the CasaXPS software package. As shown in Fig. 2-9, the doublet Mo⁴⁺ 3d_{5/2} and Mo⁴⁺ 3d_{3/2} peak located at 229.6 eV and 237.8 eV are attributed to the Mo⁴⁺ state in MoS₂ (marked as orange).^{86,88} Doublet peaks at 232.7 eV and 235.9 eV are attributed to the Mo⁶⁺ state of MoO₃ (marked as blue).^{88,89} S 2s core level peak at 226.7 eV and 228.4 eV corresponds to the S²⁻ state in MoS₂ (marked as purple) and other surface S species such as oxysulfide compounds and SH species (marked as green), respectively.⁸⁸ When exposed to air, S vacancies on the PLD-

synthesized MoS₂ thin film surface may react with atmospheric oxygen, which give rise to the formation of MoO₃.⁸⁹ The observed non-uniform current distribution for the single grain may be due to stoichiometry fluctuation on MoS₂ surface as revealed by the XPS result. The existing surface Mo oxide species would degrade the electrical conductivity of those regions.

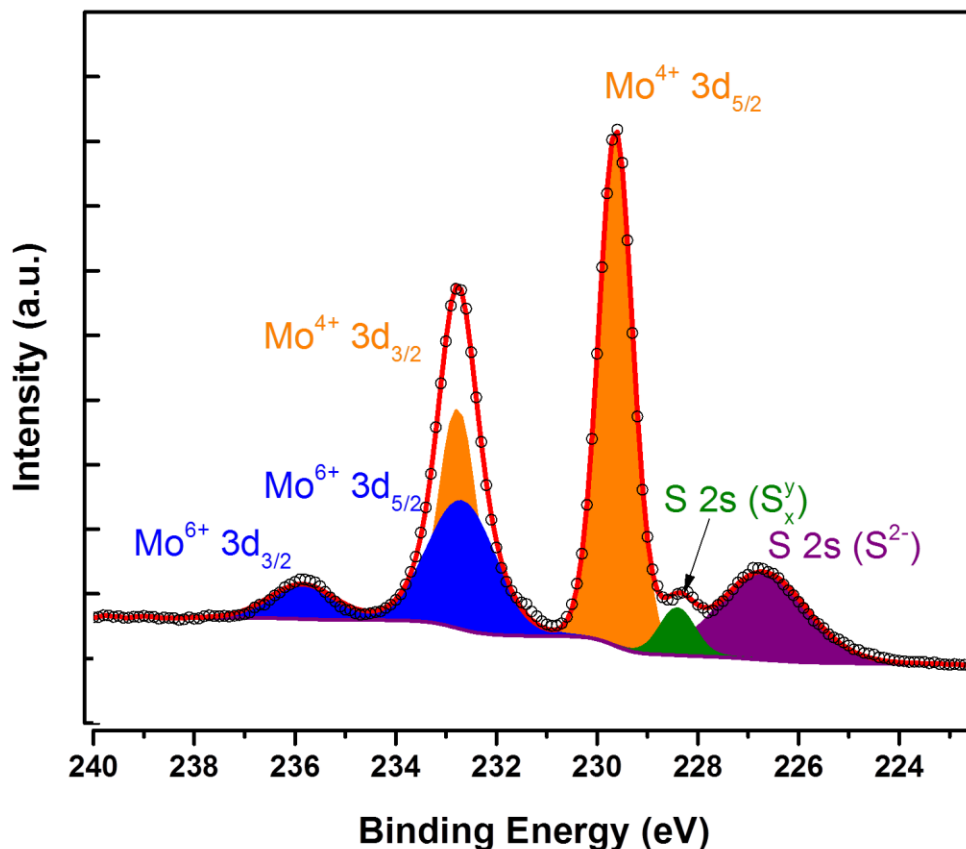


Figure 2-9 Decomposition of Mo 3d and S 2s XPS peaks of MoS₂ thin film deposited by PLD. Black hollow circles are raw data points. Red solid curve is the fitted result.

2.3 Conductive-atomic force microscopy (C-AFM) characterization

2.3.1 AFM operation

Developed in 1986 by Binnig, Quate, and Gerber as a collaboration between IBM and Stanford University, the atomic force microscope (AFM) grew out of the STM and today is by far the more prevalent of the two. Unlike STMs, AFMs can be used to study insulators, as well as semiconductors and conductors. The probe used in an AFM is a sharp tip, typically less than 5 μm tall and often less than 10 nm in diameter at the apex. The tip is located at the free end of a cantilever that is usually 100–500 μm long.

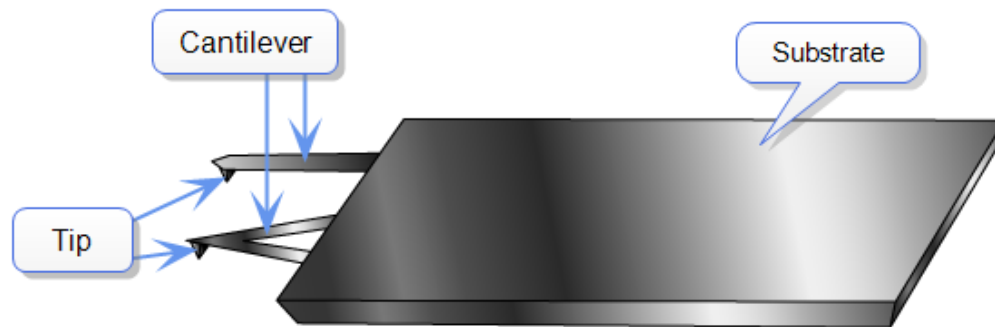


Figure 2-10 Illustration of an AFM cantilever system. The AFM cantilever may have different shape such as rectangular or triangular as shown in the illustration. They are connected with a base, which can be mounted on a tip holder, and excited by a piezoelectric actuator

Forces between the tip and the sample surface cause the cantilever to bend, or deflect. A photodiode detector measures the cantilever deflections as the tip is scanned over the sample, or the sample is scanned under the tip. The measured cantilever deflections allow a computer to generate a map of surface topography. Several forces typically contribute to the deflection of an

AFM cantilever. To a large extent, the distance regime (i.e., the tip-sample spacing) determines the type of force that will be sensed:

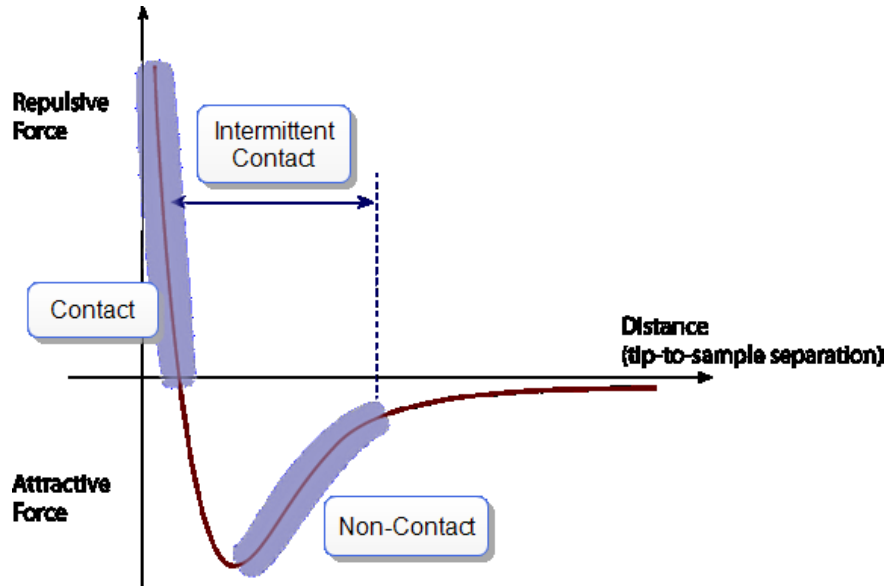


Figure 2-11 The effect of tip-to-sample distance on the force interaction between tip and sample

The forces between the tip and sample change as the separation distance changes. As the tip and the sample are gradually brought together, their atoms begin to weakly attract each other. This attraction increases until the atoms are so close together that their electron clouds begin to repel each other. This electrostatic repulsion progressively weakens the attractive force as the separation continues to decrease. The total force goes through zero and finally becomes positive (repulsive).

Most AFMs use optical techniques to detect the position of the cantilever. In the most common scheme, a light beam from a laser diode bounces off the back of the cantilever and onto a position-sensitive photo-detector (PSPD). As the cantilever bends, the position of the laser beam on the detector changes. The ratio of the path length between the cantilever and the detector to the length of the cantilever itself produces amplification. As a result, the system can detect sub-Ångstrom vertical movement at the free end of the cantilever, where the tip is located.

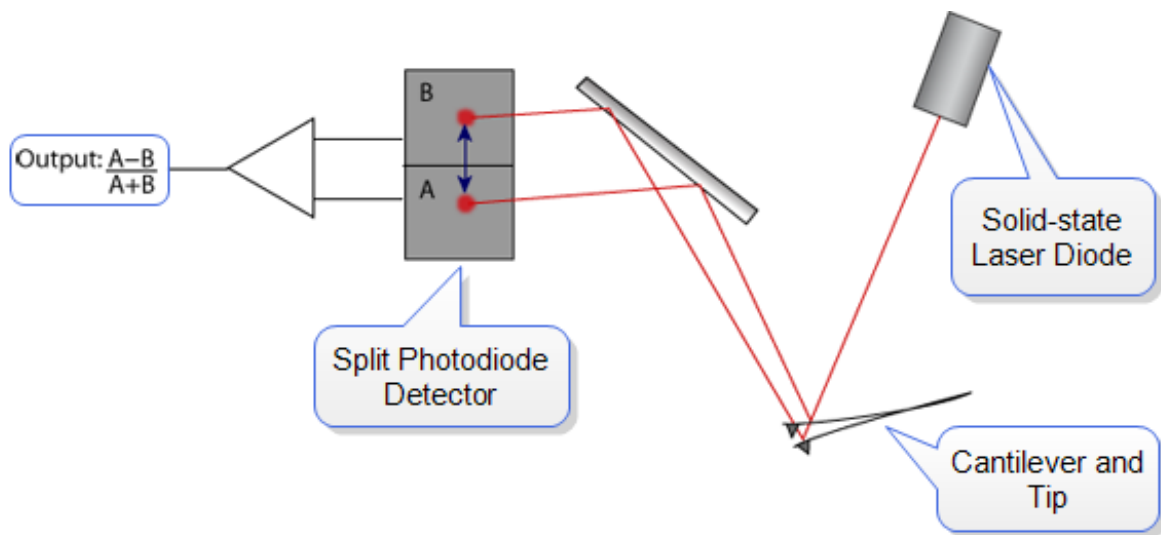


Figure 2-12 Illustration of a basic AFM system

Variations on this basic scheme are used to measure topography as well as other surface features. There are numerous AFM Modes. Each is defined primarily in terms of the type of force being measured and how it is measured. In this thesis, conductive-AFM based on contact scanning mode is the main mode being used for the study of tribo-tunneling phenomenon.

In contact AFM, the tip is in perpetual contact with the sample. The tip is attached to the end of a cantilever with a low spring constant—lower than the effective spring constant of the force holding the atoms of most solids together. As the scanner gently traces the tip across the sample

(or the sample under the tip), the contact force causes the cantilever to bend to accommodate changes in topography. The Contact Mode feedback loop maintains a constant deflection between the cantilever and the sample by vertically moving the scanner at each (x,y) data point to maintain a “setpoint” deflection. By maintaining a constant cantilever deflection, the force between the tip and the sample remains constant.

The force is calculated from Hooke's Law: $F = -kx$, where F , k , x is the force, cantilever spring constant, and cantilever deflection, respectively. Force constants usually range from 0.01 to 1.0 N/m, resulting in forces ranging from nN to μ N in an ambient atmosphere. The distance the scanner moves vertically at each (x,y) data point is stored by the computer to form the topographic image of the sample surface. Operation can take place in ambient and liquid environments.

2.3.2 Determine Cantilever Spring Constant by Thermal Tune

The thermal tune method, based on measuring thermal noise, provides an automated and quick determination of cantilever spring constant. Often, users prefer to determine cantilever spring constant by thermal tune is often preferred over The added mass method (which is more demanding and time-consuming) or estimation from cantilever geometry (which has a large uncertainty factor). The measurement data consists of a time interval of the deflection signal in contact Mode (*i.e.*, with no driving oscillation applied electronically) at thermal equilibrium, while the cantilever is suspended away from any solid surface. Brownian motion of surrounding (air) molecules imparts random impulses to the cantilever during the sampling. The resulting function of time is Fourier transformed to obtain its Power Spectral Density (PSD) in the

frequency domain. Integrating the area under the resonant peak in the spectrum yields the power associated with the resonance.

Expressing the dynamics of the cantilever as a harmonic oscillator by the total system energy (the Hamiltonian), the average value of the kinetic and potential energy terms are both $1/2k_B T$ according to the Equipartition Theorem, where T is temperature in Kelvin, and k_B is Boltzmann's constant (1.3805×10^{-23} J/K)

In particular, for the potential energy,

$$\langle \frac{1}{2} m \omega_0^2 z^2 \rangle = \frac{1}{2} k_B T, \quad (2-1)$$

Where $\omega_0 = (k/m)^{1/2}$ is the resonant angular frequency, m is the effective mass, and z is the displacement of the free end of the cantilever. The “angle” brackets indicate average value over time. Simplifying, the temperature and average displacement determine the cantilever spring constant:

$$k = (k_B T) / \langle z^2 \rangle = k_B T / P, \quad (2-2)$$

The original displacement time-series is Fourier transformed to segregate other broadband noise contributions from the narrowband thermal noise around resonance. By integrating the area under the resonance in the PSD, while excluding both the noise floor and the “shoulders” to either side of the resonance peak, only the power, P , of the thermal cantilever fluctuations is included. The latter is equal to the mean square of the time-series data. Fig. 2-13 shows the power P vs. cantilever frequency f of the AFM cantilever ACCESS-EFM (AppNano, US). A spring constant k of ~ 5 N/m is determined by the thermal tune method.

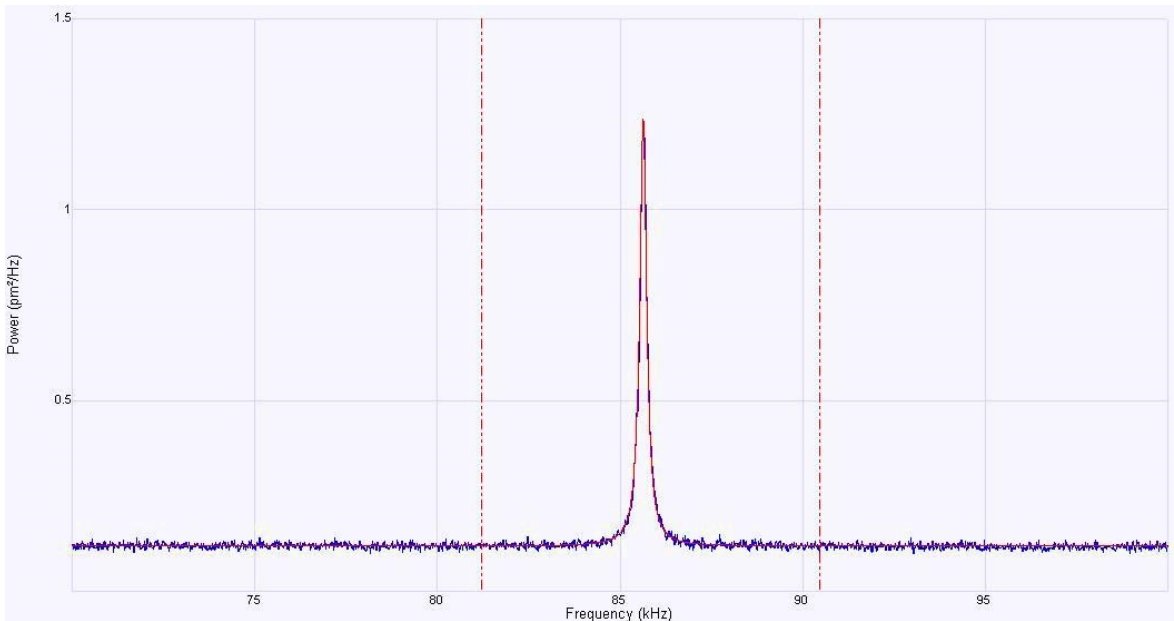


Figure 2-13 Thermal tune of the AFM cantilever

2.3.3 C-AFM measurement

Tunneling Atomic Force Microscopy (TUNA) extends to high resistance sample surfaces the original SPM implementation, scanning tunneling microscopy of conductive samples. TUNA measures sub-picoampere tip/sample currents through highly resistive samples.

The geometry of the tip determines the lateral resolution, which is roughly equal to the end radius of the tip. With the tip at virtual ground, a selectable bias voltage is applied between the conductive tip and sample (see Figure 2-14). While scanning in Contact Mode, a linear amplifier with a range of 80fA to 120pA senses the current passing through the sample. By maintaining a

constant force between tip and sample, simultaneous topographic and current images are generated, enabling the direct correlation of local topography with electrical properties.

TUNA is especially useful for evaluating dielectric films subject to breakdown, such as silicon dioxide, SiO₂, and transistor gate oxide. Tip/sample tunneling current depends on film thickness, leakage paths, possibly caused by defects, charge traps and tip geometry. TUNA is also used to test the integrity of tribological films, such as Diamond-Like-Carbon (DLC) as used in magnetic recording head/disk interfaces, and conductivity in small structures, such as light-emitting polymers and carbon nanotubes.

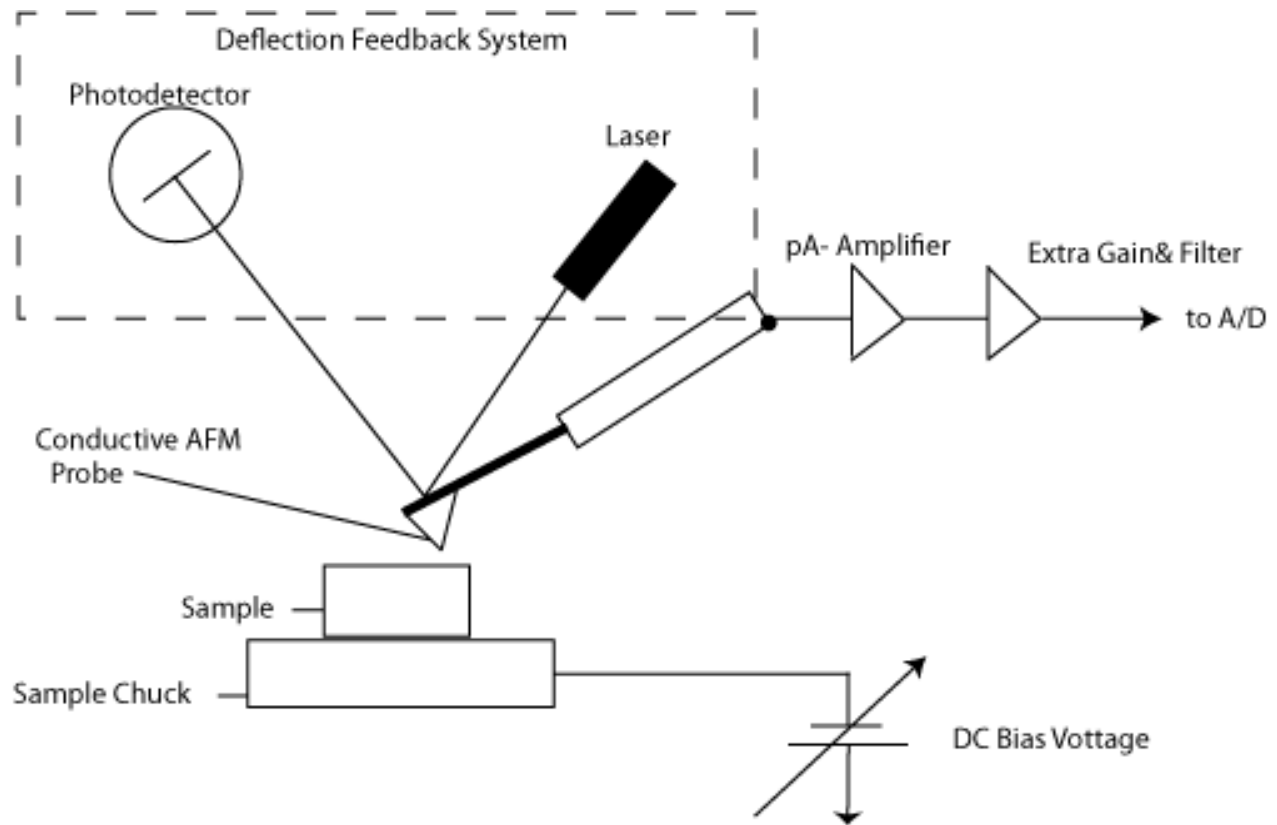


Figure 2-14 Tunneling AFM (and Conductive AFM) Block Diagram

In this thesis, C-AFM measurement was performed with a Dimension Icon (Bruker, USA) AFM and Pt/Ir coated conductive-AFM probes (ACCESS-EFM, AppNano, USA). The bottom electrode of the sample was electrically connected to the AFM sample stage with conductive tape. During the measurement, the topographic image and current signal were simultaneously collected by contact-mode scanning and a current amplifier, respectively. The contact force was determined by calibrating cantilever deflection sensitivity and spring constant. For the I - V spectra, C-AFM mapping was scanned first, followed by moving the AFM probe to the designated spots on the scanned region and recording the current output as a function of sample bias.

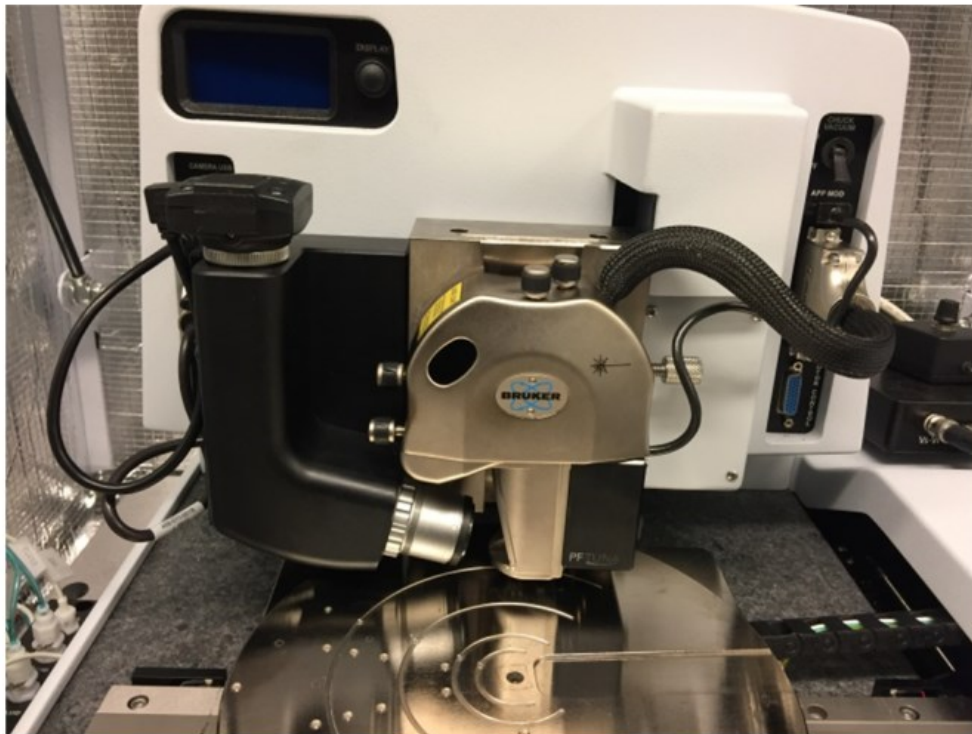


Figure 2-15 Bruker Icon C-AFM system with TUNA module

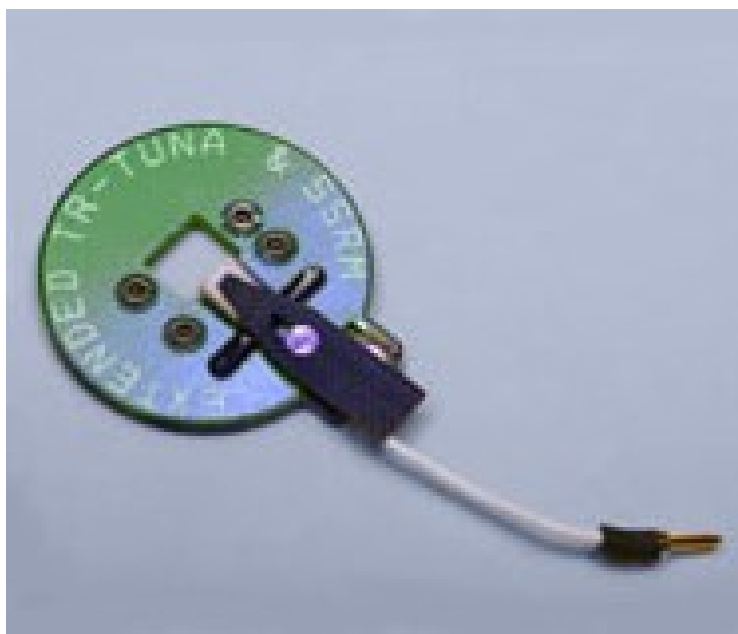


Figure 2-16 Bruker DTRCH-AM tip holder for TUNA module

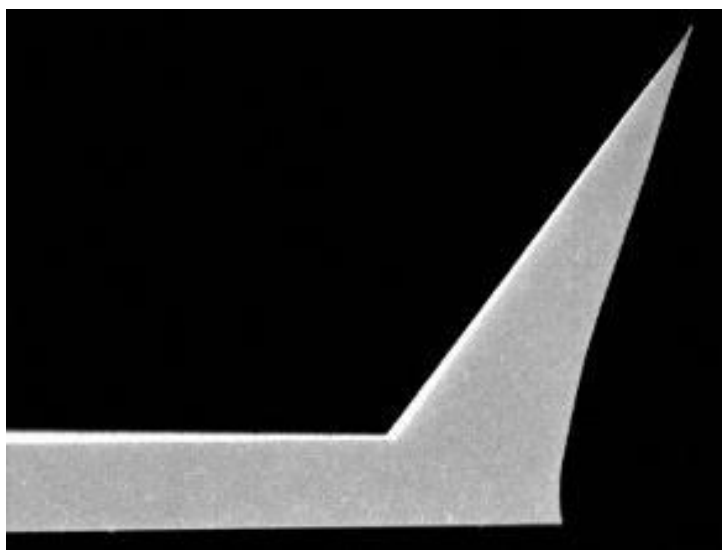


Figure 2-17 SEM image of ACCESS-EFM Pt/Ir-coated conductive AFM tip from AppNano,

US.

Platinum-Iridium (Pt-Ir) coated probes offer excellent conductivity and good mechanical stability are optimal for contact as well as non-contact EFM techniques. Fig. 2-17 shows the SEM image of ACCESS-EFM Pt/Ir-coated conductive AFM tip from AppNano, US. Table 2-1 summarized its major parameters.

Table 2-1 Parameters of ACCESS-EFM probes

Parameter	ACCESS-EFM
k (N/m)	2.7
f (kHz)	60
Length	245
Width (μm)	52
Thickness (μm)	2.8
Tip ROC (nm)	30
PtIr thickness (nm)	25 \pm 5

2.3.4 Probe-sample contact area estimation

To model the contact geometry of asperities, a simplified model consisting of a sphere with radius R and a planar substrate can be used. If adhesion interaction is not considered, the well-known Hertz model based on classical continuum mechanics describes the elastic deformation of the contact bodies as⁵⁹:

$$A = \pi \left(\frac{RL}{K} \right)^{2/3}, \quad (2-3)$$

where R is AFM tip radius, L is the load (contact force F) K is the reduced Young's modulus given as $K = \frac{3}{4} \left(\frac{1-\nu_s^2}{E_s} + \frac{1-\nu_t^2}{E_t} \right)$, where E_t and E_s are Young's moduli and ν_t and ν_s are the Poisson ratios of the tip and the sample, respectively.

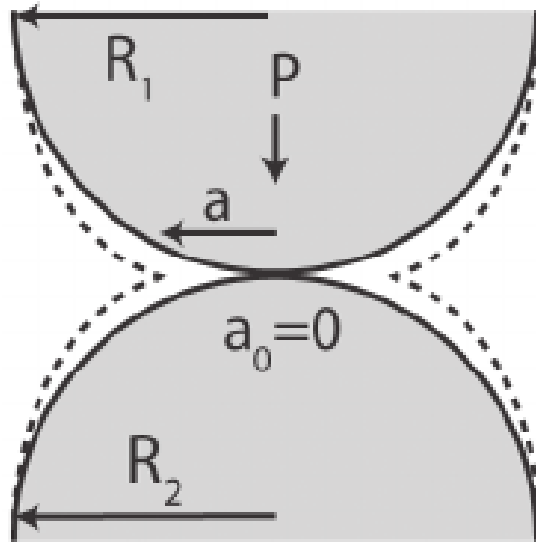


Figure 2-18 Schematic of Hertz model

A more sophisticated model is the JKR (Johnson–Kendall–Roberts) model, which neglects long-range forces outside the contact area but considers short-range forces inside the contact region that manifest in the surface energy or work of adhesion, γ ⁵⁹:

$$A = \pi \left\{ \frac{R}{K} \left[L + 3\pi R\gamma + (6\pi RL + (3\pi R\gamma)^2)^{1/2} \right] \right\}^{2/3}, \quad (2-4)$$

The term $2\pi R\gamma$ can be considered as an ‘additional load’ L_{ad} , which is determined by the “pull-off” force. The “pull-off” force is defined as that where the contact is unstable against thermal fluctuations, which causes a transition to zero area. It can be measured from force–distance curves. JKR is applicable when contact between the tip has a large radius and the materials are highly adhesive and compliant.

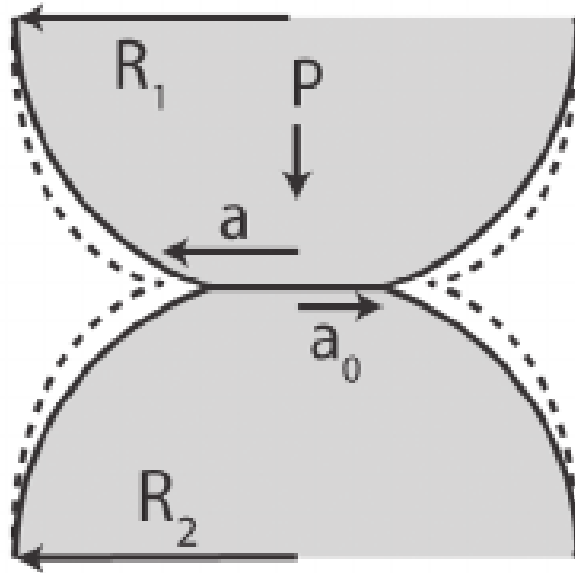


Figure 2-19 Schematic of JKR model

A third model is the DMT (Derjaguin–Muller–Toporov) model considering only long-range adhesion forces from inside and outside the contact area. Since the PLD deposited MoS₂ materials or the silicon material in this study are considered as hard and weakly adhesive materials, the contact area in our AFM experiments is approximated by the DMT model.⁵⁹ According to the DMT model, A is given by⁵⁹:

$$A = \pi \left[\frac{R}{K} (L + 2\pi R\gamma) \right]^{2/3}, \quad (2-5)$$

Adhesion measurement was conducted with PeakForce QNM mode (Bruker, USA). The average adhesive force can be used for tip-sample contact area estimation.

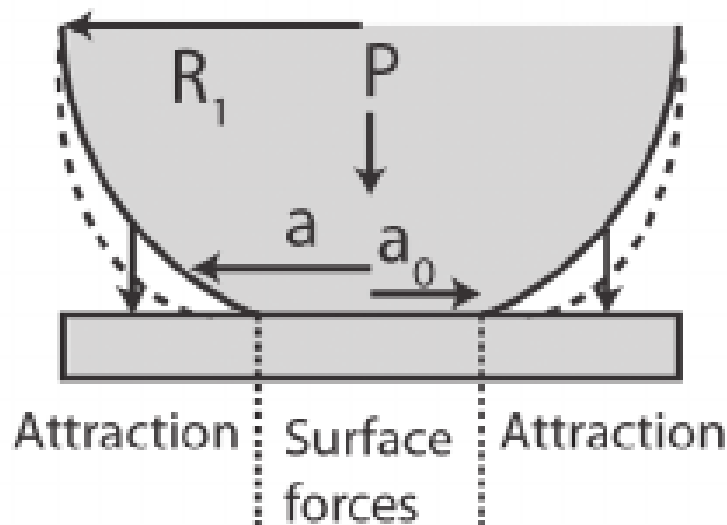


Figure 2-20 Schematic of DMT model

Briefly, the PeakForce QNM mode works based on force-distance curves obtained for each image pixel. The z-piezo in PeakForce QNM mode is driven with a sinusoidal waveform (rather than a triangular waveform in conventional modes) at a low frequency (2 KHz), which allows direct force control of damaging lateral forces. Fig. 2-21 shows the schematic force-distance

curves of a typical PeakForce QNM-AFM measurement during approach and retraction of the tip. The peak force value of the force-distance curves is used as the imaging feedback parameter, and the maximum pull-off force during the retraction of the tip is designated as adhesion force.⁹⁰

The source of the adhesion force can be any attractive force between the tip and sample. In air, van der Waals, electrostatics, and forces due to the formation of a capillary meniscus can all contribute with the relative strengths of the contributions depending on such parameters as Hamaker constants, surface charges, and hydrophilicity. For example, if either sample or the probe surface is hydrophilic, a capillary meniscus will typically form, leading to higher adhesion that extends nanometers beyond the surface. For polymers in which the long molecules serve as a meniscus, the adhesion can extend tens of nanometers beyond the surface. The adhesion typically increases with increasing probe end radius. Simple models based on surface energy arguments predict the adhesion to be proportional to the tip end radius. The area below the zero force reference (the horizontal line in the force curve) and above the withdrawing curve is referred to as “the work of adhesion.” The energy dissipation is dominated by work of adhesion if the peak force set point is chosen such that the non-elastic deformation area (the hysteresis above the zero force reference) in the loading/unloading curve is negligible compared to the work of adhesion.⁹⁰

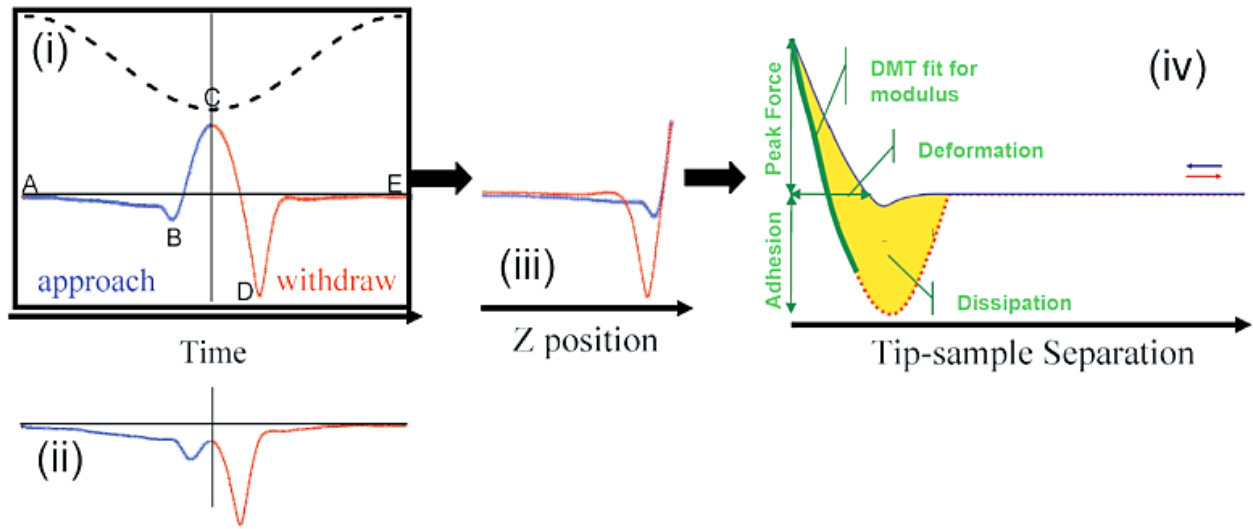


Figure 2-21 Force curves and information that can be obtained from them: (i) Plot of force and piezo Z position as a function of time, including (B) jump-to-contact, (C) peak force, (D) adhesion; (ii) Plot of force vs. time with small peak force. (iii) A traditional force curve eliminates the time variable, plotting Force vs. Z piezo position; (iv) For fitting purposes it is more useful to plot force vs. separation where the separation is calculated from the Z piezo position and the cantilever deflection.

2.4 Finite Element Method (FEM) simulation

The FEM simulation of electric field distribution at tip-sample interface was carried out utilizing the 2D electrostatic module in COMSOL Multiphysics software. The MoS₂ thin film was modeled by a 500 nm × 40 nm slab with a dielectric constant $\epsilon=11$. The tip had a conical shape with a spherical apex with a radius of 30 nm. A 1500 × 1500 nm slab was applied as air atmosphere. The tip-sample contact was modeled by an indentation distance determined by DMT model. While the initial electric potential $V_0=8$ mV was set at the tip-sample interface, the rest of tip surface was assigned to be “Zero charge” and the tip end was set to be “Ground” boundary condition.

2.5 Electrical measurement of the generator performance

2.5.1 V, I and P output as a function of load resistance R

The V and I data were collected by a Keithley 2450 SourceMeter SMU (Tektronix, USA). Unlike the high impedance in polymer-based TENGs (high resistance and capacitance), the equivalent circuit components in our case is relatively simpler, which can be approximated as a DC voltage source, an internal resistance and an external resistance connected in series. Therefore, V, I and P can be modeled as:

$$V = V_{oc}R/(R + r), \quad (2-6)$$

$$I = V_{oc}/(R + r), \quad (2-7)$$

$$P = V_{oc}^2R/(R + r)^2, \quad (2-8)$$

2.5.2 Charging capacitor with DC triboelectricity

The $V-t$ data was collected by a Keithley 2450 SourceMeter SMU (Tektronix, USA).

Theoretically, the $V-t$ curve can be fitted by:

$$V = V_b \left(1 - e^{-\frac{t}{RC}}\right), \quad (2-9)$$

where $V_b \approx V_{oc}$ and $R \approx r$.

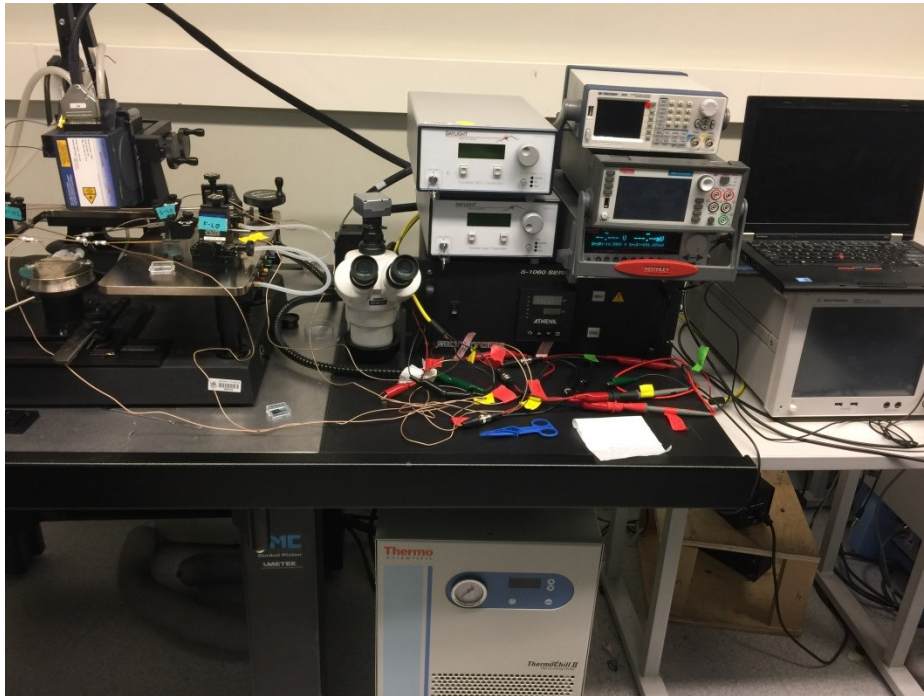


Figure 2-22 Electrical testing platform

Chapter 3 Direct-current triboelectricity generation by sliding-Schottky nanocontact on MoS₂ multilayers

J. Liu, A. Goswami, K. Jiang, F. Khan, S. Kim, R. McGee, Z. Li, Z. Hu, J. Lee and T. Thundat,

"Direct-current triboelectricity generation by a sliding Schottky nanocontact on MoS₂ multilayers." *Nature nanotechnology* (2018): 13, pages 112–116

(Reprinted with permission from Nature Publishing Group)

3.1 Introduction

Although it is known that frictional contact between two materials results in heat and charge carrier generation and many experimental demonstrations show energy harvesting using triboelectric nanogenerators (TENGs), the fundamental understanding of the charge transfer process during friction is still lacking.^{10,40,59} In conventional TENGs, dielectric displacement current, in AC form, is generated by vertical/horizontal movement of the contact materials with opposite electrostatic charges (Fig. 3-1a; $i=V\cdot\partial C/\partial t+C\cdot\partial V/\partial t$, where i , V , and C represent displacement current, voltage and electrode-sample capacitance, respectively).¹⁰ Those electrostatic charges are built up by the contact electrification process. However, the current density is largely limited due to the high impedance of the polymer-based system, with the best J in the order of 0.1-1 A/m² achieved so far.³² Additionally, rectifying approaches such as switching circuit³², rotating-disk configuration⁹¹ or double-wheel design⁹² have to be used to convert AC into DC. Meanwhile, other efforts have been dedicated to harvesting DC directly from mechanical energy. Piezoelectric DC excited by ultrasonic waves has been harvested by ZnO nanowire array but with low output power ($I\approx 0.5$ nA and $J\approx 2.5\times 10^{-4}$ A/m²).²² Recently, semiconducting polymer-metal Schottky contacts have been used for generating periodically changed DC ($J=0.1-1$ A/m²), indicating that the sliding metal-semiconductor system may convert mechanical energy directly into DC electricity based on different mechanism.²⁹

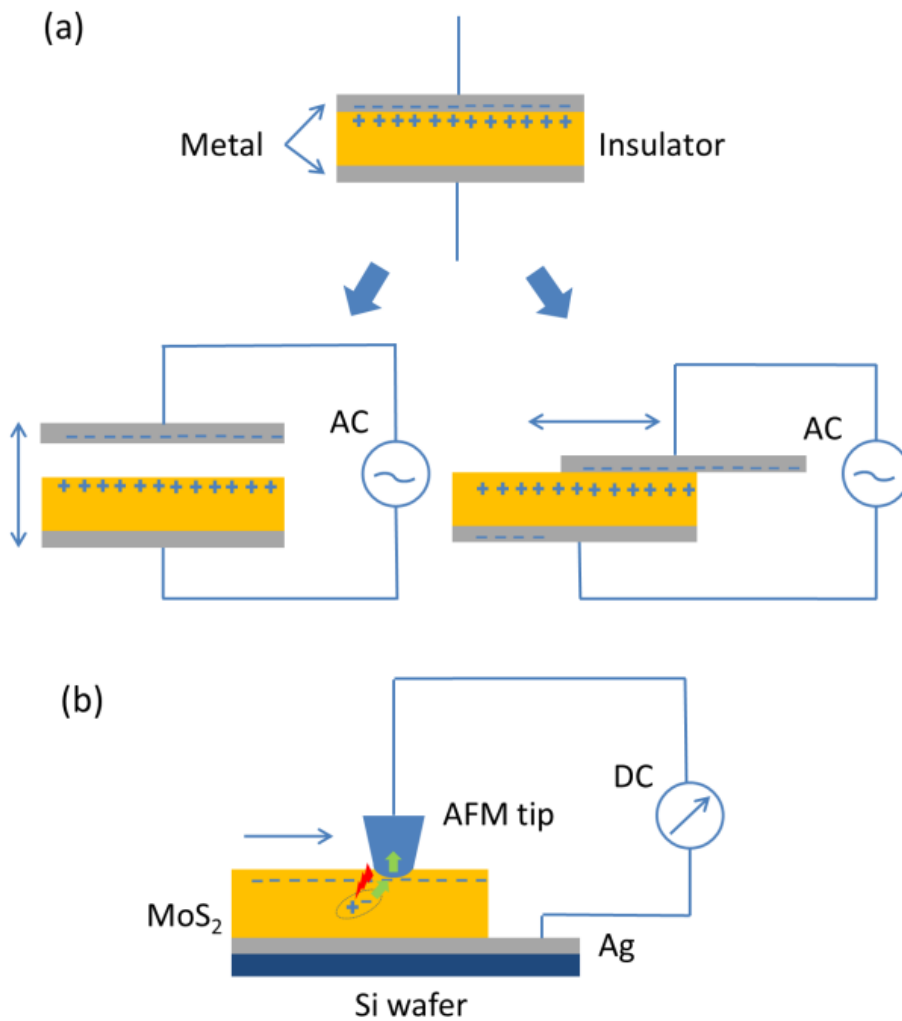


Figure 3-1 (a) Working principle of conventional TENGs considering a metal-insulator system. A demonstration of the contact electrification results in electrostatic charge distribution at the material interface (Top). By moving the two materials vertically (bottom left) or horizontally (bottom right), dielectric displacement AC can be harvested. (b) Schematic of nanoscale DC harvesting. MoS₂ thin film is deposited on Ag by PLD method. Pt/Ir-coated AFM tip slides in contact mode on the sample surface, which induces electronic excitation and carrier conduction.

3.2 Characteristics of C-AFM current output

Here, we demonstrate triboelectric DC generation by sliding a platinum-coated silicon AFM tip over a molybdenum disulfide (MoS_2) thin film synthesized by pulsed laser deposition (PLD) on a silver coated SiO_2/Si substrate (Fig. 3-1b)⁹³. Apart from its novel electrical,⁹⁴ optical⁹⁵ and catalytic⁹⁶ properties, MoS_2 has long been used as a dry lubricant in industries because of its excellent wear resistance originating from its layered structure.^{97,98}

Figure 3-2a shows a typical topographic AFM image of the synthesized MoS_2 sample with its characteristic hexagonal crystal morphology⁹⁹. Its corresponding C-AFM current map scanned with 5 nN contact force and zero bias is shown in Fig. 3-2b, where the DC signal with magnitude of 0.1-1 nA is observed. Cross-sectional line analysis of the image in Fig. 3-2d shows a continuous DC output on the single grain as shown in Fig. 3-2e.

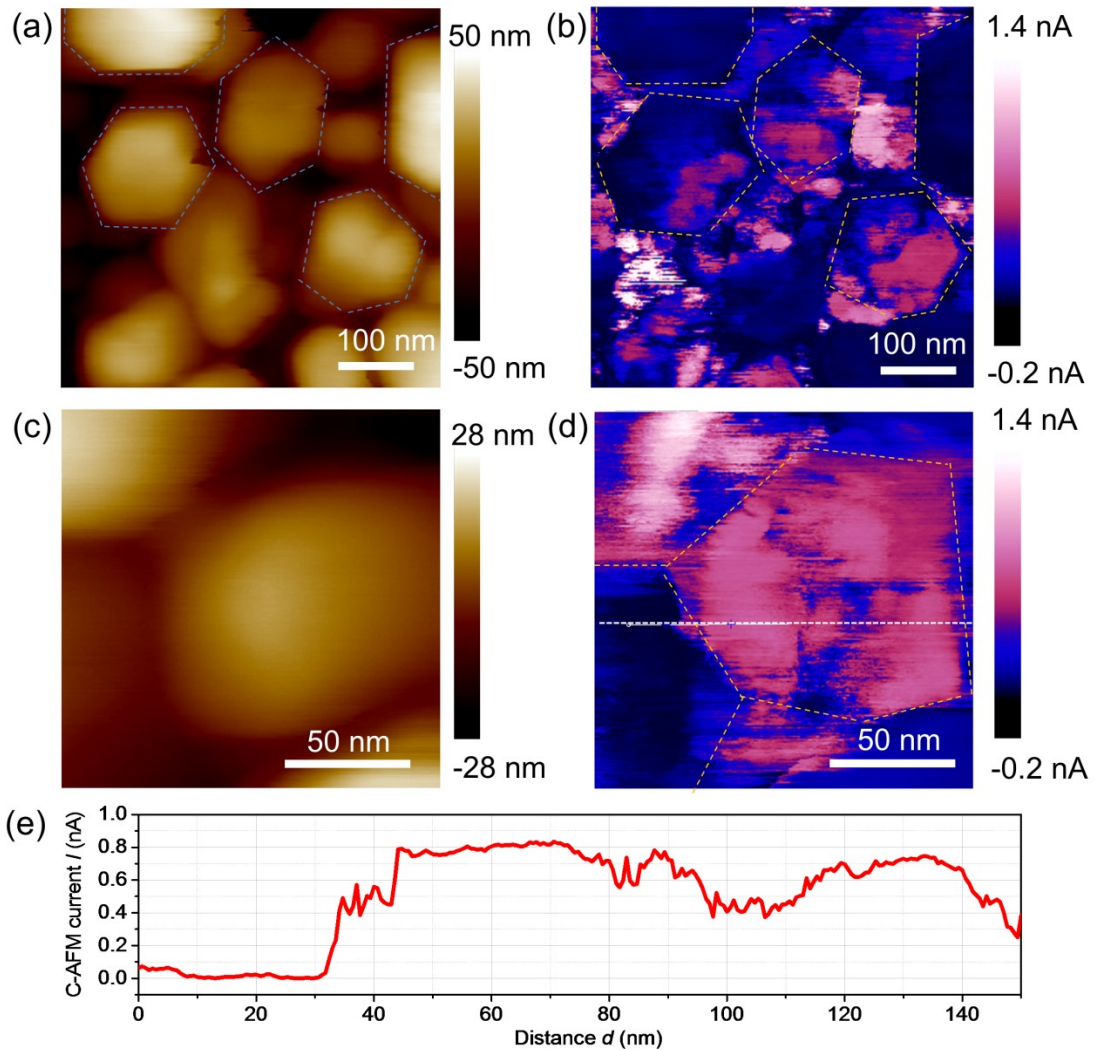


Figure 3-2 (a) and (c) are AFM topographic images of MoS₂ thin films at different scales and their corresponding C-AFM current mapping in (b) and (d). Sample bias of 0 V and contact force of 5 nN are used. The hexagonal single crystal morphology of MoS₂ is clearly visible and marked by orange dashed lines. Note: current direction in the C-AFM image is from tip to sample, *e.g.* electrons flow from sample to tip. (e) Cross-sectional line analysis of the tribo-excited current on (d) (marked by white dashed line). A continuous DC output can be seen on the single crystal upon scanning.

3.3 Artifact exclusion

Here, possible artifacts caused by environmental noise and laser irradiation have been excluded.

3.3.1 Current amplifier calibration

The conductive AFM module has been calibrated by using a standard 100 M Ω resistor provided by the manufacturer. In a typical procedure, the AFM probe was false engaged and a ramping test bias was applied to the C-AFM module. It can be seen from Fig. 3-3 that the slope of I - V curve matches perfectly with the standard resistor, indicating no data magnification from analysis.

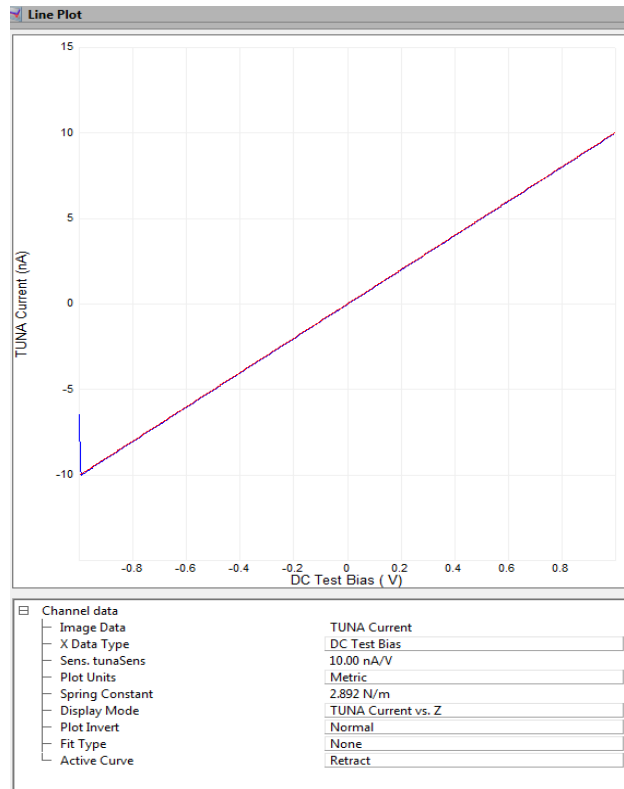


Figure 3-3 I - V characterization with a 100 M Ω standard calibration resistor.

3.3.2 False engagement

Upon false engagement, AFM probe scans above the sample surface without actual contact, in which case the system noise level can be investigated. It can be seen from Fig. 3-4 that the noise level in our experiment is around several pA, three orders smaller than the nA current signal upon contact scanning.

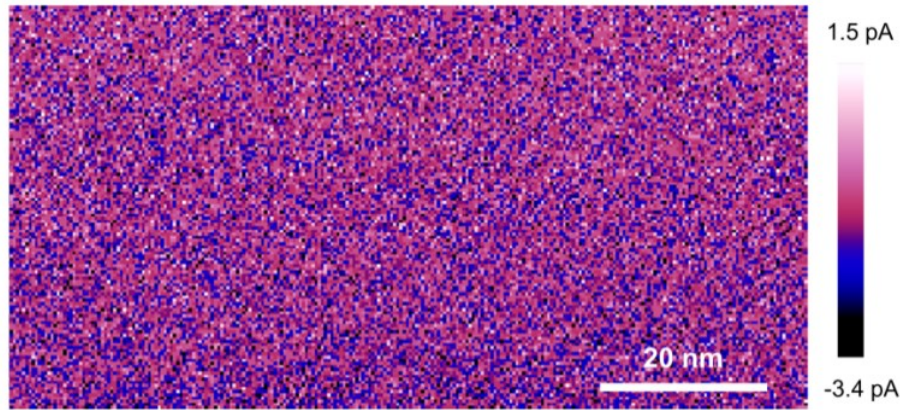


Figure 3-4 C-AFM current signal under false engagement

3.3.3 Laser spot position

To exclude the effect of AFM laser irradiation on the observed C-AFM current, we investigated the laser position-dependent current signal. As shown in Fig. 3-5, the C-AFM current signal is not sensitive to the laser spot position. As a matter of fact, the AFM laser spot is blocked by the AFM cantilever body, and reflected by the Pt/Ir coating on the top surface of cantilever.

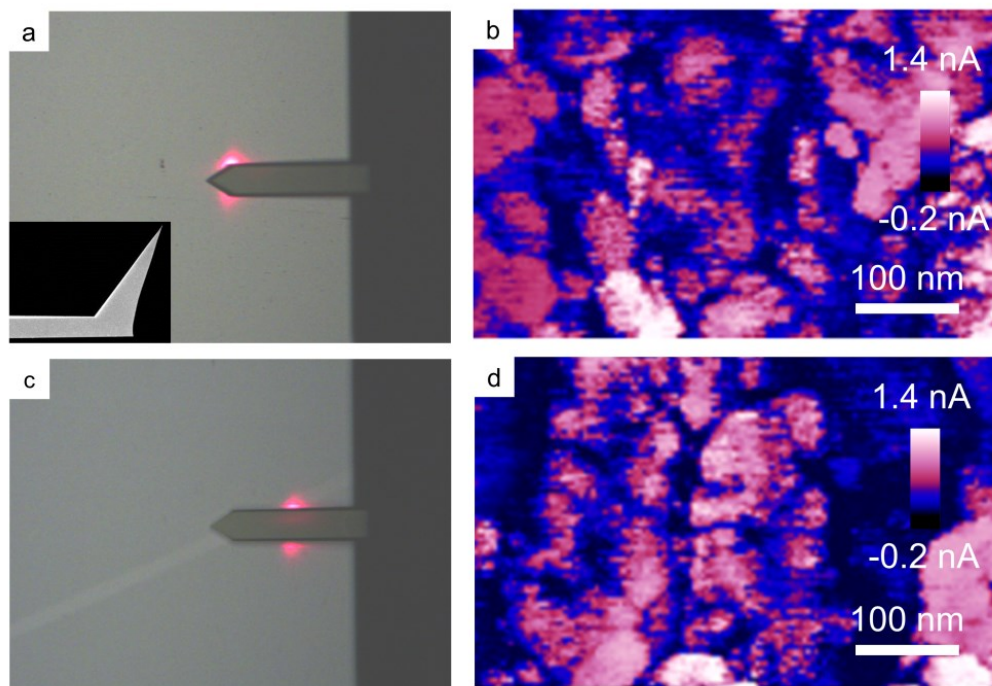


Figure 3-5 Laser position-dependent C-AFM signal on MoS₂. (a) and (b) are optical images of the AFM cantilever with different laser position. (b) and (d) are the corresponding C-AFM current mapping. Contact force $F=5$ nN.

3.4 C-AFM measurement on other materials

In comparison, the C-AFM current signal cannot be detected on Ag, p-Si, SiO₂ and traditional TENG polymer samples. The tribo-excited DC occurs spontaneously without any electrical bias or external rectifying circuit, indicating the fundamental difference in the charge transport mechanism.

3.4.1 Ag and SiO₂

We have conducted C-AFM experiments on Ag and SiO₂ sample for comparison. As shown in Fig. 3-6, no current signal has been found on these samples. The electron-hole pairs excited in metal-metal frictional contact has much shorter life time and may just quickly decay into heat. As for insulator SiO₂, charge mobility is very low on the surface and the series resistance is very high that inhibit the DC current flow.

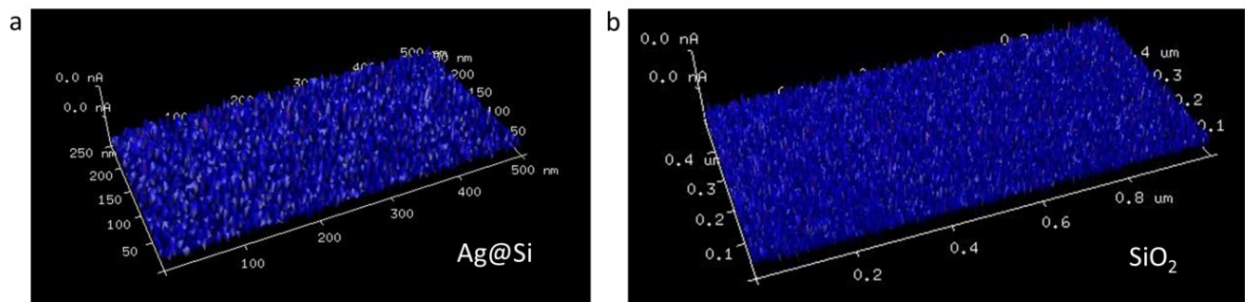


Figure 3-6 C-AFM current measured on (a) Ag sample and (b) SiO₂ sample.

3.4.2 p-type Si

The current signal was not observed mainly because of the naturally grown insulating silica on Si surface, and the localized pressure applied by AFM tip may not be able to penetrate and affect the electronic structure at the SiO₂/Si interface.

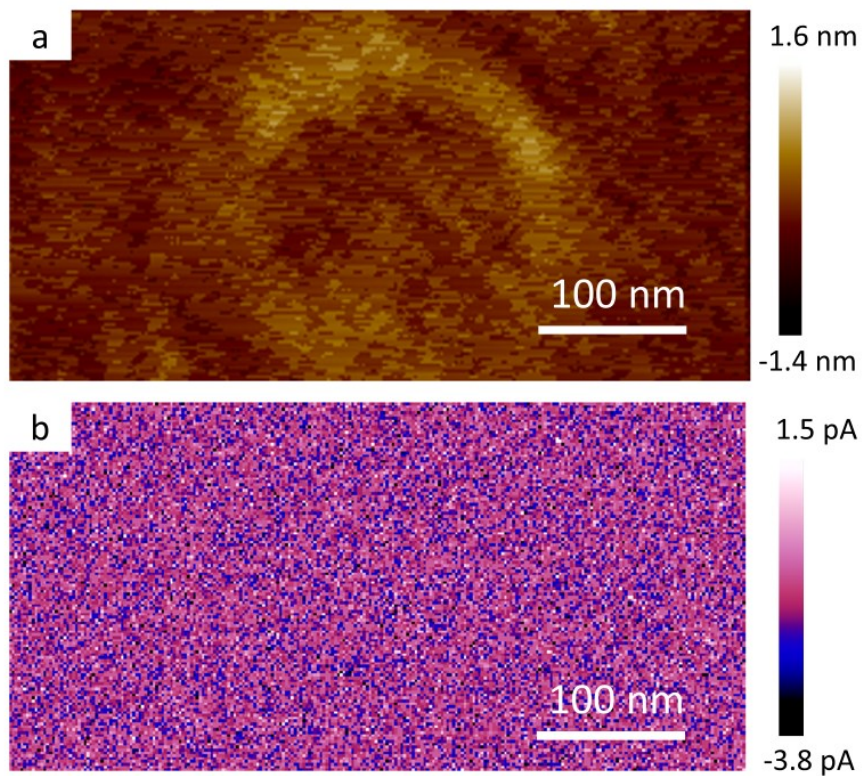


Figure 3-7 C-AFM measurement on p-type Si. (a) Topography and (b) current map.

3.4.3 PEG polymer

For comparison, we have also conducted C-AFM measurement on a spin-coated PEG polymer thin film on Au substrate. As shown in Fig. 3-8, no current signal can be observed. This is mainly because of the poor mobility of tribo-induced charges on the insulating surface.

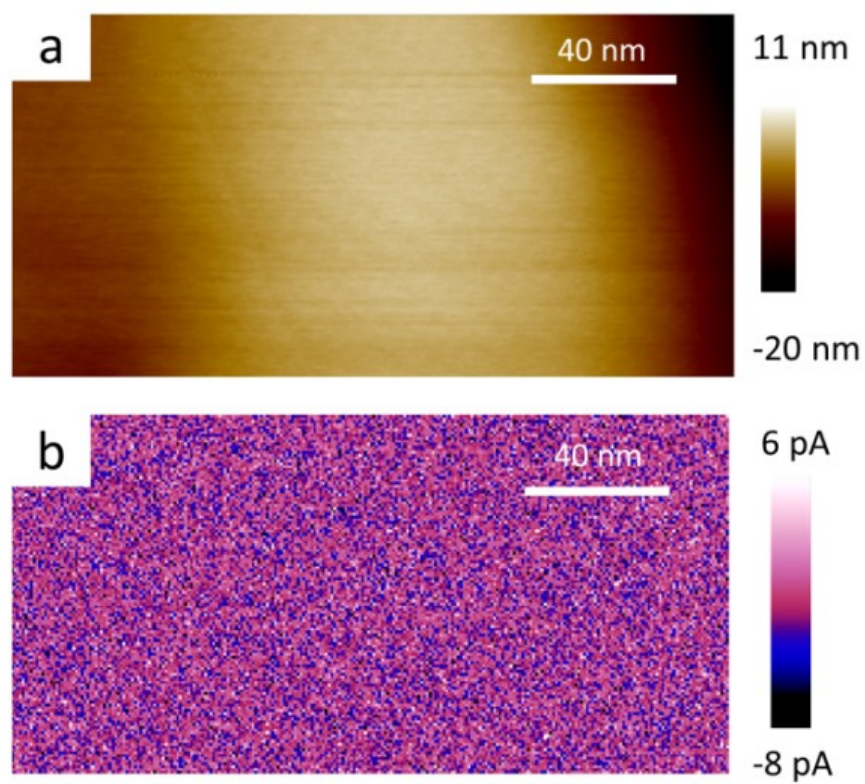


Figure 3-8 C-AFM current measured on spin-coated PEG polymer thin film on Au substrate. (a) Topography and (b) current map.

3.5 In-situ C-AFM I - V characterization

It should be noted that the C-AFM current generation in our system (sliding metal-semiconductor contact) differs from the surface charge accumulation effect observed on the polymer surface by Kelvin Probe Force Microscopy (KPFM).⁶⁷⁻⁶⁹ In the latter case, electrostatic charges are deposited on the polymer surface by the AFM tip via triboelectrification, *i.e.* contact electrification under friction, which have negligible electrical communication with the insulating bulk. In those AFM studies, no displacement current flows in the system as the tip-sample capacitor is neither vibrated in contact-separation mode, nor mismatched in sliding mode ($\partial C/\partial t=0$).¹⁰ In contrast, the carrier flow in our case is more likely due to the direct electronic excitation at the metal-semiconductor interface followed by diffusion-drift conduction throughout the material system. It has been reported that the electronic excitation in friction manifests itself in various physical phenomena such as electron-hole pair generation, triboluminescence, exo-electrons, etc.⁵⁹ Surface states may also play a role here indicating by the cyclic I - V measurement.

The existence of surface S vacancies and other defects facilitate the surface energy states formation, which may store charges as revealed by the observed hysteresis in the cyclic voltammetry measurement (Fig. 3-9). It is found that the hysteresis loop is much more conspicuous in the case of Cu probe in direct contact with the MoS₂ sample compared with that with a thin Pt/Cr top electrode deposited in advance.

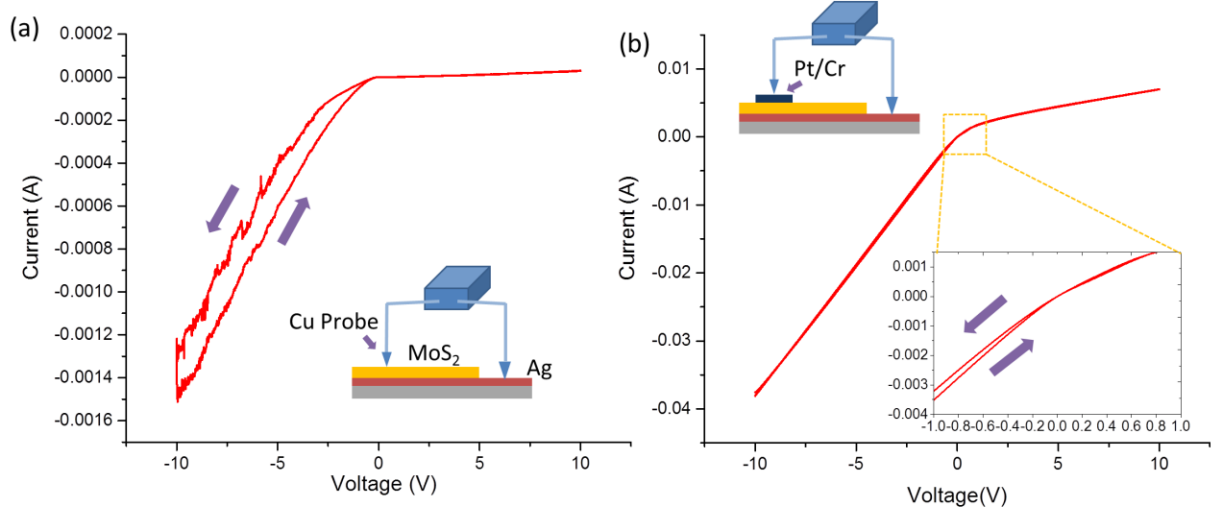


Figure 3-9 Cyclic I - V measurement on the PLD-synthesized MoS₂/Ag sample using probe station. (a) Sample surface in direct contact with Cu probe. (b) Pt/Cr top electrode was deposited in advance and in contact with the Cu probe.

Specifically, it is found that the Schottky contact between the tip and MoS₂ plays a significant role in the tribo-excited charge transport. As a typical example, Fig. 3-10a shows three adjacent MoS₂ crystal grains with different tribo-excited current responses (Fig. 3-10b and (c), $I_{\text{grain 2}} > I_{\text{grain 3}} > I_{\text{grain 1}}$). Multiple I - V data points of grains 1, 2, and 3 and their equivalent circuits are shown in Figs. 3-11, 3-12, 3-13, respectively. From the C-AFM I - V spectra, it is evident that both grains 1 and 2 exhibit diode features but with different rectifying directions. Noting the bias is applied from the sample to the AFM tip, one would expect the tribo-excited electrons transport from MoS₂ to Pt/Ir to be facilitated on grain 2 and suppressed on grain 1. Showing the same diode direction of grain 1 but much more Ohmic nature, grain 3 exhibits a moderate current output. This discrepancy may result from the surface potential fluctuation on different MoS₂ grain surface and the MoS₂-bottom electrode contact as is easily oxidized.

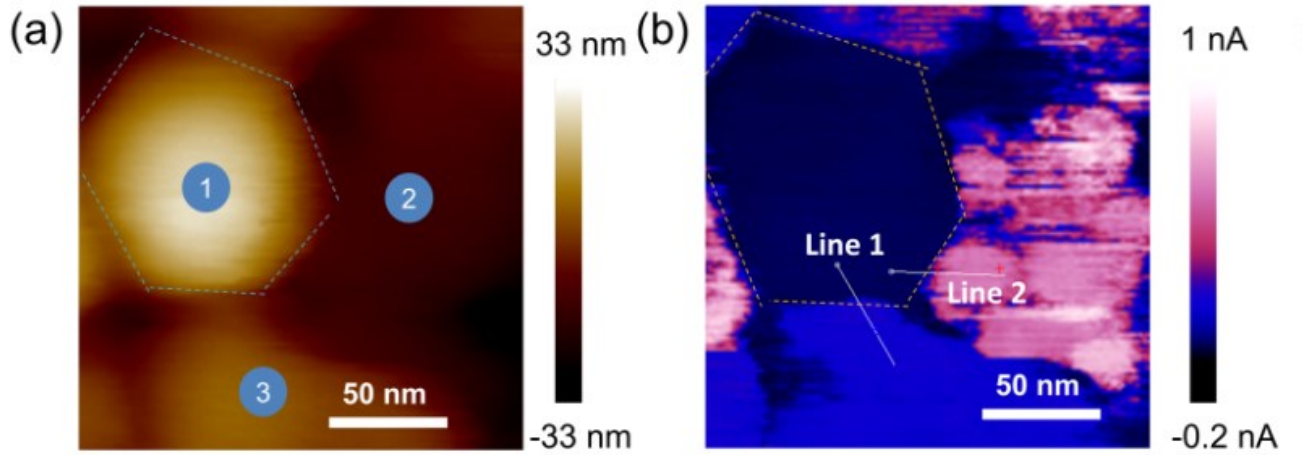


Figure 3-10 (a) AFM topographic image of three adjacent MoS₂ crystal grains marked as 1, 2, and 3. Their corresponding C-AFM current map is shown in (b).

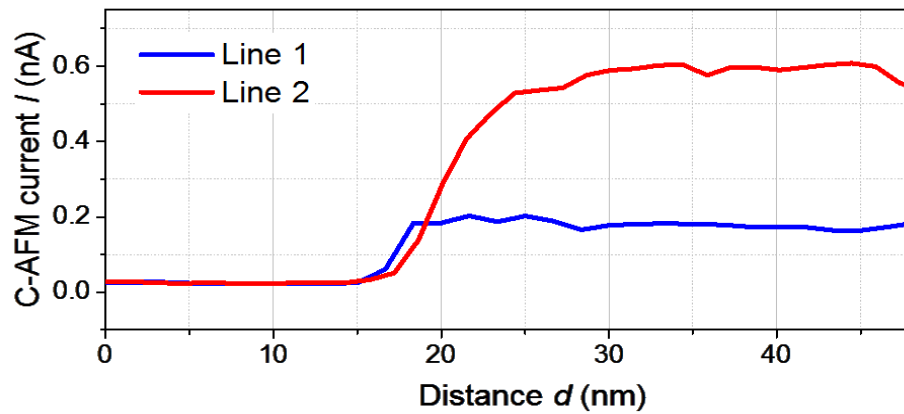


Figure 3-11 Cross-sectional line analysis of the current as marked on 3-10(b)

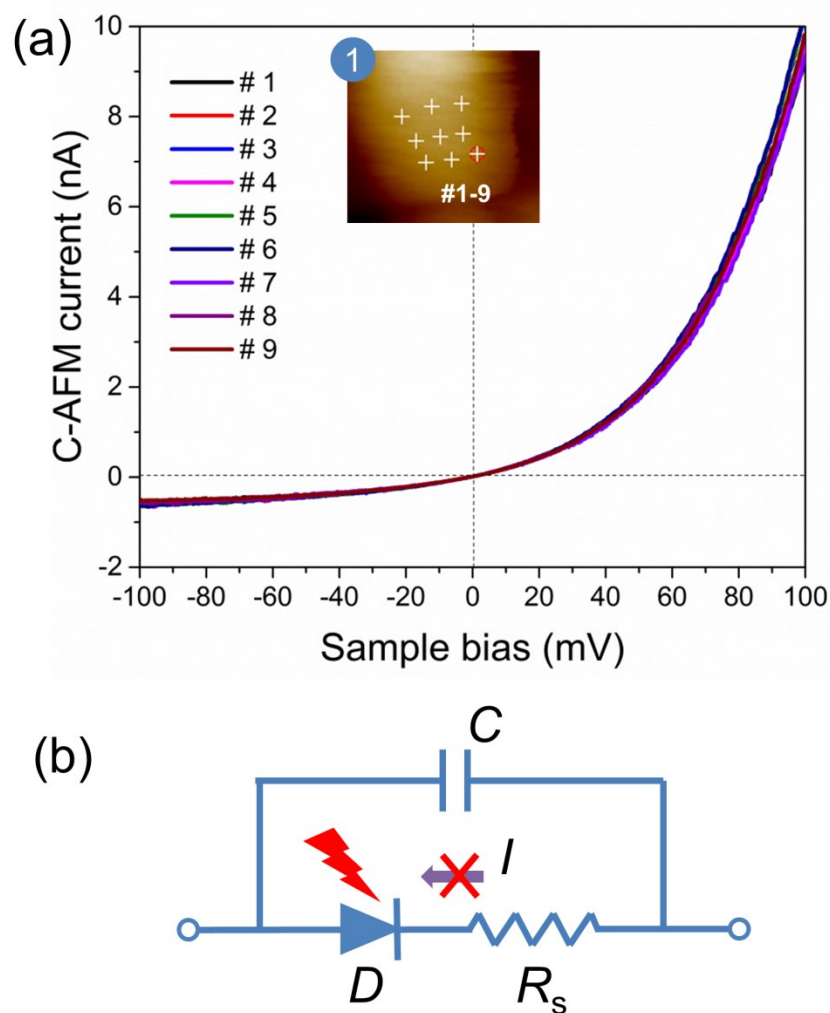


Figure 3-12 C-AFM I - V spectra on grains 1 is depicted in (a). Inset: nine data points marked on the topographic image (collected from left to right, top to bottom). Inset (bottom) in (a) is the magnified I - V spectra of points #1-9. (b) illustrates the equivalent circuits of tip-grain system 1. C , D , and R_s represent the capacitance of semiconductor depletion region, Schottky diode, and series resistance, respectively. The current flow from metal to MoS₂ is suppressed this case.

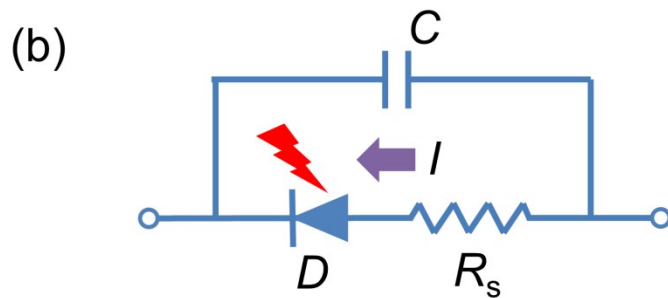
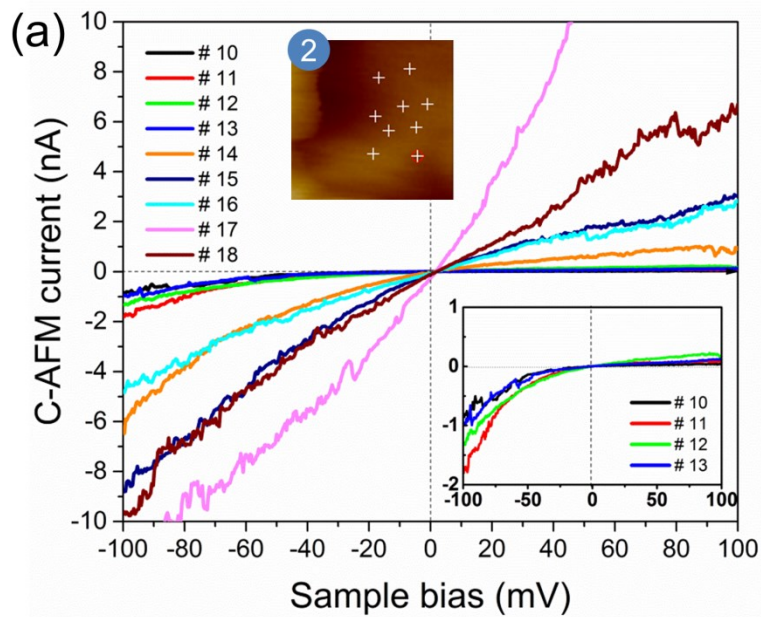


Figure 3-13 C-AFM I - V spectra on grain 2 is depicted in (a). Inset: nine data points marked on the topographic image (collected from left to right, top to bottom). Inset (bottom) in (a) is the magnified I - V spectra of points #10-18. (b) illustrates the equivalent circuits of tip-grain system 1. C , D , and R_s represent the capacitance of semiconductor depletion region, Schottky diode, and series resistance, respectively. The current flow from metal to MoS₂ is facilitated in this case.

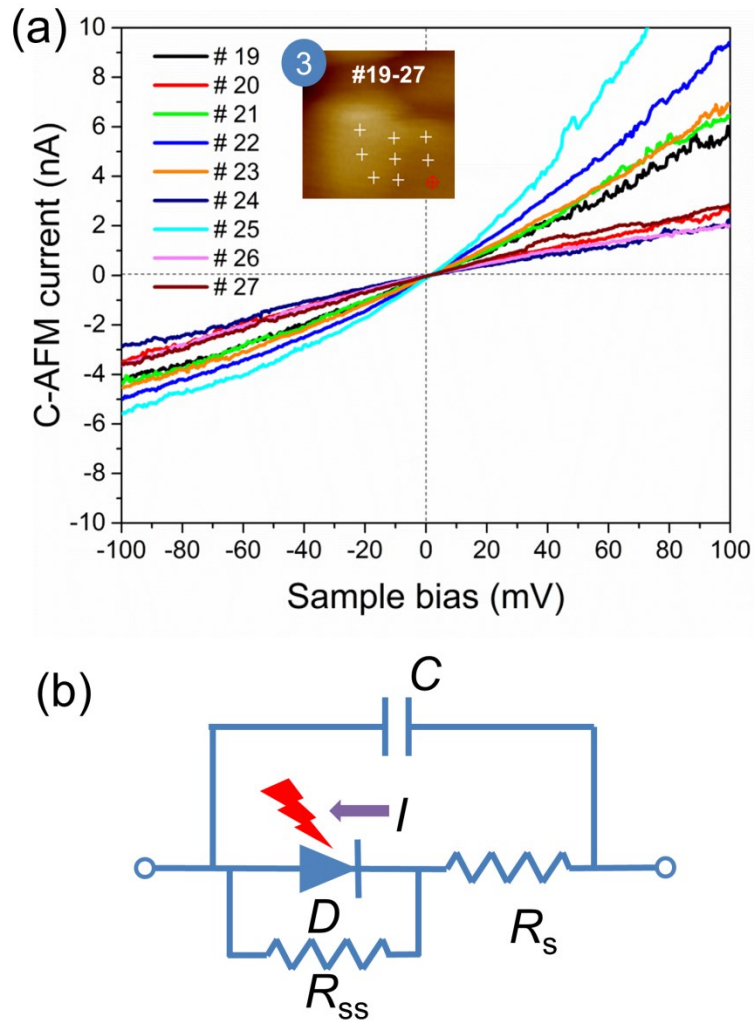


Figure 3-14 C-AFM I - V spectra on grains 3 is depicted in (a). Inset: nine data points marked on the topographic image (collected from left to right, top to bottom). Inset (bottom) in (a) is the magnified I - V spectra of points #19-27. (b) illustrates the equivalent circuits of tip-grain system 1. C , D , and R_s represent the capacitance of semiconductor depletion region, Schottky diode, and series resistance, respectively. In this case, the circuit of tip-grain 3 shows the same diode direction as grain 1 but with a more Ohmic nature. This is expressed by an additional R_{ss} in parallel with D , which exhibits less rectifying properties and thus moderate current output.

Fig. 3-15 shows another example of the *in-situ* I - V characterization. A single MoS₂ grain is scanned (Fig. 3-15a), with its corresponding current distribution shown in Fig. 3-15b. It can be seen that the top-left region of the grain shows less current output compared to that of the bottom-right region. Fig. 3-15c and 3-15d shows the I - V spectrum collected from data point 1-6 and 7-14, respectively. The relationship between the I - V spectrum features and C-AFM current output is in line with the previous example with three individual grains.

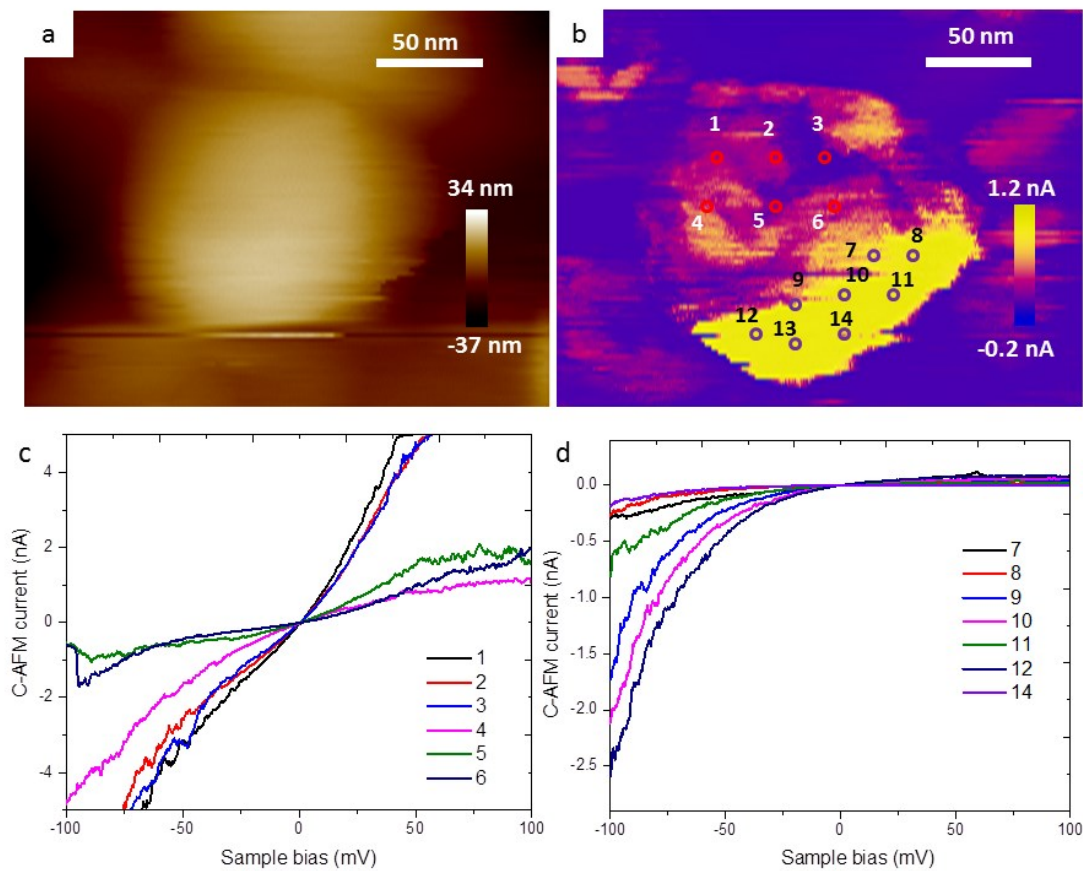


Figure 3-15 (a) AFM topographic image of one MoS₂ grain and its (b) corresponding C-AFM current map. (c) and (d) shows the I - V spectra of the location #1-14 as marked in (b).

3.6 C-AFM I - V data analysis

C-AFM I - V data of the example show in Fig. 3-10 has been analyzed by thermionic emission theory. According to the thermionic emission (TE) model for a Schottky contact, current I as a function of bias voltage V can be expressed by^{100,101}:

$$I = I_0 \exp\left(\frac{eV}{nkT}\right) \left[1 - \exp\left(-\frac{eV}{kT}\right)\right] \approx I_0 \exp\left(\frac{eV}{nkT}\right) \quad (3-1)$$

The saturation current I_0 at reverse bias is given by:

$$I_0 = AA^*T^2 \exp\left(-\frac{\Phi_B}{kT}\right), A^* = 4\pi qm^*k/h^3 \quad (3-2)$$

where A is the metal-semiconductor contact area, A^* is the Richardson constant, q is elementary charge, m^* is effective mass, k is the Boltzmann constant, h is the Plank constant, T is temperature, n is ideality factor and Φ_B is the Schottky barrier height. When n is close to 1, an ideal Schottky contact can be expected. Tunneling conditions may exist depending on the local electric field at the interface. TE model fitting reveals that ideality factor n for data points #14-18 (grain 2) deviates from 1, indicating an imperfect prediction by the TE theory and the existence of electron tunneling at the tip-sample interface (Fig. 3-10)¹⁰⁰ Specifically, the arising of electron tunneling to the overall charge transport characteristics in the C-AFM system has been ascribed to the local electric field effect at nanoscale Schottky contact: the ultrahigh electric field E_{loc} under the AFM tip, as we showed in the finite element method (FEM) simulation, would break the space charge density-limited requirement and trigger charge tunneling transport.^{100,102}

The I - V data fitting with thermionic emission model is shown in Fig.3-16, and the predicted parameters are summarized in Table 3-1. For region 1 and 2, contact is formed in the order of

metal-semiconductor and semiconductor-metal, so that the “forward” direction of Schottky contact, where electron flows from n-type MoS₂ to metal, is opposite in these two cases.

Accordingly, fitting was conducted in the positive and negative sample bias part of data acquired in region 1 and region 2, respectively. For region 2, data point #17 has not been considered for fitting since it exhibits an Ohmic feature. Specifically, imperfect fitting of data points #16 and #18 is in line with the existence of tunneling component in the overall charge transport characteristics as discussed in main text.

For the TE model used in our experiment, metal-semiconductor contact area $A=6 \text{ nm}^2$; elementary charge $q=1.6 \times 10^{-19} \text{ C}$, effective mass $m^*=0.5m_e=4.56 \times 10^{-31} \text{ kg}$, Boltzmann constant $k=1.38 \times 10^{-23} \text{ J/K}$, Plank constant $h=6.6 \times 10^{-34} \text{ m}^2\text{kgs}^{-1}$, temperature $T=298 \text{ K}$.

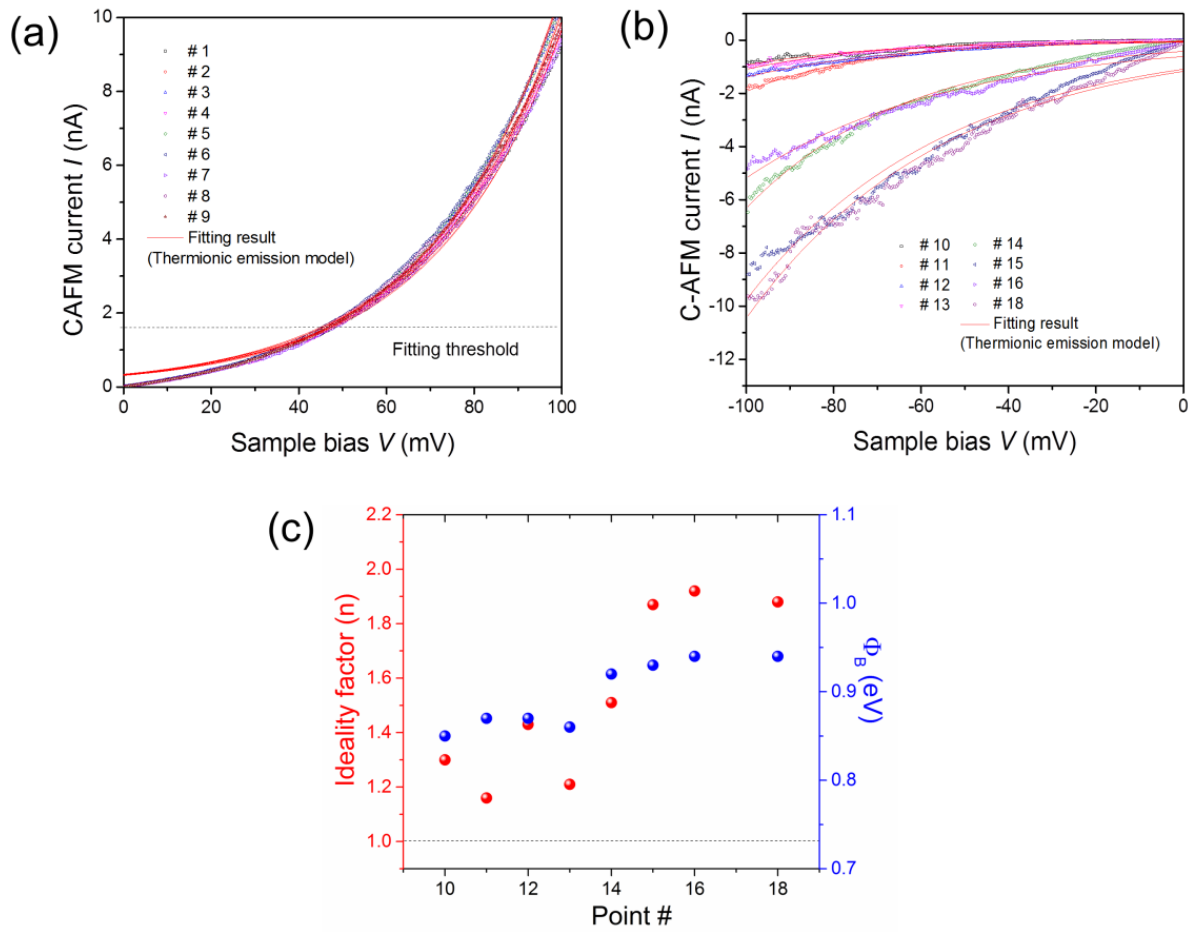


Figure 3-16 (a) Forward I - V spectrum (#1-9) fitted with thermionic emission model (Eq. 3-1). (b) Reverse I - V spectrum (#10-18) fitted with thermionic emission model. (c) Estimated ideality factor n and energy barrier Φ_B from fitting result in (b).

Table 3-1 Summary of fitting results

Region	Data point #	Ideality factor n	Energy barrier Φ_B (eV)
1	1	1.21	0.89
	2	1.18	0.88
	3	1.18	0.89
	4	1.20	0.89
	5	1.18	0.89
	6	1.19	0.89
	7	1.19	0.88
	8	1.21	0.89
	9	1.19	0.89
2	10	1.30	0.83
	11	1.16	0.84
	12	1.43	0.85
	13	1.21	0.83
	14	1.52	0.89
	15	1.87	0.92
	16	1.92	0.90
	18	1.88	0.92

3.7 Voltage output and electric field characteristics

Figures. 3-17a-f show that the current signal can be suppressed with a positive sample bias, nullified when $V=7-8$ mV, and inversed afterwards. In contrast, the current signal is enhanced with a negative bias. Theoretically, this nullified voltage is equivalent to the open circuit voltage V_{oc} of this nanogenerator system, which may be related to the variation of energy distribution of surface charges. By knowing the V_{oc} of our nanogenerator system, we are able to simulate the electric field distribution using FEM. It is well-known that the special electrode geometry in the C-AFM system (nano tip-plane) can induce a strongly intensified local electric field E_{loc} and hence yield ultrahigh current density J .^{102,103} It was found that the AFM tip produced a significant electric field enhancement as expected (Fig. 3-18a) with an even distribution of the potential assumed at the tip-sample interface (Fig. 3-18b). The highest enhancement occurs at the edge of the tip-sample interface with the value of 7×10^5 V/m, penetrating inside the contact interface and remaining in the order of 10^5 V/m.

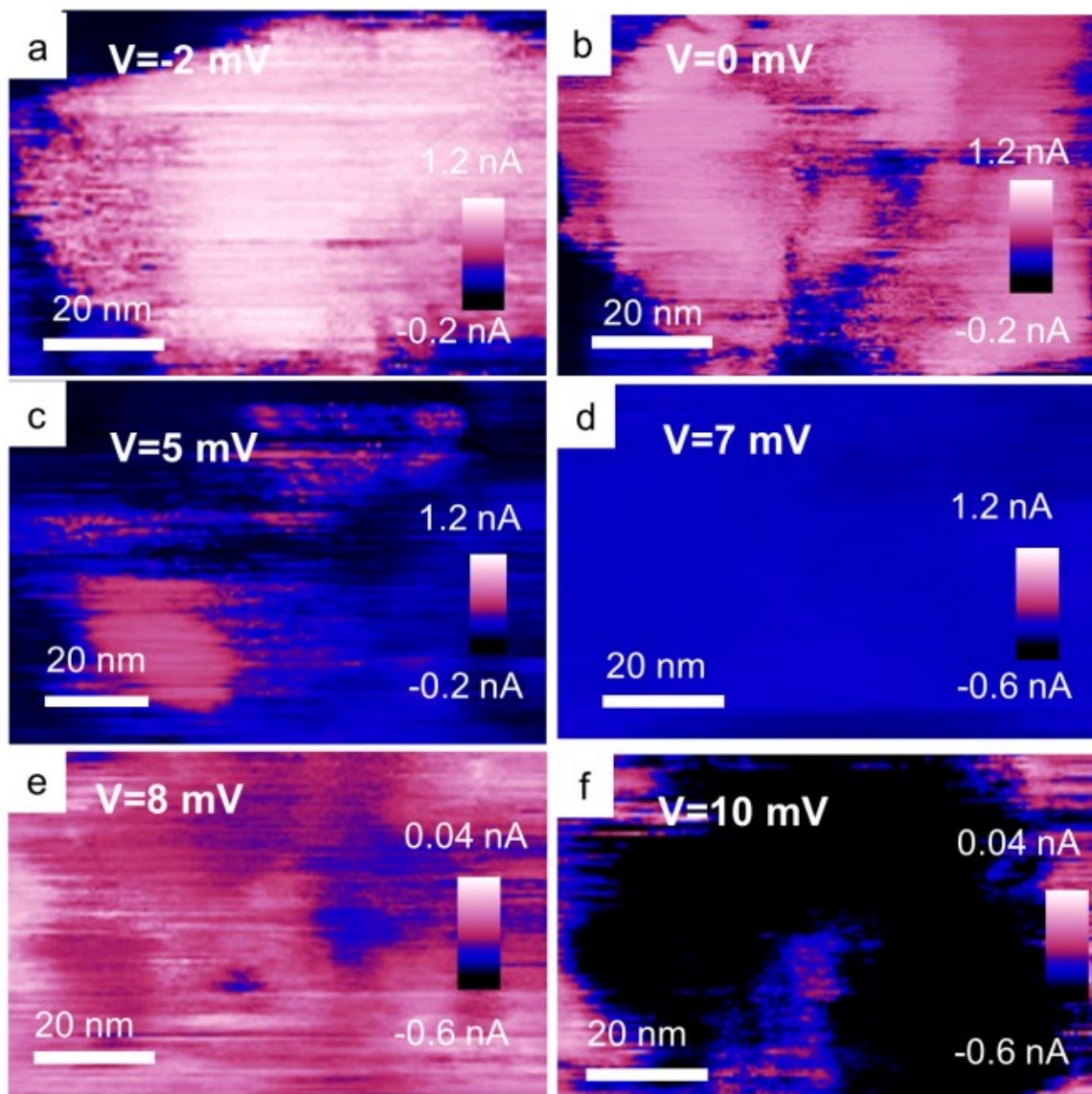


Figure 3-17 C-AFM current map on the single crystal grain in Fig. 1c with the sample bias V of (a) -2 mV, (b) 0 mV, (d) 7 mV, (e) 8 mV, and (f) 10 mV. Tribo-excited current is nullified with the sample bias of 7-8 mV, of which the value is the open circuit voltage of the nanogenerator system.

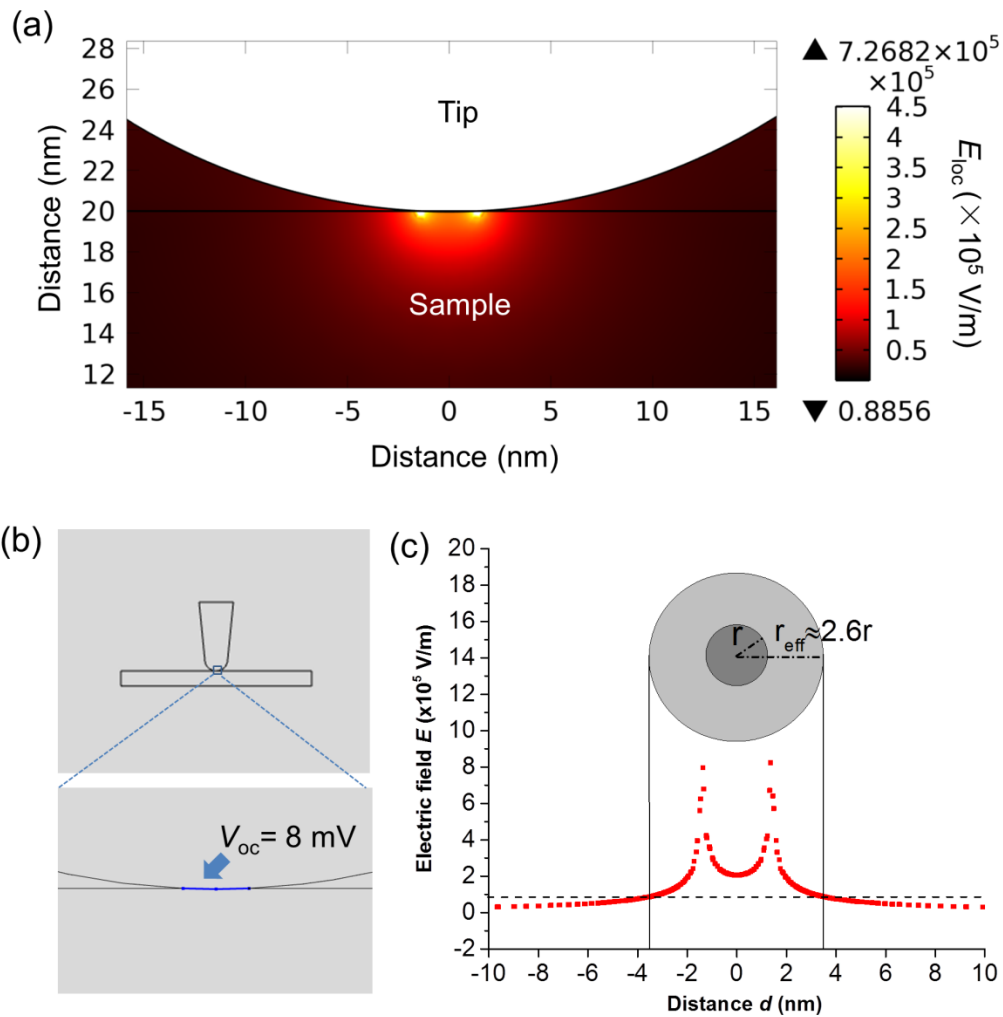


Figure 3-18 (a) Simulated electric field distribution at the tip-sample interface. An intensified local electric field ($E_{loc}=10^5$ - 10^6 V/m) is found. (b) 2D Model for finite element modeling. (c) Line analysis of electric field E vs. distance to tip d at the tip-sample interface simulated by FEM. Here, $d=0$ is defined as the center tip front. It can be seen that E intensifies at tip-sample contact fringe and decays by 10 times at $d \approx 2.6r$, which can be

considered as the radius of effective electrical contact area (r : the radius of actual contact area).

Since the non-uniform electric field generates an effective region from which the excited charges can drift to the AFM tip, an effective electrical contact area should be considered when calculating the current density J . Figure 3-17c shows that E intensifies at the tip-sample contact fringe and decays by 10 times at $d \approx 2.6r$, where r is the radius of actual contact area. The simulated result is in good agreement with the prediction from the numerical method ($d \approx 3r$).¹⁰³ Typically, this distance can be considered as the radius (r_{eff}) of an “effective area” (A_{eff}) for excited carriers to drift from the sample to the top electrode (AFM tip).¹⁰³ Accordingly, the estimation of current density in our case may utilize A_{eff} ($\approx 6.8A$) instead of the actual contact area A for a more accurate prediction, which is in the order of 10^6 A/m² depending on the criterion of selecting threshold E for charge transport.

3.8 The proposed charge transfer mechanism

As is shown in Fig. 3-19, the electrons with sufficient energy may be excited from the surface states or valence band into the conduction band, overcome the energy barrier from semiconductor side (qV_{bi}) and transmit into the metal side. This scenario is very likely to happen since the band gap of layered-MoS₂ is very narrow (1.2-1.4 eV)⁹³ while the direct electronic excitation from friction can result in highly energetic electron-hole pairs. For the excited electrons with lower energy, they may, if not recombined with the holes, fall into the unoccupied surface states and transmit into the metal side assisted by the intensive electric field and

frictional heat. The possible excitations from the metal side, in contrast, would be expected to decay much faster into lattice vibration considering the short lifetime of electron-hole pairs in metal and the higher energy barrier (Φ_B) the excited electrons would meet from the metal side. As a result, a rectification of charge flow can be achieved. It is noteworthy that the surface energy states would inevitably exist in the metal-MoS₂ Schottky contact, due to the surface defects as well as the unusual interface dipole formation¹⁰⁴ (the formation of gap energy states with Mo *d*-orbital characters).

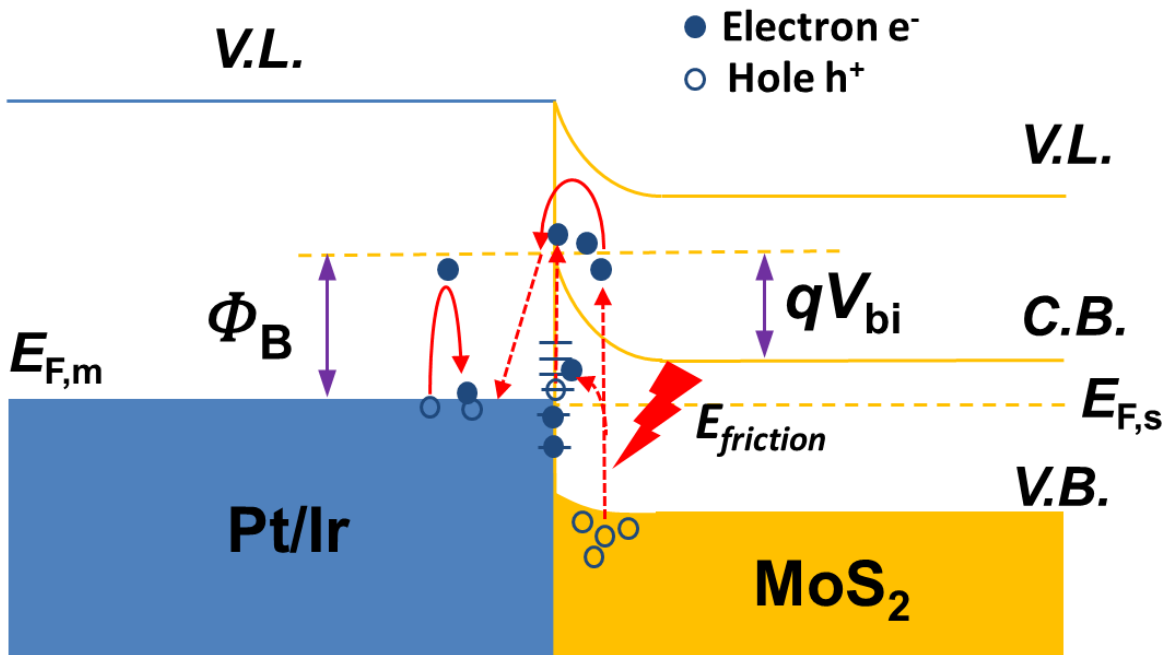


Figure 3-19 Energy band diagram of the tip-sample interfaces and the proposed charge transfer mechanism: Schottky contact is formed between the Pt/Ir coated AFM tip and MoS₂. While the electrons from surface states/valence band may be excited by frictional energy and transmit into the metal side, the excited electron-hole pairs from the metal side have shorter life time and encounter higher energy barrier.

3.9 Contact force-dependent C-AFM current output

Furthermore, we investigated the effect of contact force on the C-AFM current output. Here, we have used the Derjaguin-Muller-Toporov (DMT) model for estimating F dependent- A of the tip-MoS₂ contact. In an AFM system, hard and poorly adhesive materials are best approximated by the DMT model.⁵⁹ According to the DMT model, A is given by⁵⁹:

$$A = \pi \left[\frac{R}{K} (L + 2\pi R\gamma) \right]^{2/3} \quad (3-3)$$

where R is AFM tip radius, L is the load (contact force F), and γ is the work of adhesion. The term $2\pi R\gamma$ can be considered as an ‘additional load’ L_{ad} , which is determined by the “pull-off” force in the force curve (see Fig. 3-20c). K is the reduced Young’s modulus given as $K = \frac{3}{4} \left(\frac{1-\nu_s^2}{E_s} + \frac{1-\nu_t^2}{E_t} \right)$, where E_t and E_s are Young’s moduli and ν_t and ν_s are the Poisson ratios of the tip and the sample, respectively. Adhesion measurement was conducted with PeakForce QNM mode (Bruker, USA). The average adhesive force can be used for tip-sample contact area estimation.

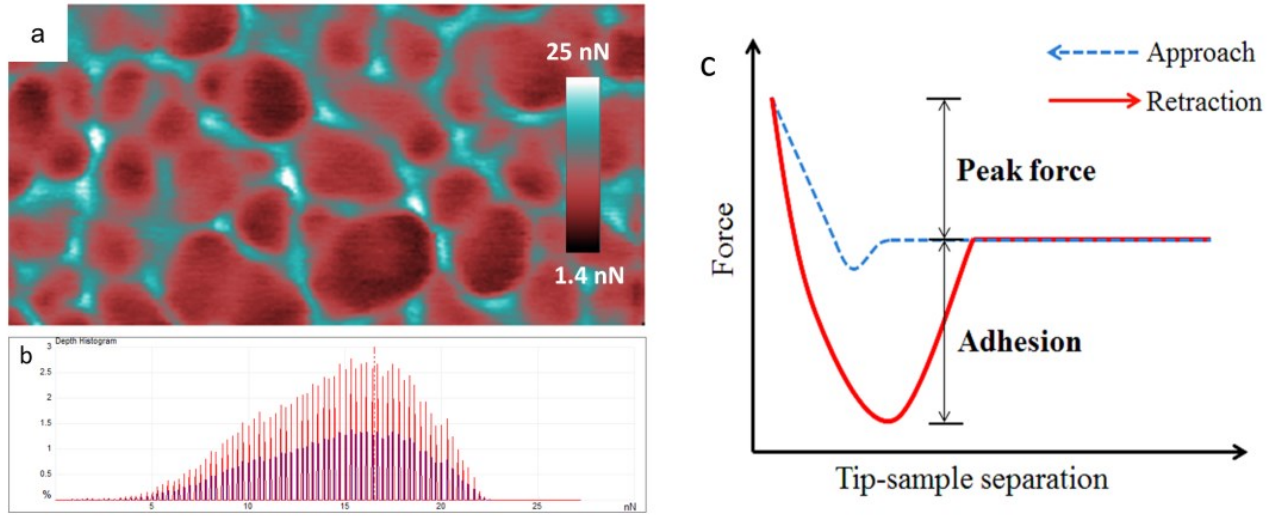


Figure 3-20 (a) Tip-sample adhesion mapping of MoS₂. (b) Histogram of the adhesion distribution. (c) Typical force curve in PeakForce QNM measurement.

As shown in Figs. 3-21a and 3-21b, by increasing the applied force during the scan, there is an enhanced DC response throughout the entire surface. Analytically, it can be seen from Fig. 3-21c that average current I_{ave} increases from ~ 0.08 nA to 0.15 nA when the applied force is increased from 5 nN to 30 nN, while the peak current I_{peak} remains relatively less sensitive to F with the value around 1.1 nA. The enhanced current distribution and the increasing I_{ave} may be understood, since the tip-sample contact area is enlarged with a higher force applied. By normalizing I with estimated A , current density can be calculated as shown in Fig. 3-21d. While the J_{ave} of MoS₂ remains relatively stable, the J_{peak} exhibits a decreasing trend with increasing F , indicating the J_{peak} is optimum when the single asperity for electrification has small but sharp feature. This can be understood by considering that a larger surface curvature results in an ultrahigh electric field as shown in the simulated result, which gives rise to the largest current density value.

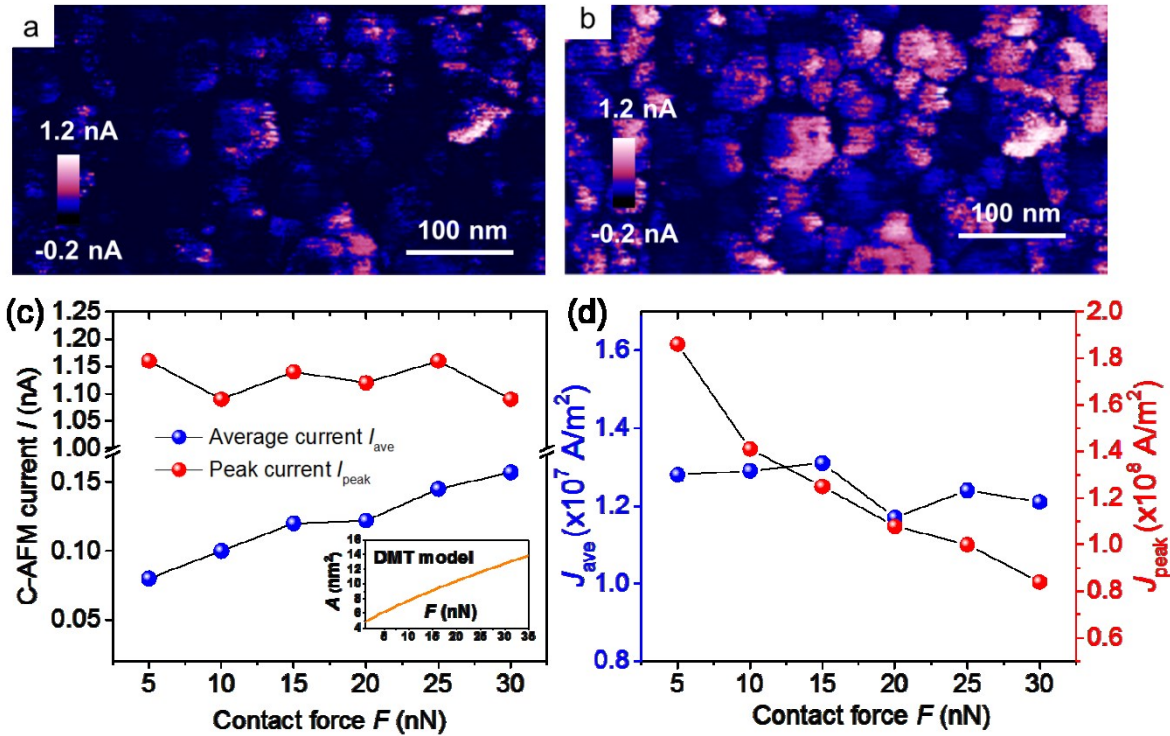


Figure 3-21 C-AFM current mapping of MoS₂ with contact force of (a) 5 nN and (b) 30 nN. (c) is the F -dependent average current I_{ave} and peak current I_{peak} of MoS₂. Inset: estimated F -dependent tip-sample contact area A from the DMT model (Eq. 3-3). (d) shows the F -dependent average current density J_{ave} and peak current density J_{peak} of MoS₂. Note that the value of J in (d) is obtained by normalizing the current with actual contact area. By considering the effective electrical contact area in the point-plane system, all values of J would be one order lower.

The C-AFM current signal has also been observed in the force curve characterization (Fig. 3-22). Typical approach (black) and retract (red) curves are shown in Fig. 3-22. Different stages are depicted in Fig. 3-22 (a): when the AFM tip approaches the sample, it would snap onto the sample surface due to van der Waals forces.¹⁰⁵ Thereafter, the tip presses on the sample leading

to cantilever deflection (elastic deformation). Accordingly, normal force applied on the sample surface can be calculated by the product of cantilever deflection error and spring constant k . When retracted again, the tip would stick to the sample surface due to adhesion forces before finally snapping free. The hysteresis between the approach and retract curves is called contact hysteresis caused by friction effects between the tip and the sample.¹⁰⁶ As revealed by the C-AFM current signal in the time domain, charge flow occurs immediately after the tip engagement, enhanced with increasing force and eventually tends to saturate. It should be noted that the current signal (in the order of 10 pA) detected in force curve measurements is much less than that observed during scanning (in the order of 1 nA) under the same applied force (in the order of 10 nN). Interestingly, two different stages of current signal with response to normal force can be found (Fig. 3-22 (b) and (d)), which may be related to the existence of less conductive surface depletion regions.

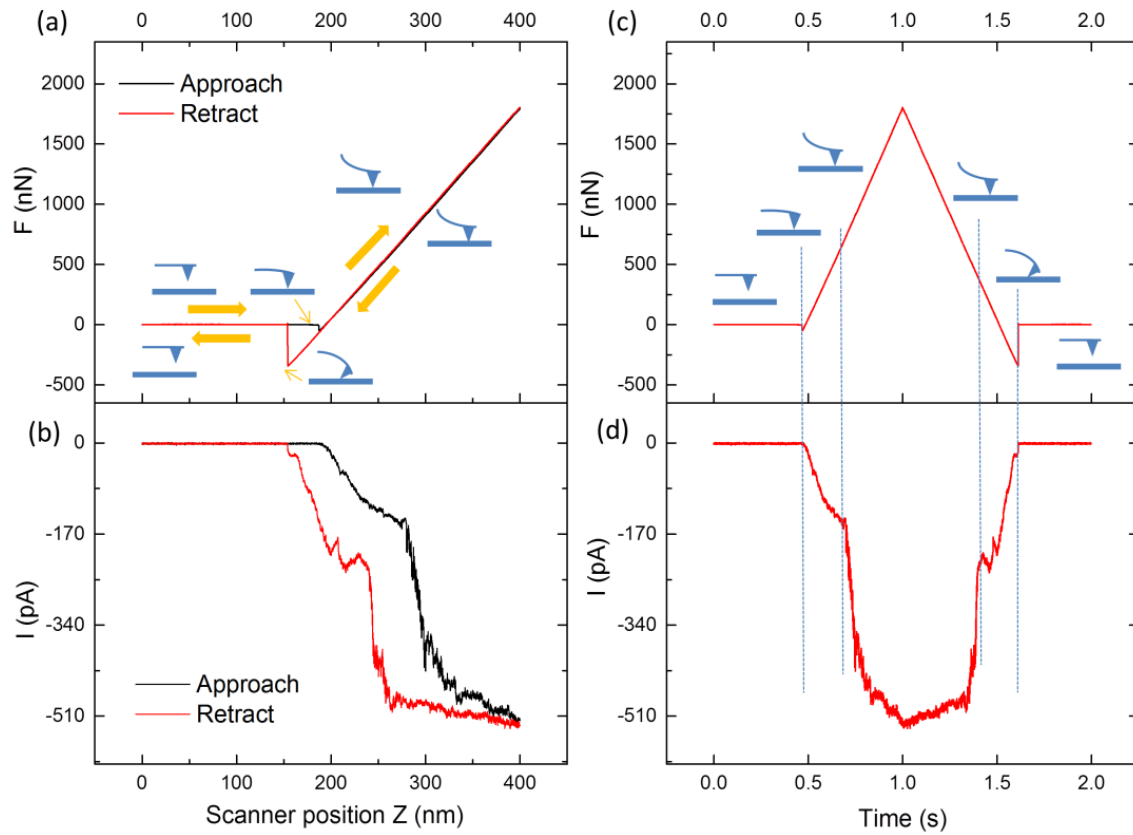


Figure 3-22 (a) and (b) are AFM cantilever force F vs. Piezo-scanner position Z and C-AFM current I vs. Z , respectively. (c) and (d) are their corresponding graphs in time domain.

Although the power output in the single AFM probe system is on the order of pW, the maximum surface and volume power densities are estimated to be in the order of 1 kW/m^2 and 1 MW/m^3 (device thickness $\sim 1 \text{ mm}$), respectively, indicating that the scaling up of the concept is theoretically feasible and promising.²¹ It's worth mentioning that the open-circuit voltage V_{oc} generated with the technique (in the order of mV) is relatively low compared to that obtained with the conventional TENGs, which can be improved in an engineering way such as using a tip

array connected in series. In order to apply the idea to the scaling-up energy harvesting, we would need to reveal the source of this potential gradient, screen the material candidates as well as modify the electrode in the future work.

3.10 Scan number- and velocity-dependent C-AFM current output

The scan number- and velocity-dependent measurements show that the current output is repeatable and not very sensitive to the tip velocity within the tested range (Figs. 3-23 and 3-24).

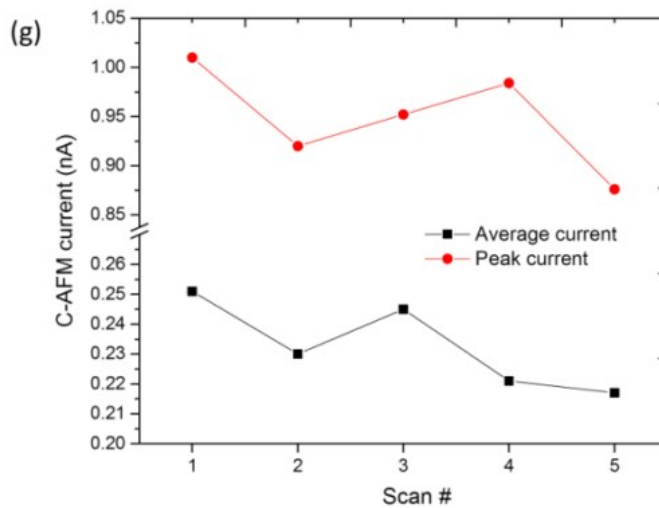
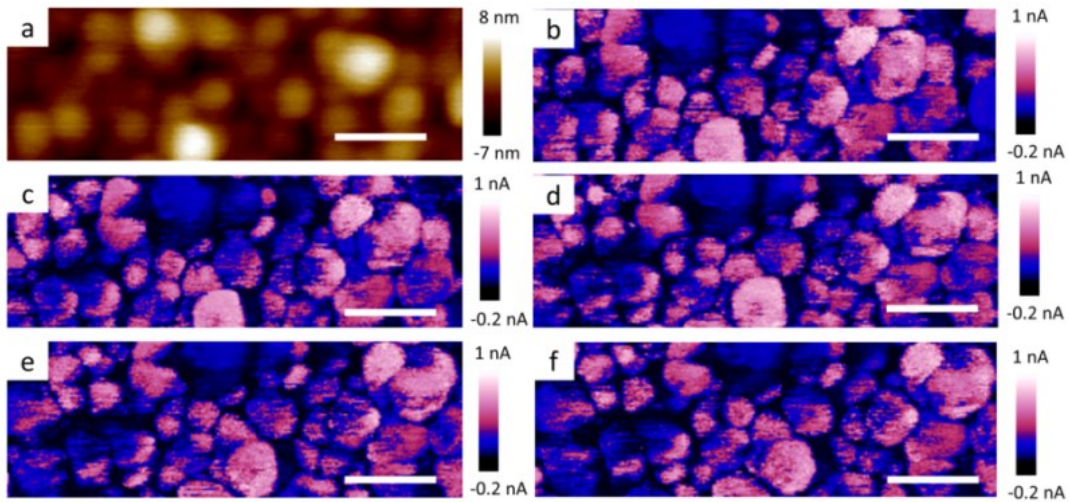


Figure 3-23 (a) Topography of MoS₂ sample and (b-f) its corresponding current output for multiple scans (#1-5). (The scanned area has little drift during the multiple scanning). (g) Average and peak C-AFM current as a function of scan #.

Fig. 3-24 shows the velocity-dependent experimental data. The velocity range is limited by the piezoelectric actuator in the AFM probe holder. For the investigated range, it is found that the C-AFM current has a slightly decreasing tendency with increasing velocity. This can be a result of current diminishing with multiple scans, or the tip-sample electrical contact cannot be built up properly within shorter contact time.

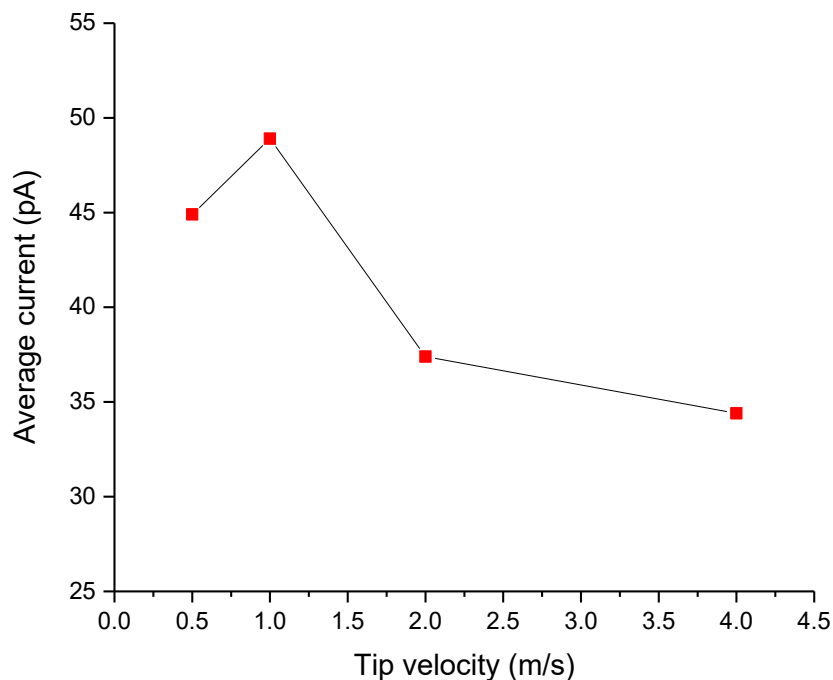


Figure 3-24 Velocity-dependent C-AFM current data. $F=5$ nN.

3.11 C-AFM measurement on the exfoliated MoS₂ sample

In comparison, we have also conducted C-AFM measurement on the exfoliated MoS₂ single crystal layers. As is shown in Fig. 3-25, C-AFM current can be observed on three different MoS₂ layers. The thickness of the very bottom layer is close to that of single layer as revealed by edge topographic scan (Fig. 3-25g and 3-25h). It is found that the DC current signal increases with increasing layer thickness, which cannot be explained by conventional TENG theory (AC output) or piezoelectric signal (only occurs and decreases in the order of 1st, 3rd and 5th layer).¹⁰⁷ The current output is much lower than that observed in PLD-deposited MoS₂ samples, indicating possible influence from bottom electrode contact or surface states. In fact, even the ideal metal-MoS₂ contact has very unusual mechanism of the partial Fermi level pinning caused by interface dipole formation (the formation of gap energy states with Mo *d*-orbital characters).¹⁰⁴

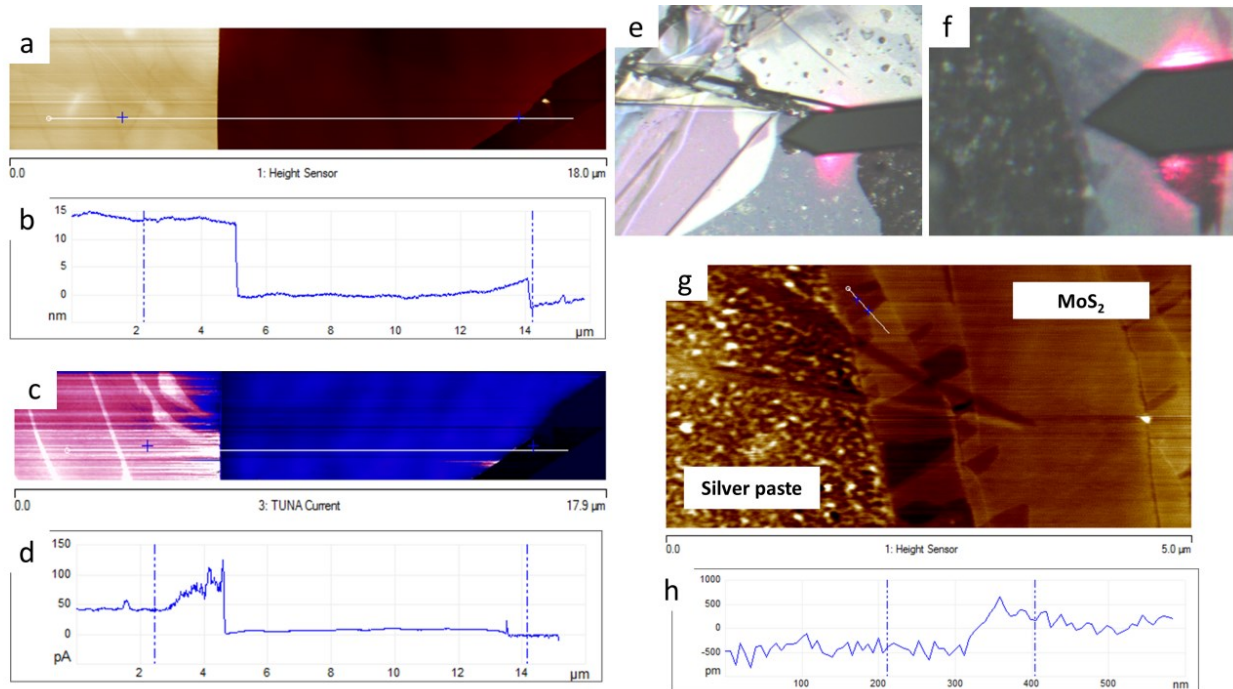


Figure 3-25 (a) AFM topographic image of exfoliated MoS₂ layers and (c) corresponding C-AFM current map. (b) and (d) show line analysis labeled in (a) and (c), respectively. (e) and (f) are optical microscope images of the scan area of (a) and (g), respectively. (g) AFM topographic image of the silver paste-MoS₂ boundary. From line analysis in (h), atomic layer thickness can be seen.

3.12 Conclusion

To summarize, we have demonstrated the direct harvesting of a large triboelectric DC using a nanoscale sliding friction of a C-AFM tip on a pulsed laser deposited MoS₂ thin film, which operates under a fundamentally different mechanism as compared to conventional. Specifically, nano-sized tip-enhanced ultrahigh electric field boosts the local triboelectric current density of this nanogenerator system. It is found that a tip-sample Schottky contact and sample-substrate

Ohmic contact play a significant role in the efficiency of the triboelectricity collection. We believe this new concept offers a promising technique for self-powered portable electronics and large-scale mechanical energy harvesting by integrating DC output from large numbers of single asperities with sharp features. This may either be achieved by a parallelized array of microfabricated tips¹⁰⁸ or hemispherical metal nanoparticle-decorated electrodes³².

Chapter 4 Sustained electron tunneling at unbiased metal-insulator-semiconductor triboelectric contacts

Jun Liu, Mengmeng Miao, Keren Jiang, Faheem Khan, Ankur Goswami, Ryan McGee, Zhi Li, Lan Nguyen, Zhiyu Hu, Jungchul Lee, Ken Cadien and Thomas Thundat, “Sustained electron tunneling at unbiased metal-insulator-semiconductor triboelectric contacts”, 2018, *Nano Energy* 48 (2018) 320–326

(Reprinted with permission from Elsevier Publishing Group)

4.1 Introduction

Mechanical energy harvesting materials and systems have emerged as a promising research area because of the widespread and growing demand for powering wireless sensor networks, wearable devices, and rechargeable energy storage systems.^{3,10,23,40,109} Recent years have witnessed a rapid growth in the development of technologies based on triboelectric nanogenerator (TENG) with which various environmental mechanical energy sources (e.g. wind, water flow, vibration, human body motion, etc.) could be harvested for electric power generation.^{10,40,110,111} Conventionally, TENGs operational principle is based on a phenomenon called ‘contact electrification’ (‘triboelectrification’ if it is under friction): two materials become electrically charged when in dynamic contact.⁵⁸ If one of the materials is a good insulator such as polymers, the charges persist on the surface leading to the building up of very high voltages. For energy harvesting purpose, distance or contact area between the materials is modulated so as to generate a displacement current.¹⁰ As a result, an a.c. dielectric displacement current output that manifests itself as transient peaks as a function of time is obtained.¹⁰ Though a polymer-based TENG is capable of generating high voltages, its current generation capability is limited because of its large impedance.^{10,110}

Recently, it was found that a sliding conductive-AFM probe on MoS₂ multilayers can generate triboelectric d.c. output with high current density.¹¹² Direct current generation with similar characteristics has also been reported from vibrating metal-semiconducting polymer systems.^{29,113} These new findings indicate that new physical mechanisms of carrier transport may exist, with which triboelectric charges, induced by friction, may be directly scavenged for

generating d.c. power. Since the obtained current has very high density and does not require any rectification, it is an intriguing strategy for utilizing frictional energy. However, the underlying mechanism still remains unclear, primarily due to the complicated triboelectrification process and the dynamically varying electronic interface.

Herein, we report on tunneling current-based triboelectricity generation in a sliding metal-insulator-semiconductor (MIS) sliding contact, consisting of a metal point contact on a p-type silicon with a thin native silicon oxide (less than 2 nm thick). The triboelectric charging of the interface provides the sustained potential difference for the electron tunneling. The measured current shows an exponential decay with the thickness of the oxide layer deposited with atomic layer deposition (ALD), consistent with electron tunneling through the insulator layer. The demonstration of the high current generation with Si using sliding micro-contacts paves the way for scaling up the nanoscale effects for practical applications. Particularly, the naturally grown thin oxide (< 2 nm) presented on silicon surface provides a perfect tunneling barrier. The low cost and easy availability of silicon make this concept as a promising technique for large-scale mechanical energy harvesting.

4.2 Current output characteristics of the MIS triboelectric contact

4.2.1 C-AFM current mapping

To demonstrate the phenomenon at nanoscale, we have used a Pt/Ir-coated AFM probe (AppNano, Inc.) sliding on a p-Si substrate (boron doped, orientation: <100>, resistivity: 0.1-1 $\Omega \cdot \text{cm}$) with an aluminum back contact without any external bias voltage (Fig. 4-1). Tunneling

current during the sliding was collected using a conducting mode AFM (C-AFM). Fig. 4-2 shows the current distribution vs. applied force (F).

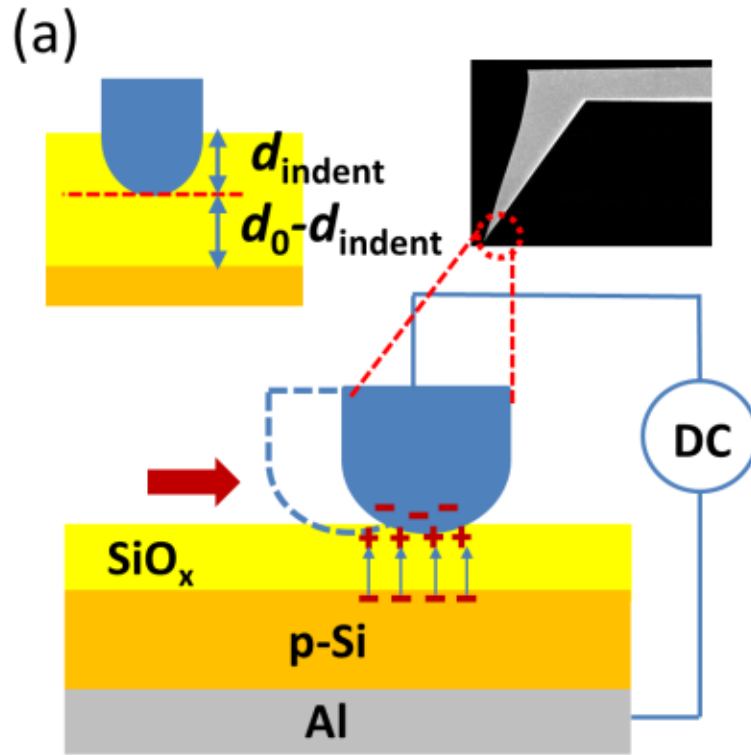


Figure 4-1 Schematic of C-AFM characterization of triboelectric current generation. Sliding a Pt/Ir-coated AFM probe on a p-type silicon sample with an ohmic Al back contact. A native oxide (SiO_x) with thickness d_0 ($d_0 < 2$ nm) presents on the Si surface forms the tunneling barrier. Inset (up-left): probe-sample interface when sufficient force is applied to the probe; an indentation with distance d_{indent} is expected. Inset (up-right): scanning electron microscopy image of the AFM tip.

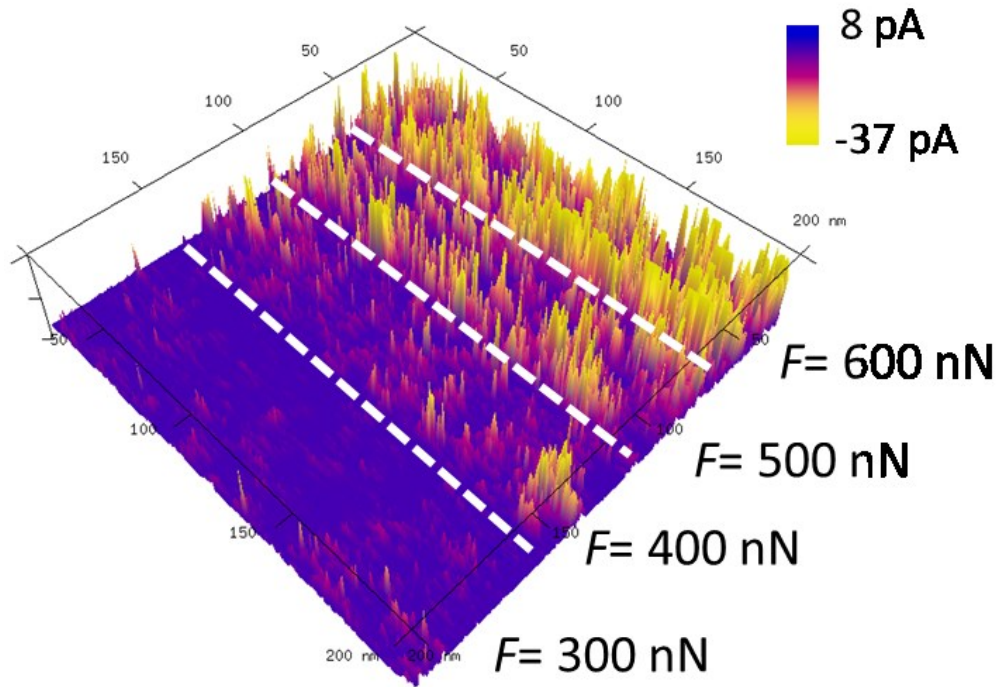


Figure 4-2 Force-dependent current signal. $V_{\text{bias}}=0$ V. Since the bias routing is from the AFM sample stage to the tip, the negative direction of the C-AFM current is from the tip to the sample.

It can be seen from Fig. 4-1 that the current becomes measurable when $F > 300$ nN. It is known that silicon surface is generally covered with a very thin layer of native oxide (SiO_x , 1-2 nm).^{114,115} During the probe-surface contact, a high pressure on the order of 0.1-1 GPa develops under the AFM probe. The actual probe- SiO_x/Si gap distance (d_0-d_{indent}) and the contact area (A) can be approximated by the Derjaguin-Muller-Toporov (DMT) model as shown in Fig. 4-3a (see Methods for more details).^{59,105} Accordingly, current density (J) can be estimated to be of the order of 10^4 A/m².

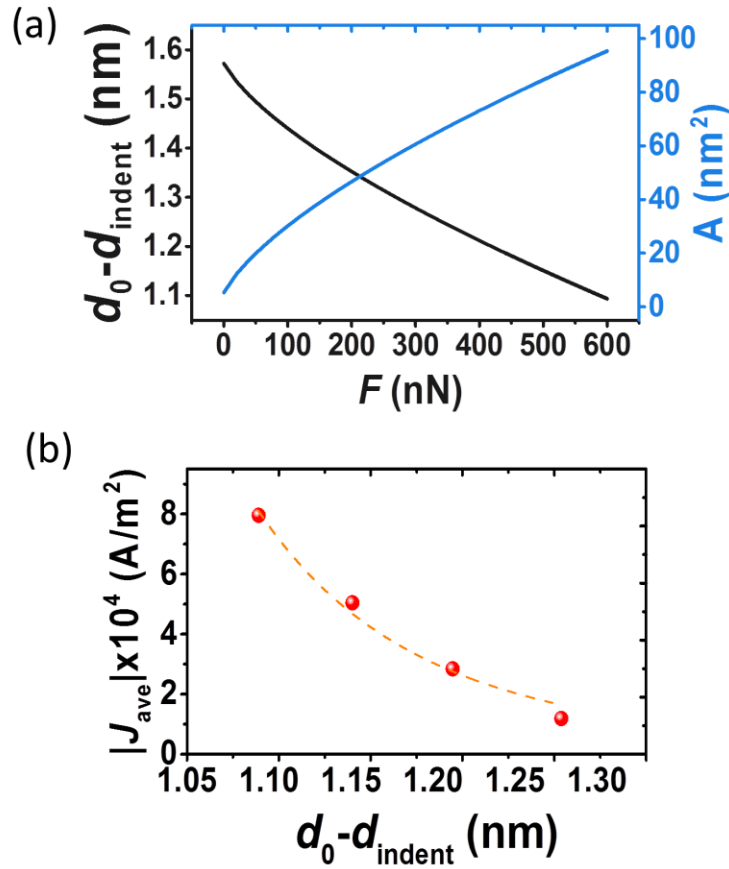


Figure 4-3 (a) The distance of probe-Si/SiO_x interface $d_0 - d_{\text{indent}}$ and contact area A as a function of applied force F (modeled by DMT theory, see Methods for details). (b) Average C-AFM current density J_{ave} as a function of $d_0 - d_{\text{indent}}$. The dashed line is the exponential decay fitting result.

This anomalously high current density may be due to the ultra-high electric field induced by the nano-sized AFM probe.^{102,103,112} Experimentally, J is found to decay exponentially as a function of $d_0 - d_{\text{indent}}$ (Fig. 4-3b), consistent with distance dependence of electron tunneling current (the exponential relationship will be justified below, with more macroscale data points.).

4.2.2 Macroscale current generation

To demonstrate the concept at macroscale, a stainless steel based test lead is manually driven on a p-type silicon wafer (boron doped, orientation: $\langle 100 \rangle$, resistivity: 0.1-1 $\Omega\text{-cm}$), coated with a bottom aluminum ohmic contact (Fig. 4-4a). When the probe was driven in a linearly reciprocating (Fig. 4-4b) and circularly rotating fashion (Fig. 4-4c), corresponding short-circuit currents (I_{sc}) were measured. Figs. 4-5a and 4-5b show I_{sc} for the linearly reciprocating mode circularly rotating mode, respectively. In contrast to the transient a.c. generated by polymer-based TENGs, the current output in our case is observed to be continuous d.c. throughout the frictional contact process, indicating a different current generation mechanism. The I_{sc} output is found to be 3-5 μA . Considering an A of $\sim 1 \text{ mm}^2$ for the macroscale probe, J as high as 3-5 A/m^2 can be estimated, which is significantly higher than those reported in polymer-based TENGs (in the order of 0.1 A/m^2)^{10,32,110} and piezoelectric generators (in the order of 0.01 A/m^2)^{23,116}. This observation is in agreement with our previous conductive-AFM results where a continuous current has been observed when the platinum-coated tip slides on the MoS_2 single grain.¹¹²

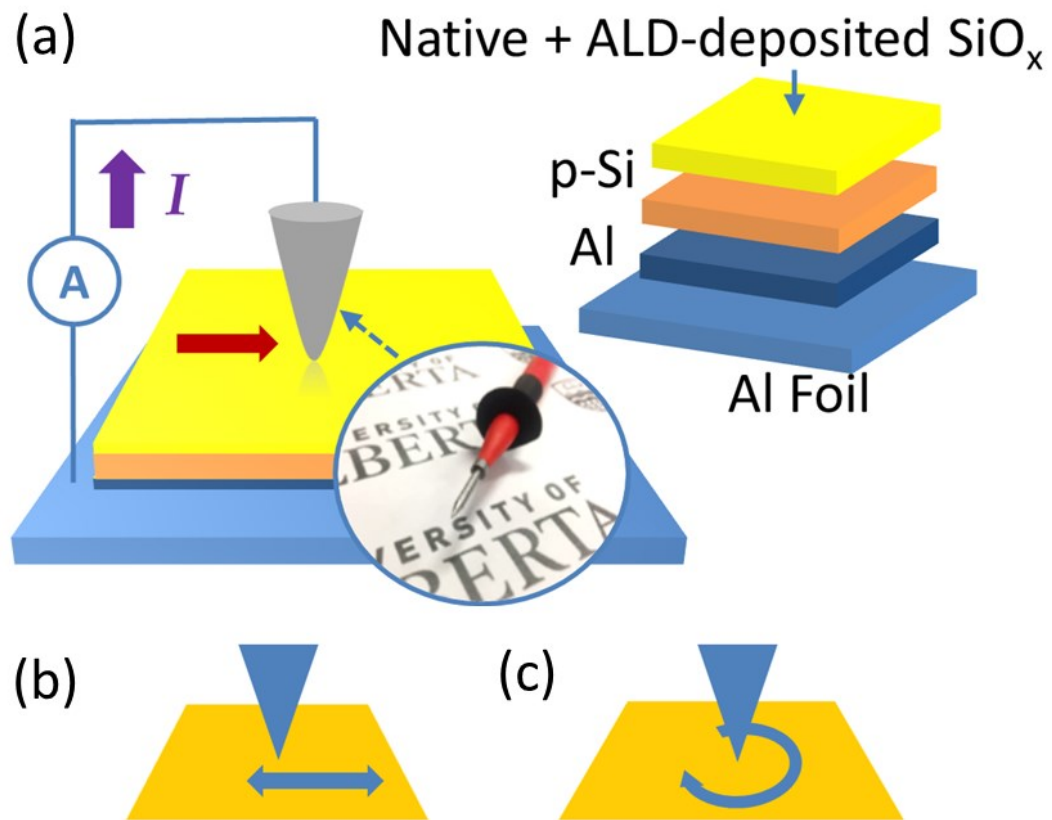


Figure 4-4 (a) Schematic of the macroscale MIS frictional contact system. (b) and (c) shows the linearly reciprocating and circularly rotating modes, respectively.

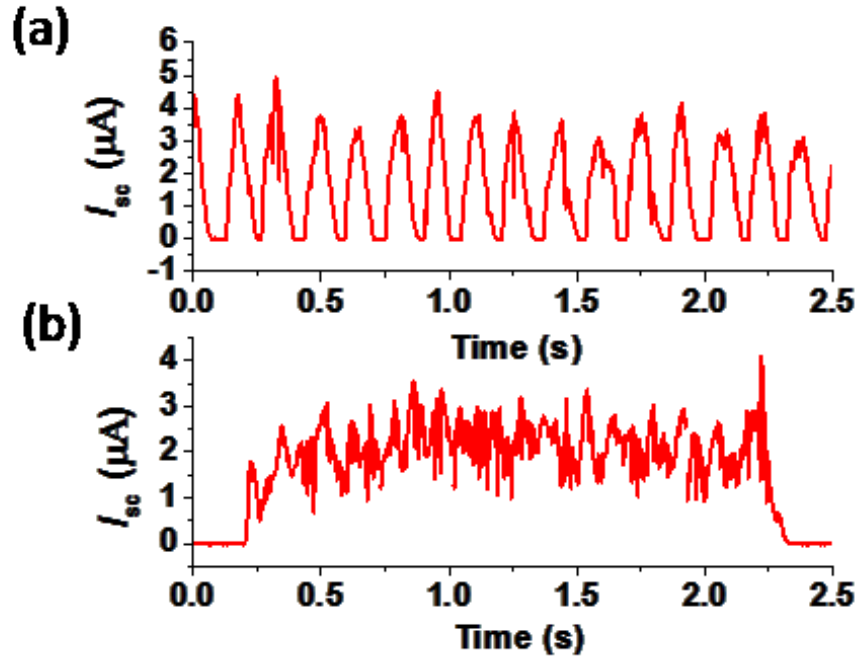


Figure 4-5 (a) and (b) shows short-circuit current (I_{sc}) under the linearly reciprocating mode and the circularly rotating modes, respectively.

4.2.3 Oxide thickness-dependent current output

To reveal the current generation mechanism, the silicon oxide samples with different d were prepared by atomic layer deposition (ALD)⁸⁵ (see Methods for experimental details). Fig. 4-6 shows the I_{sc} output as a function of d . It can be seen that the current signal decays exponentially with increasing d . Since the oxide is very thin, triboelectric electrons may quantum mechanically tunnel through the insulating layer (Inset, Fig. 4-6).¹¹⁷

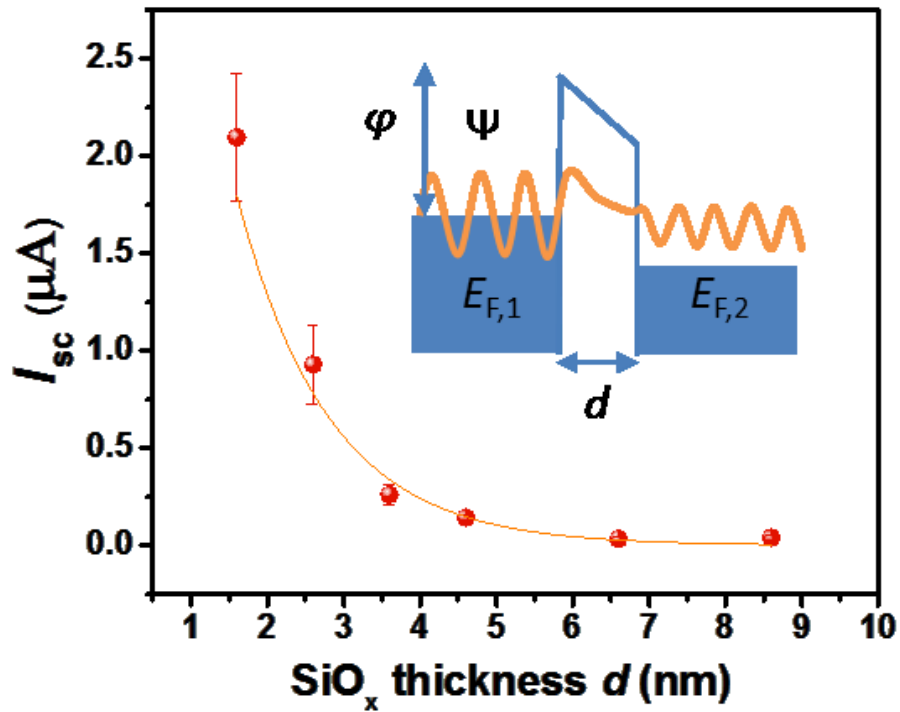


Figure 4-6 I_{sc} vs. d . Silicon samples with different surface oxide thickness were prepared by atomic layer deposition (ALD). The error bars represent standard deviations of the data collected from 15 testing cycles. The solid orange line is the exponential decay fitting of the data points. Inset: one-dimensional tunneling junction. The wave function ψ of the electrons shows an exponential decay inside the barrier, and there is a finite probability that the electrons can tunnel through it.

4.3 Voltage output characteristics of the MIS triboelectric contact

4.3.1 Macroscale voltage output

Figs. 4-7a and 4-7b show open-circuit voltage V_{oc} for the linearly reciprocating mode and the circularly rotating mode, respectively. It was observed that a continuous potential difference of 300-400 mV was observed during the probe-sample frictional contact, which indicates the presence of a potential drop in the space charge region of interface. In contrast, V_{oc} in an intimate polymer-metal contact is negligible since the positive and negative charges are confined in a two-dimensional sheet plane.¹⁰ Therefore, V_{oc} in a polymer-based TENG cannot be observed unless the two counterparts are separated in a vertical mode or mismatched in a horizontal plane.^{10,34}

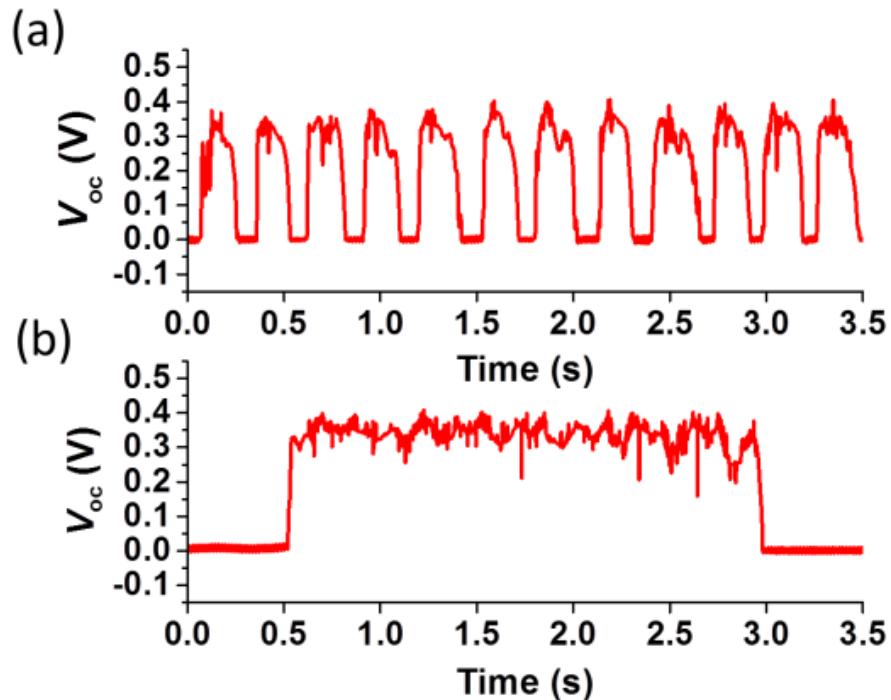


Figure 4-7 Open-circuit voltage (V_{oc}) under (a) a linearly reciprocating mode and (b) a circularly rotating modes, respectively.

The continuous features of V_{oc} and I_{sc} indicate that both driving force and carrier conduction in our case differ from those in the polymer-based TENGs. When a semiconductor such as silicon is brought into contact with a metal, diffusive carrier transport would take place due to the Fermi energy difference between the two materials until thermodynamic equilibrium is achieved (*i.e.* Fermi energy alignment and energy barrier formation, Figs. 4-8a and 4-8b).¹¹⁸ While this process also occurs at a polymer-metal interface in conventional TENGs, the transferred charges are always trapped on the insulating surface, accounting for the high voltage built-up in the system.¹⁰ Although those electrostatic charges can be utilized by generating dielectric displacement current, the current density is inherently limited.¹⁰

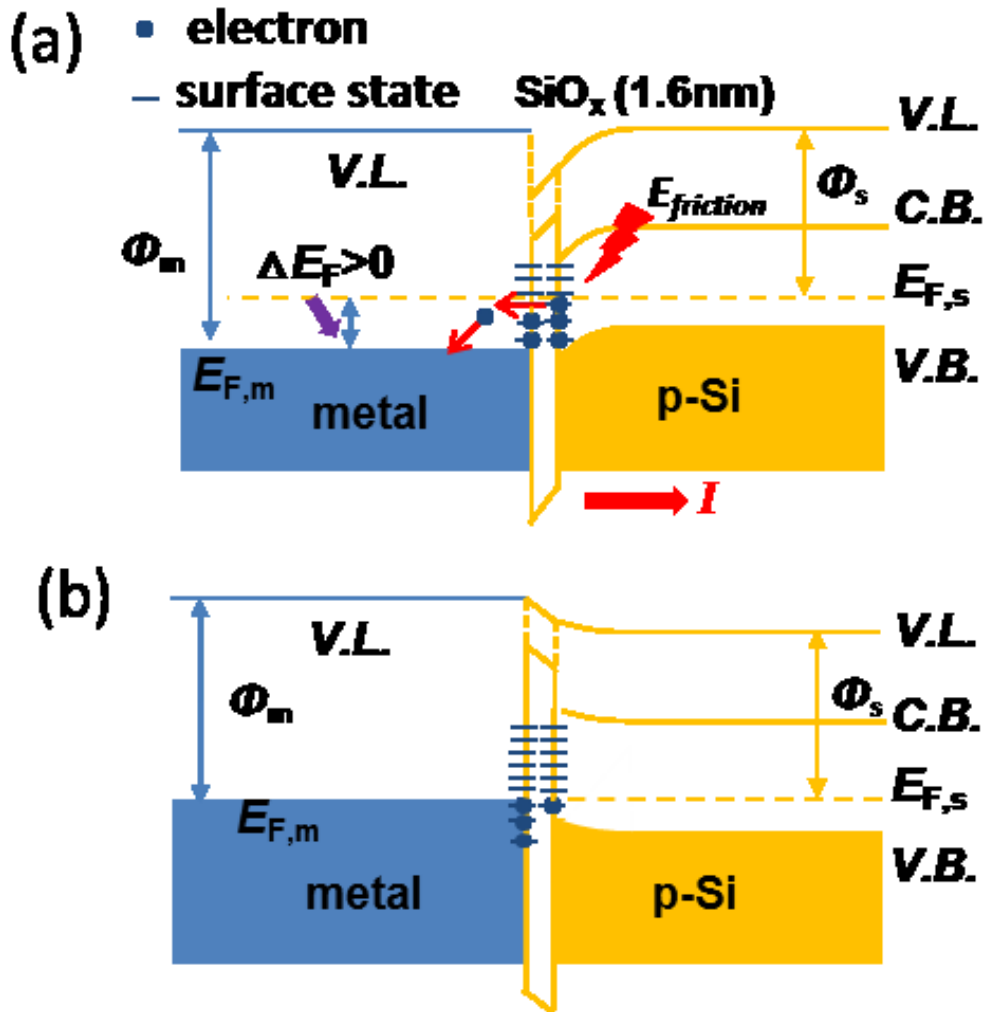


Figure 4-8 Band diagrams of MIS frictional contact under (a) non-equilibrium, $\Phi_m > \Phi_s$ and (b) equilibrium, $\Phi_m > \Phi_s$; where Φ_m and Φ_s are work functions of metal and semiconductor, respectively. Electrons may tunnel through the thin oxide layer and be conducted in the semiconductor.

4.3.2 Bias-dependent C-AFM current output

Fig. 4-9 shows that the triboelectric current measured in C-AFM experiment can be nullified and reversed by applying an additional bias voltage (V_{bias}), which is similar to the determination of photovoltaic open-circuit voltage V_{oc} in solar cell characterization.¹¹⁹ This null method has been successfully used to estimate V_{oc} in the AFM studies of TENGs.^{68,112} When $V_{\text{bias}} < V_{\text{oc}}$ is applied, the relative potential difference between the probe and the sample would decrease, giving rise to a decreasing current output. The relative potential difference may be reversed by applying $V_{\text{bias}} > V_{\text{oc}}$, thus resulting in a current output in the opposite direction.

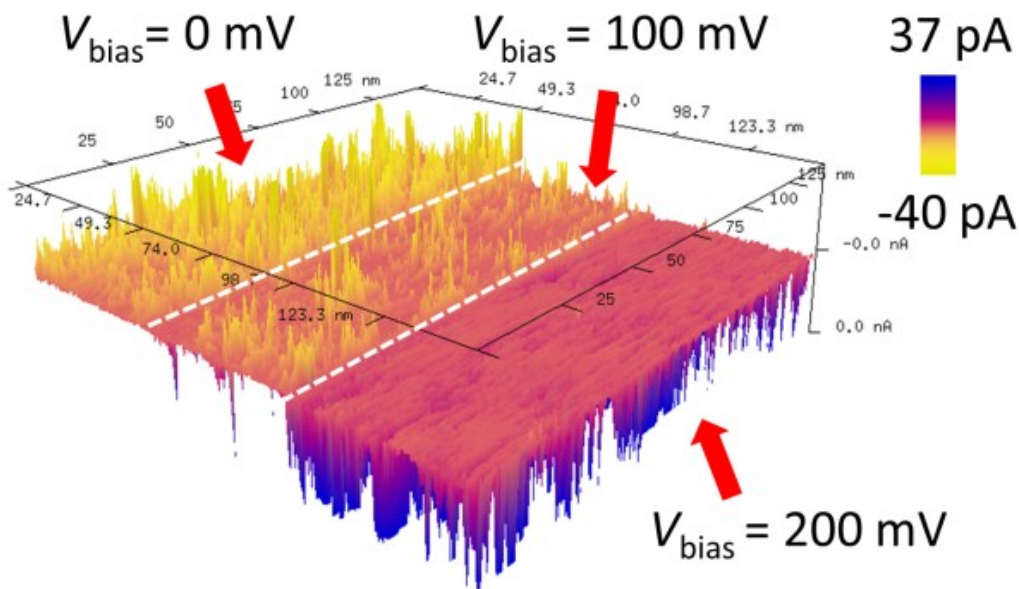


Figure 4-9 Bias voltage-dependent current maps. With the presence of sample bias, the triboelectric current may be nullified or reversed by lowering or reversing the relative surface potential difference, respectively.

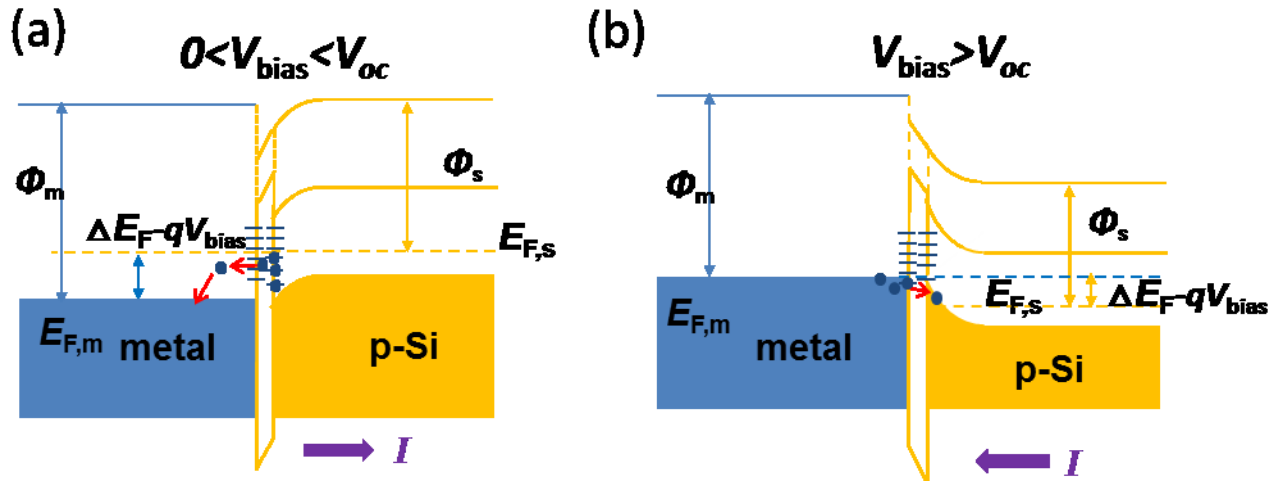


Figure 4-10 Band diagrams of MIS frictional contact under external bias

4.3.3 Oxide thickness-dependent voltage output

Fig. 4-11 shows the V_{oc} and the electric field (E_{loc}) across the surface oxide as a function of oxide thickness (d). It can be seen that V_{oc} first increases and then saturates with increasing d , which may be related to the trade-off between the increasing capacitance and the decreasing triboelectric charge density.⁶⁸

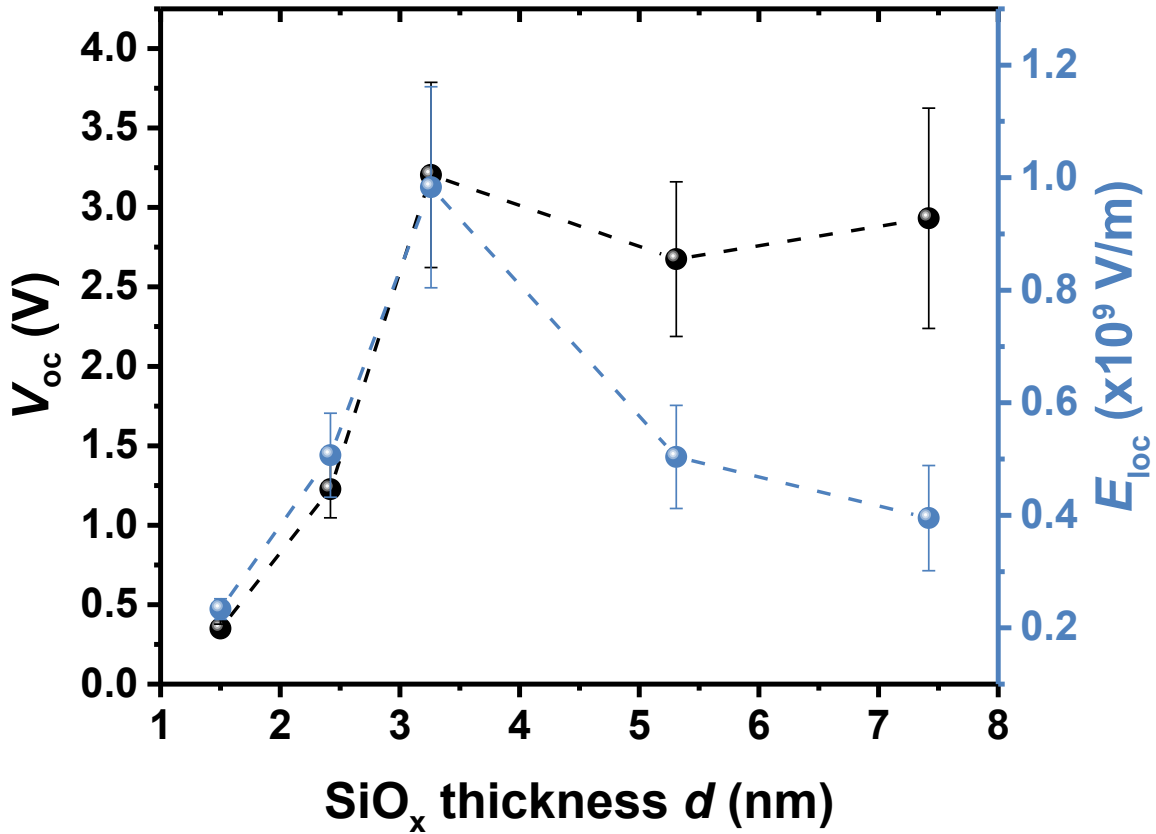


Figure 4-11 Oxide-dependent open-circuit voltage out and local electric field

4.4 Influence of metal work function on V_{oc} direction

As for the triboelectric charge transfer process (contact electrification), many different mechanisms have been proposed, such as: work function difference, ion transfer, and material transfer.⁵⁸ It is evident that the contact potential difference between the tip and sample plays an important role in our case. Figs. 4-12a-c shows the V_{oc} output collected with copper (work function $\Phi=4.53-5.1$ eV)¹²⁰, gold ($\Phi=5.1-5.47$ eV)¹²⁰ and aluminum ($\Phi=4.06-4.26$ eV)¹²⁰ probes (DigiKey Electronics, USA), respectively. Interestingly, it can be seen that V_{oc} measured with the aluminum-coated probe exhibits reversed polarity (i.e. $V_{oc} < 0$).

It is noteworthy that the negative voltage here is from sample to tip because of the electrical connection, which is opposite to that in the nanoscale C-AFM testing. According to Bardeen's theory on an MS electrical contact, the Fermi level at the silicon surface is generally considered to be pinned due to the existence of surface states.¹²¹ As a result, Schottky energy barrier is dominated by the surface states pinning effect and less sensitive to the metal work function, which may explain the similar V_{oc} output from gold or copper-coated stainless steel probes. However, since the work function of aluminum is much smaller than those of other metals, it is possible that the Fermi energy of aluminum is higher than that at SiO_x surface and thus gives rise to the reversed surface potential difference.

Meanwhile, the thermoelectric effect can be excluded here since it would require more than 300 °C temperature difference in order to obtain ~300 mV potential difference considering the Seebeck coefficient for moderately doped p-type silicon of ~1 mV/K.¹²²

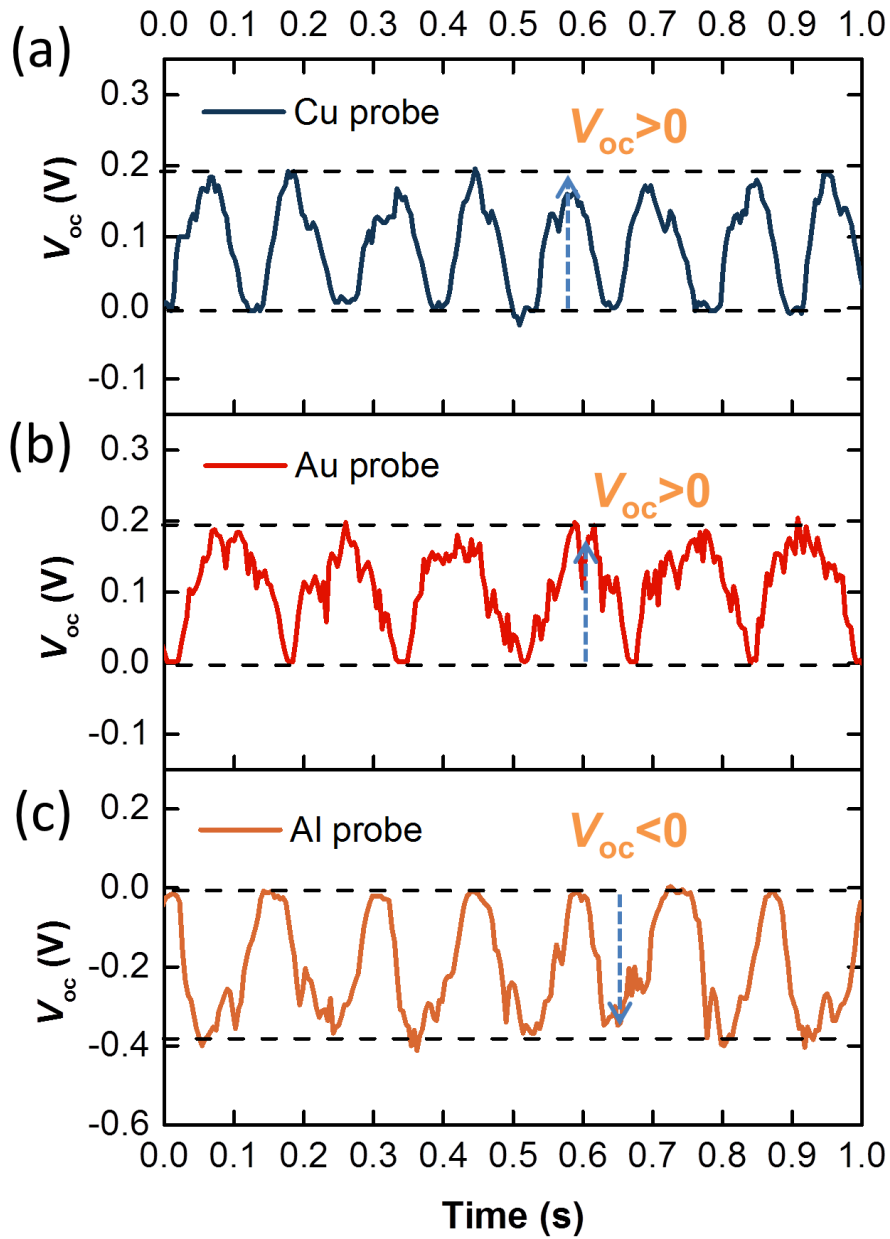


Figure 4-12 V_{oc} output for probes made of different metallic materials (a) Cu, (b) Au, and (c)

Al. It is indicated that the direction of V_{oc} is influenced by the relative surface potential difference between the metal and semiconductor surface.

4.5 Si doping type/concentration-dependent V_{oc} output

Fig. 4-13 shows the Si doping type/concentration-dependent V_{oc} output. Considering the wide doping concentration variation from degenerate n-type to degenerate p-type, the E_F level of the samples should vary largely with a magnitude no less than the Si bandgap (~ 1.1 eV).

Interestingly, it is shown that the direction of V_{oc} does not show a proportional dependency on the doping concentration. Therefore, we propose that V_{oc} may be more related to the contact potential difference between the tip and sample surface, which is the oxide layer. As for the magnitude of V_{oc} , surface state density may play a significant role. In order to reveal the determining factor of V_{oc} direction, more experiments would be needed.

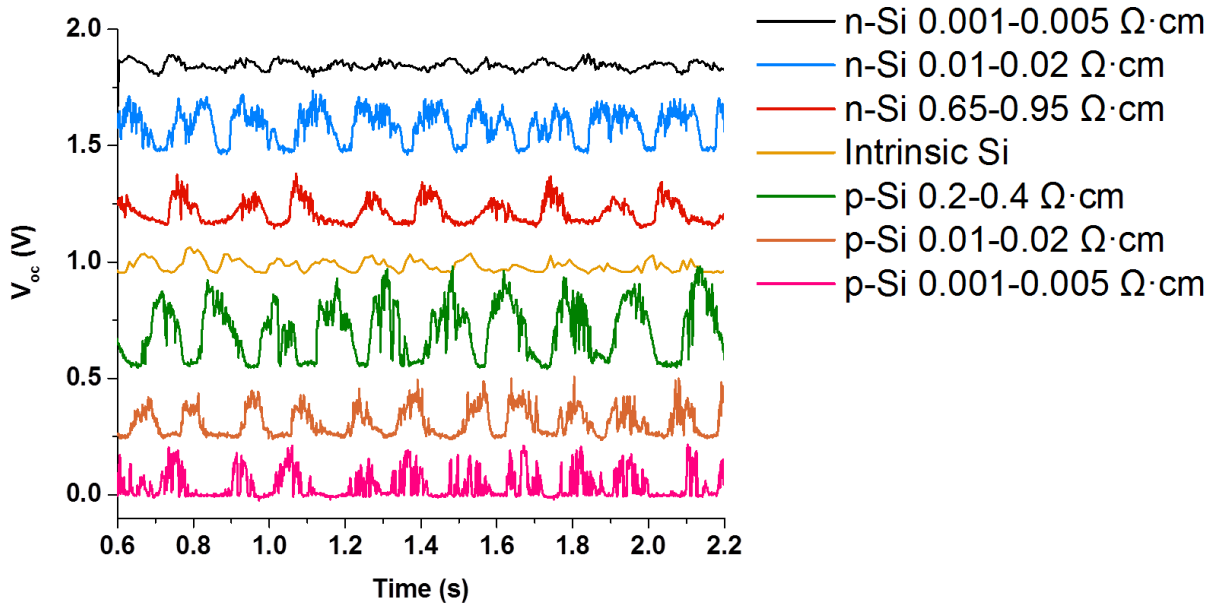


Figure 4-13 Si doping type/concentration-dependent V_{oc} output

4.6 Discussion of tribo-tunneling transport mechanism

From the experimental results, it is evident that the charge conduction mechanism in an MIS frictional system is very different from the dielectric displacement current method used in polymer-based TENGs. The tunneling mechanism in the MIS structures may be a combination of Fowler-Nordheim (F-N) tunneling (field emission) and direct tunneling.¹¹⁷ In the F-N tunneling mechanism, electric field across the thin insulator is sufficiently high to bend the conduction band of the insulator in such a way that the electrons tunnel across a triangular energy barrier.¹¹⁷ On the other hand, if the voltage across the SiO₂ is small (less than 3.1 V for SiO₂/Si interface) and oxide thickness is less than 3.5 nm, the electrons tunnel across the full oxide thickness resulting in direct tunneling.¹¹⁷ Considering the triboelectric V_{oc} (hundreds of mV) and native oxide thickness (~1.6 nm) in our case, the d.c. output should be generated by direct tunneling of the triboelectric electrons through the insulating oxide layer.¹¹⁷ Accordingly, the process of current generation in a metal-semiconductor frictional contact with an ultrathin insulating layer in between, may involve three basic steps: i) triboelectric charge generation at the metal-insulator interface, ii) quantum mechanical electron tunneling through the ultrathin insulating layer and iii) carrier conduction in the semiconducting material.

According to quantum mechanics, a particle with energy E less than the barrier height (ϕ_B) has the probability to penetrate the forbidden region (Fig. 4-1j).^{117,123} The wave function ψ decays exponentially in the forbidden region as expressed by¹²³:

$$\psi(d) = \psi(0) \exp\left[-\frac{\sqrt{2m(\phi-E)}d}{\hbar}\right], \quad (4-1)$$

where m is the mass of the particle, and \hbar is the reduced Planck's constant. Accordingly, the direct tunneling current $I(d)$ in an MIS contact can be estimated as^{117,123}:

$$I(d) \sim \exp \left[-\frac{4\sqrt{2q}}{3\hbar} (m_{\text{eff}}\phi_B)^{1/2} \epsilon_{\text{SiO}_2} d \right], \quad (4-2)$$

where, m_{eff} is the effective mass of the electrons. Therefore, the current falls off exponentially as a function of barrier (oxide) thickness. The ultrathin nature of the native oxide layer on Si surface provides an excellent condition for the triboelectric electron tunneling.

Accordingly, it is understandable why conventional polymer-based TENG systems are not able to generate direct current flow: a thick insulating layer (μm range) is usually used in those structures, resulting in triboelectric charges being trapped at the insulator surface. Therefore, the key to generate continuous direct current is to continuously draw those charges out from the contact region, and quantum mechanical tunneling and doped silicon with sufficient electrical conductivity provide excellent mechanism and environment to drain the carriers. It is worth asking the question if we can achieve the same process in a metal-metal frictional contact. In terms of harvesting d.c., the answer would be a theoretically possible, but technically hard to achieve due to the instantaneous realignment of Fermi-energy in a metal-metal frictional contact (like 'pushing' an incompressible fluid of electrons). It is extremely difficult to directly harvest the energy within such a short time scale. Instead, the frictional energy between two different metals would most likely dissipate into heat.

4.7 Conclusion

In summary, we have demonstrated that d.c. triboelectricity with high current density can be generated from metal-insulator-silicon frictional contacts using electron tunneling. This concept overcomes the limitations of poor current density observed with traditional mechanical triboelectric harvesting techniques. The mechanism of the driving force for d.c. flow is explained as related to the surface potential difference between the two materials under a thermodynamic non-equilibrium condition. The characteristic of the measured current is consistent with quantum mechanical tunneling of charge carriers through the ultrathin oxide. The three orders of magnitude enhancement in the current density in this technique, from 10 A/m^2 to 10^4 A/m^2 , is attributed to the highly intensified local electric field in a point-plane contact configuration, which results in a non-equilibrium charge transport at the tip-sample contact interface.^{112,124} This nano-scale effect indicates that the overall current output can be scaled-up and can be dramatically improved by introducing parallelized nanostructures, such as nano-tip array¹²⁴ or nanoparticle modification³² into the contact interface. With a deeper understanding of the mechanism, optimized materials, and improved device configurations, we would expect a promising future for the scaled-up d.c. triboelectricity harvesting.

Chapter 5 Scaling-up of the tribo-tunneling concept for practical application

In the previous chapters, we have introduced the discovery of triboelectric d.c. generation phenomenon (Chapter 4) and the observation of tribo-tunneling effect in metal-Si frictional contact system (Chapter). With modern nanotechnologies such as atomic force microscopy (AFM), pulsed laser deposition (PLD), and atomic layer deposition (ALD), a number of fundamental physics of the phenomena have been investigated. In order to apply the novel concepts into practical application, however, tremendous efforts from engineering perspective are needed. To this end, we have conducted some preliminary work, exploring the possible scaling up of these concepts towards real application.

5.1 Macro-scale demonstration of d.c. generation on MoS₂ sample

We demonstrated the concept by manually sliding a metallic spring connector on a MoS₂ thin film by hand (Fig. 5-1). The spring connector was electrically connected with the Ag surface, and current output was monitored by a picoammeter (6485, Keithley) (Fig. 5-1a). As shown in the Supplementary Video, a DC output of 10-100 nA was observed. The spring connector is regarded as a macroscale “tip” with a tip radius $R \approx 1$ mm (Fig. 5-1c). Contact area A can be estimated by a simple Hertz model.

For the macroscale demonstration, additional adhesion can be neglected, thus A is approximated by Hertz model⁵⁹:

$$A = \pi \left(\frac{RL}{K} \right)^{2/3} \quad (5-1)$$

Here, $E_t = 165$ GPa, $\nu_t = 0.22$ is adopted for the AFM tip, $E_t = 79$ GPa, $\nu_t = 0.42$ is adopted for gold-coated metallic connector, and $E_t = 240$ GPa, $\nu_t = 0.27$ is adopted for MoS₂ thin film. In the macroscale demonstration, the applied load L can be roughly estimated to be in the order of 1~10 N by hand.

Accordingly, $A \approx 1.5 \times 10^{-9}$ m² and current density J in the order of 10-100 A/m² was obtained. The current density J here is several orders smaller compared with the one obtained from C-AFM measurement since J is determined by the electric field E , which is extremely intensified under the nano-tip with large curvature.

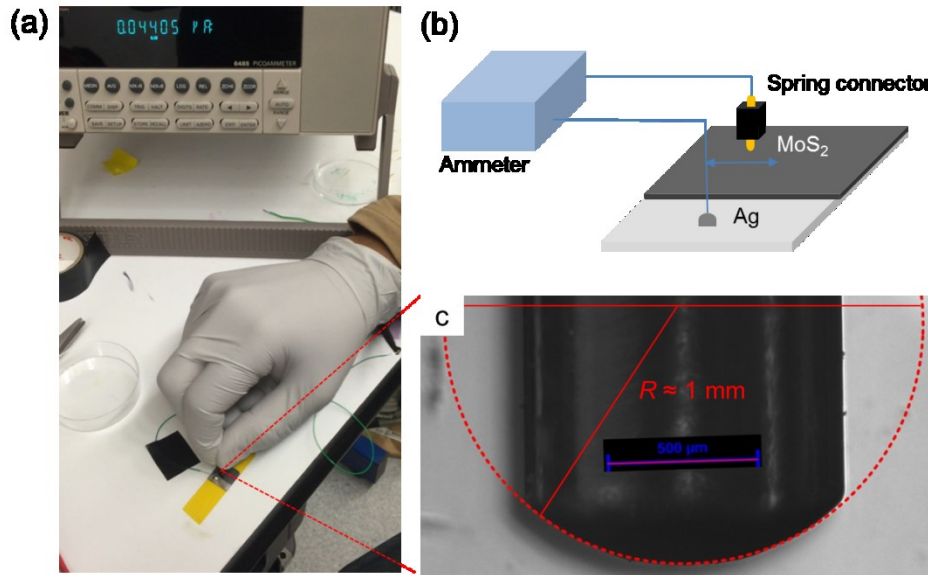


Figure 5-1 Manually driven system (a) Schematic of the setup. (b) Optical microscopy image of the connector front.

5.2 Power generation with silicon-based tribo-tunneling system

5.2.1 V, I, P output vs. electric load R

To demonstrate the possibility of extending the idea of using Si-based tribo-tunneling junction for practical applications, we have carried out experiments as shown in Fig. 5-2. Fig. 5-2a shows the current (I) and voltage (V) outputs as a function of external electrical load (R). Since the equivalent circuit components in our case is relatively simpler, which can be approximated as a DC voltage source, an internal resistance and an external resistance connected in series. Therefore, V, I and P can be modeled as:

$$V = V_{oc}R/(R + r), \quad (5-2)$$

$$I = V_{oc}/(R + r), \quad (5-3)$$

$$P = V_{oc}^2 R/(R + r)^2, \quad (5-4)$$

The fitting results are shown in Fig. 5-2. An increasing V and a decreasing I can be observed as a function of increasing R . Fig. 5-3 shows the J and the power density vs. R , which is estimated by normalizing I and power output (P) data with the A (0.1 mm^2), respectively. Specifically, the peak power output (P_{\max}) can be found around $R \approx 100 \text{ k}\Omega$, of which the R value is close to the internal resistance r of the power generation unit (see Methods for discussion). The high J , on the order of $1\text{-}10 \text{ A/m}^2$, results from the much lower impedance of the device compared with polymer-based TENGs. It is noted that the current output is very sensitive to the resistance between the top and bottom electrodes.

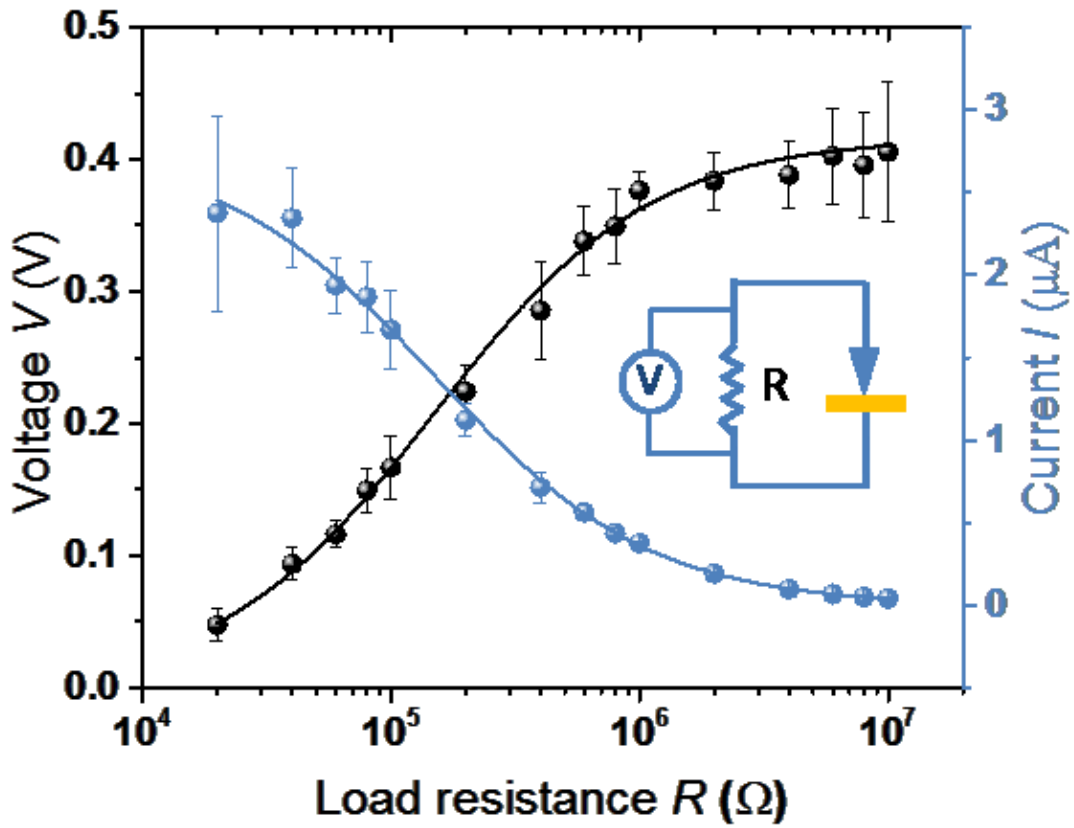


Figure 5-2 V and I output as a function of electrical load R . The solid curves for V and I are the fitting results by Eq. 5-2 and 5-3, respectively. Error bars represent standard deviations of the data collected from 30 testing cycles. Inset: equivalent circuit

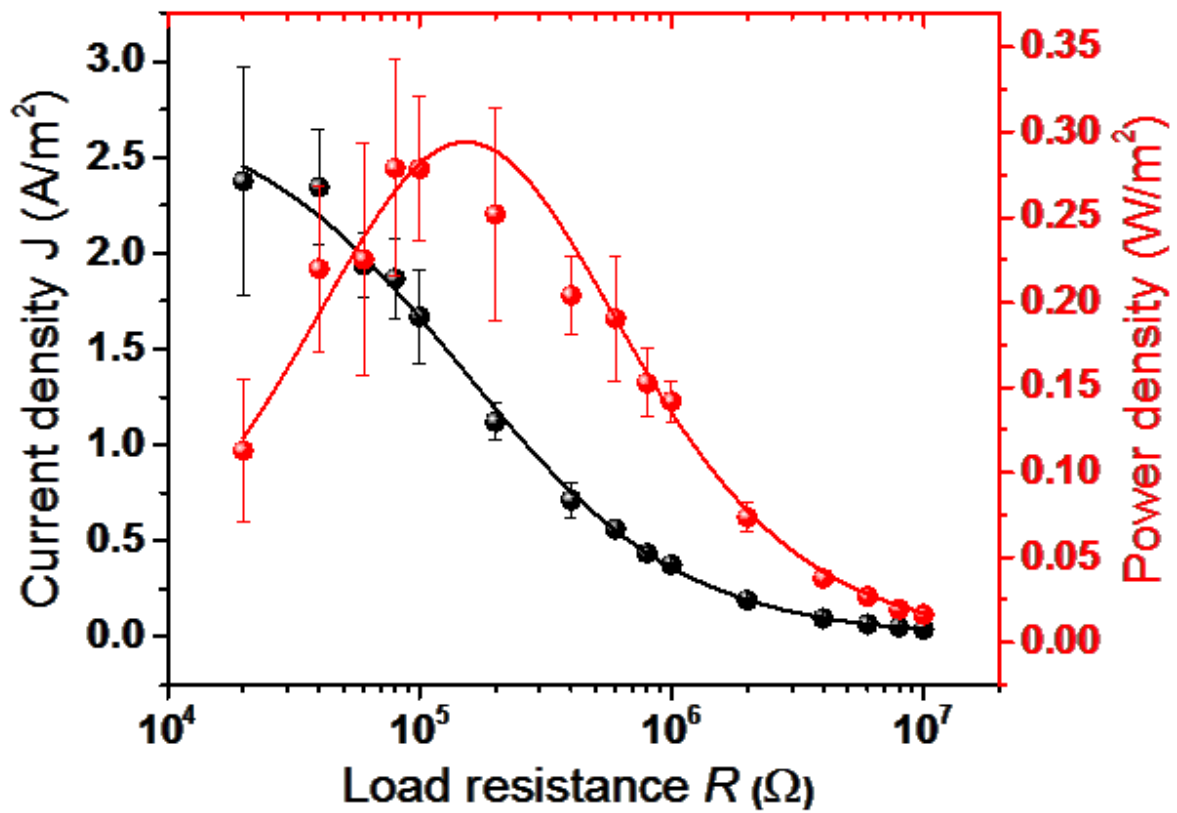


Figure 5-3 J and power density as a function of R . The power output (P) vs. R is fitted with

Eq. 5-4 in Methods.

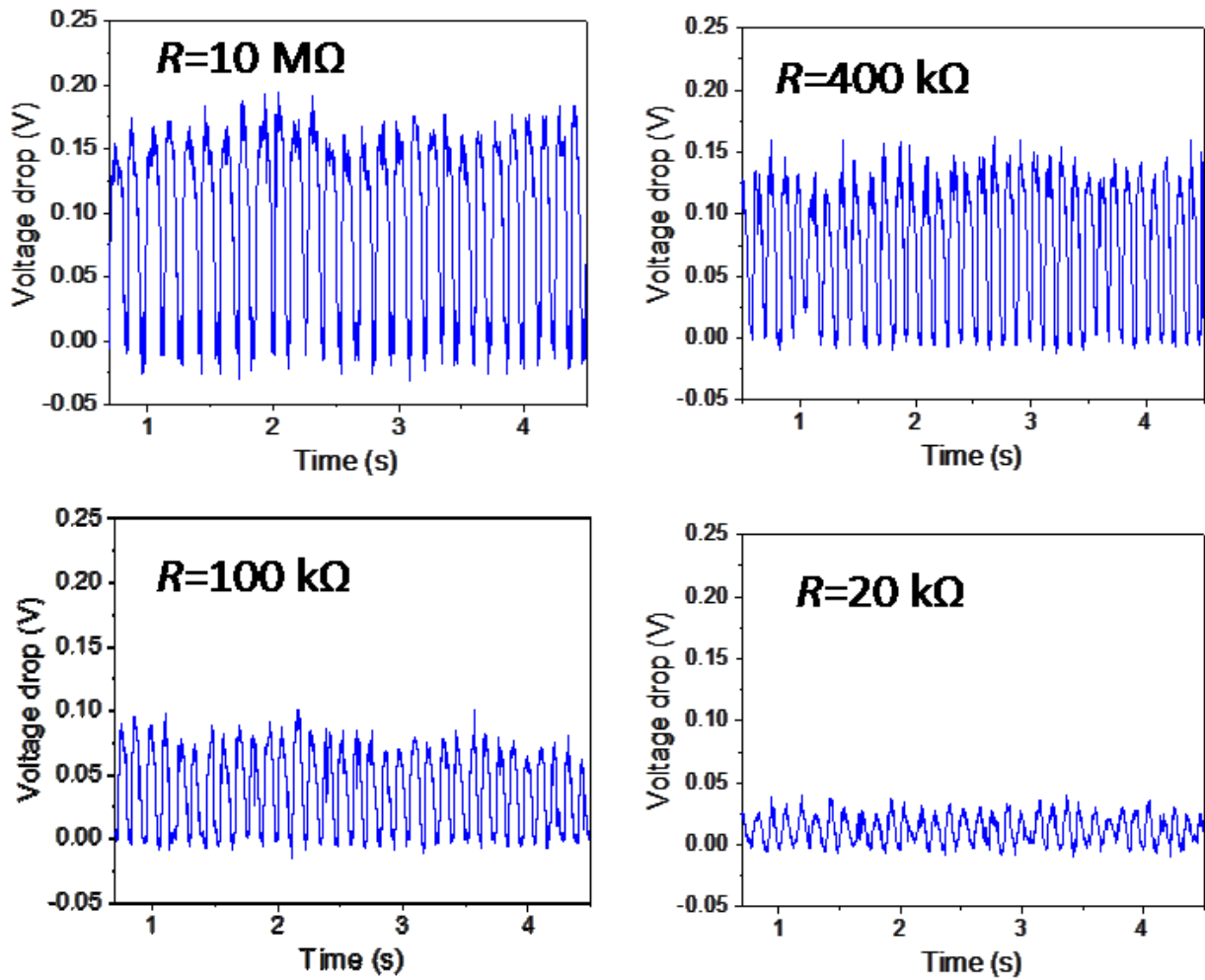


Figure 5-4 V across electrical load R with $10\text{ M}\Omega$, $400\text{ k}\Omega$, $100\text{ k}\Omega$ and $20\text{ k}\Omega$ recorded by an oscilloscope.

5.2.2 Doping type/concentration-dependent V , I , P output vs. electric load R

Fig. 5-5 and 5-6 show the I and V output as a function of electrical load R with different p type-Si doping concentration, respectively. It can be seen that the current output decreases and the voltage output increases with increasing R with all the doping concentrations. It should be noted

that the bottom electrode for all samples are e-beam evaporated Al coating, which, in fact, does not form good ohmic contact with the intrinsic Si sample and the ones doped with low concentration. Although it is apparent that the increasing doping concentration can lower the internal resistance of the d.c. generator system, it is not clear here whether it will influence the surface states density and surface potential level on the SiO_x surface.

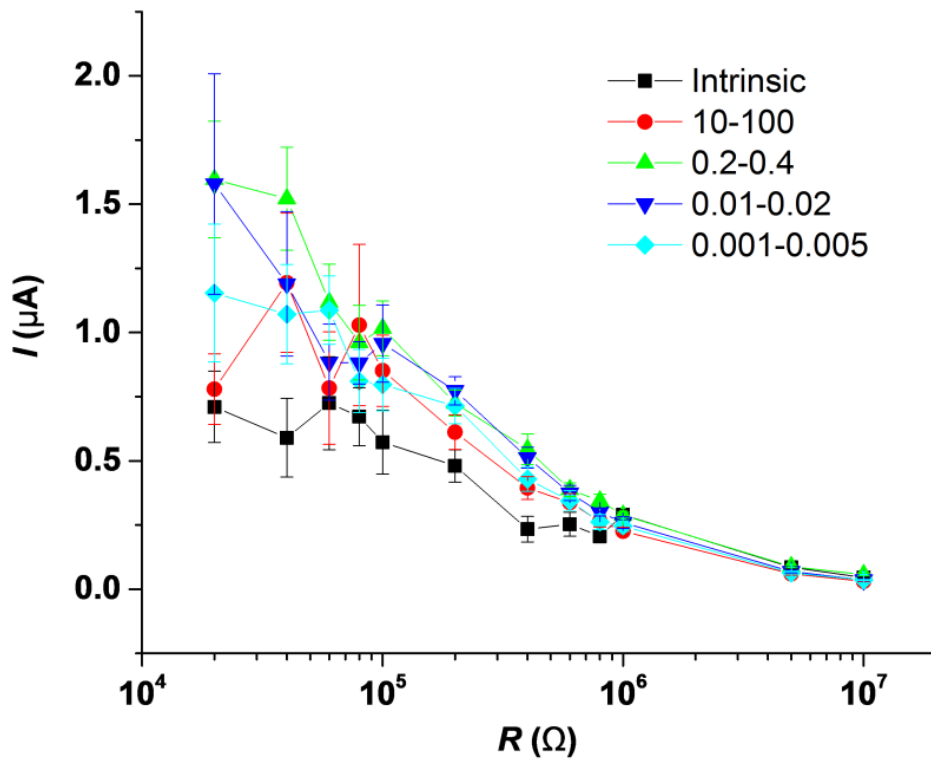


Figure 5-5 I output as a function of electrical load R with different p type-Si doping concentration (Unit in the insert: $\Omega\cdot\text{cm}$)

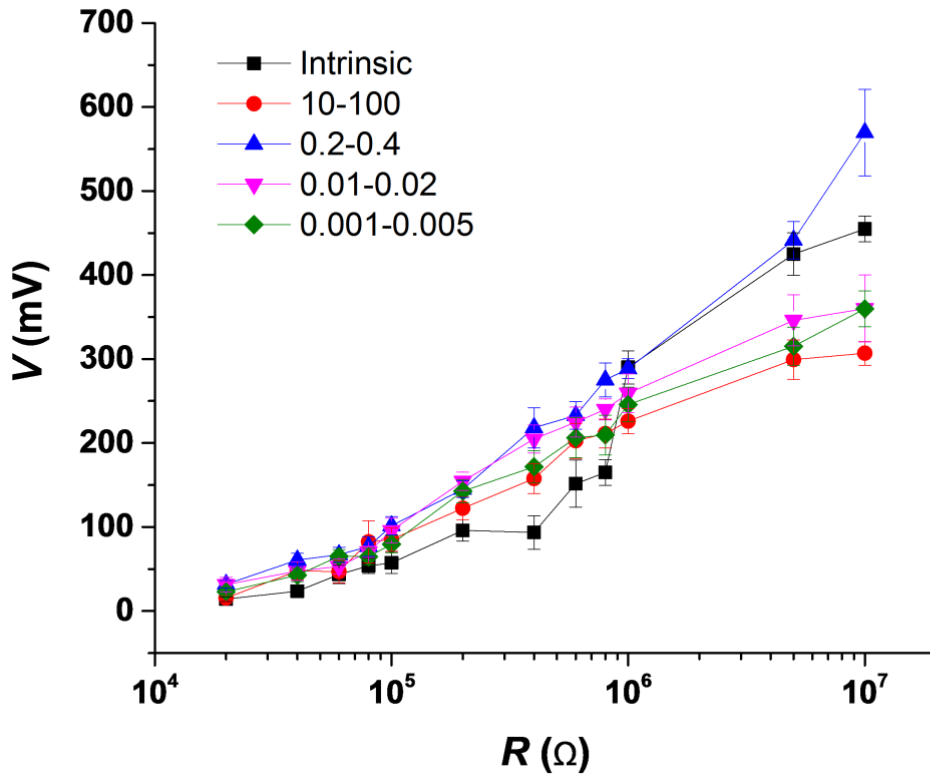


Figure 5-6 V output as a function of electrical load R with different p type-Si doping concentration (Unit in the insert: $\Omega\cdot\text{cm}$)

5.2.3 Charging capacitor with d.c. triboelectricity

The I - V data of the Si-based MIS system was collected by a Keithley 2450 SourceMeter SMU (Tektronix, USA) as shown in Fig. 5-7. Fig. 5-7a and 5-7b shows the schematic of the testing I - V testing system and the I - V curve of the MIS structure, respectively. A typical rectifying diode feature can be seen from Fig. 5-7b.

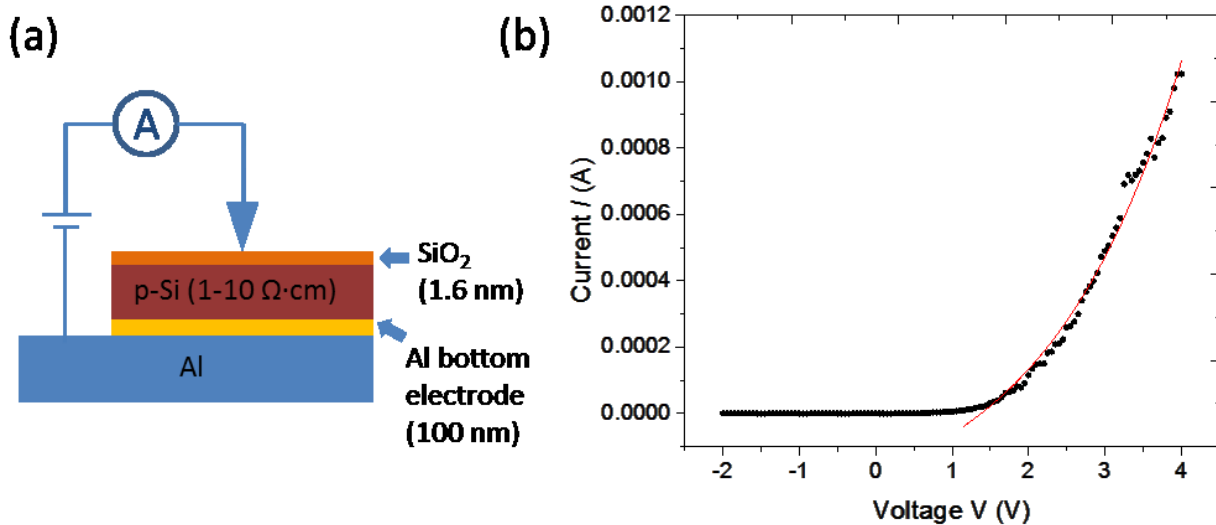


Figure 5-7 (a) Schematic of the testing I-V testing system; (b) I-V curve of the MIS structure

To demonstrate the storage of triboelectricity, we have carried out capacitor charging experiments as shown in Fig. 5-8. The $V-t$ data was collected by a Keithley 2450 SourceMeter SMU (Tektronix, USA). A single macroscale probe was manually rubbed on the silicon sample surface, generating d.c. current and charging the capacitor without any rectification. It shows that an 80 μF capacitor was charged up to 200 mV within one minute. Compared with the transient a.c. power output with low J , the d.c. output with high J described here is expected to bring simplicity in power conditioning and power management. Theoretically, the $V-t$ curve can be fitted by:

$$V = V_b (1 - e^{-\frac{t}{RC}}), \quad (5-5)$$

where $V_b \approx V_{oc}$ and $R \approx r$. The fitting result is shown in Fig. 5-8.

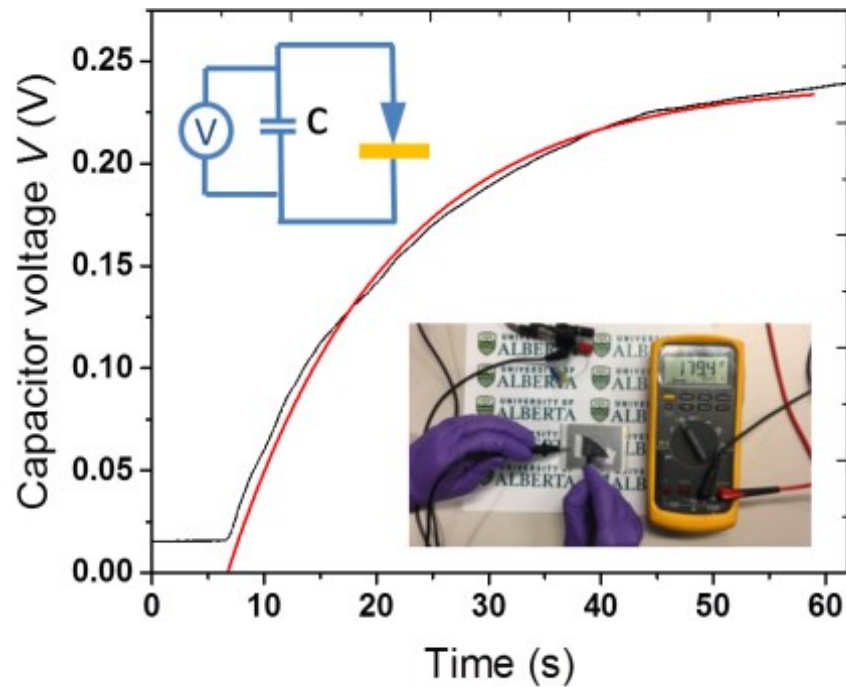


Figure 5-8 Time-dependent voltage built-up of a capacitor C ($80 \mu\text{F}$) charged by the d.c. triboelectricity. No additional rectification has been used. The solid red curve is the fitting result by Eq.5-5. Inset: equivalent circuit (top-left); captured image of the charging process (bottom-right).

5.2.4 Automatic motor system

It should be noted that the manually driving method does not have a precise control of the sliding force and speed. To address this issue, a homemade automatic motor system as shown in Fig. 5-10 has been designed, consisting of a DC motor with controlled speed, and a spring connector with controlled contact force. The V_{oc} output is monitored by an oscilloscope as shown in the picture. It can be seen that output is very consistence. This system will be used in our future work.

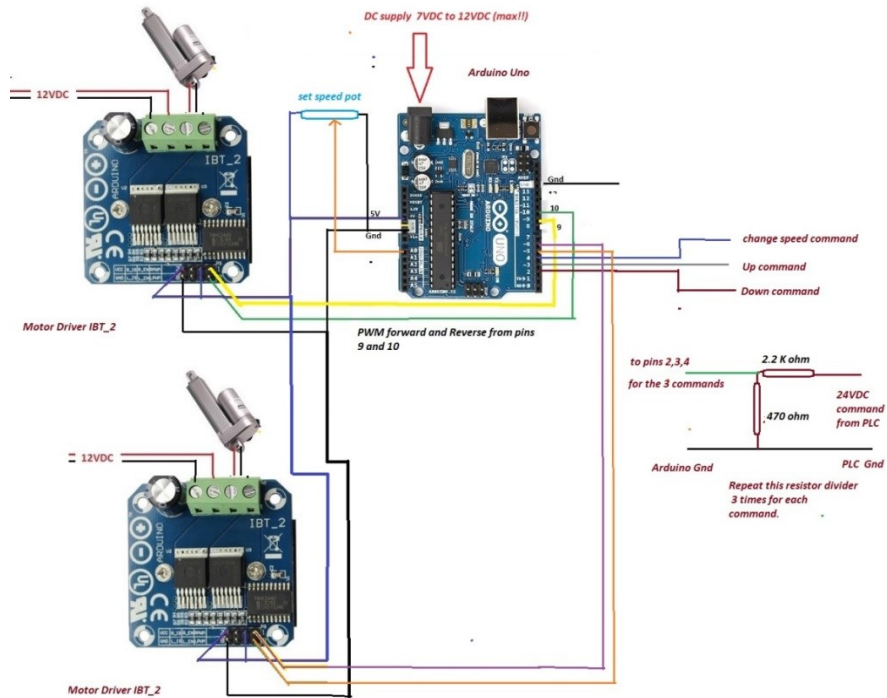


Figure 5-9 Controlling system for the automatic motor

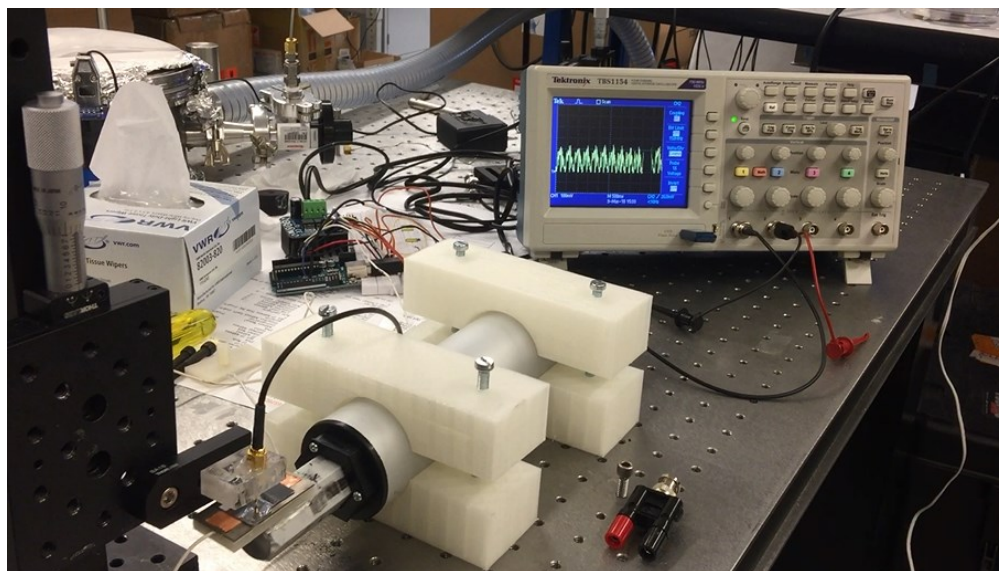


Figure 5-10 A homemade automatic motor system; The contact force and sliding speed can be controlled by a spring-connected probe and the motor, respectively.

5.2.5 Design and fabrication of tip array system

Compared to the polymer-based TENGs, the tribo-tunneling-based TENG has relatively lower voltage output. Our recent experimental results at macro-scale show that the current and voltage can be scaled up by making the probes in parallel and in series, respectively. Fig. 5-11 shows the voltage output recorded with a spring connector array (16 gold-coated pins in series) driven by the motor. While the single spring connector can generate a V_{oc} of 10~20 mV, it can be seen that the voltage output reaches 100 mV level with the series-connected pin array, which could be further boosted with increasing number of pins and electrode surface modification at nanoscale.

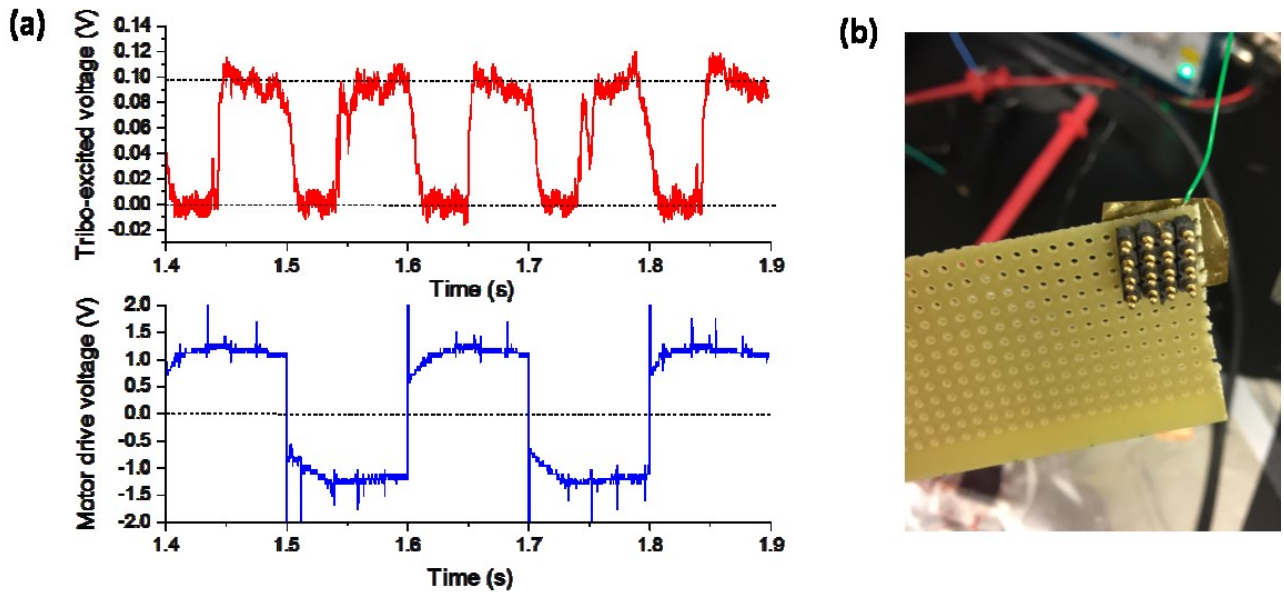


Figure 5-11 (a) Triboelectric voltage output (top) and its corresponding motor drive voltage vs. time (bottom). To drive the tips go back and forth, an AC square wave was applied to the motor. The observed duty circle is understandable because of the mechanical delay. The voltage output reaches 100 mV level. (b) Photo of the spring connector array. 16 pins are electrically connected in series.

It is proposed that the relatively low voltage output may be related to the tip radius: the sharper the tip, the higher the pressure applied to the sample, resulting in higher triboelectric charge density. To address the issue as well as explore the possible scaling-up of the concept for real application, a micro-tip array system has been designed as shown in Fig. 5-12. The tip array holder and sample holder is fabricated by 3D printing as shown in Fig. 5-13. It will be optimized and tested in our future work. Moreover, it is expected that an enhanced power output can be obtained with miniaturized tip array system.

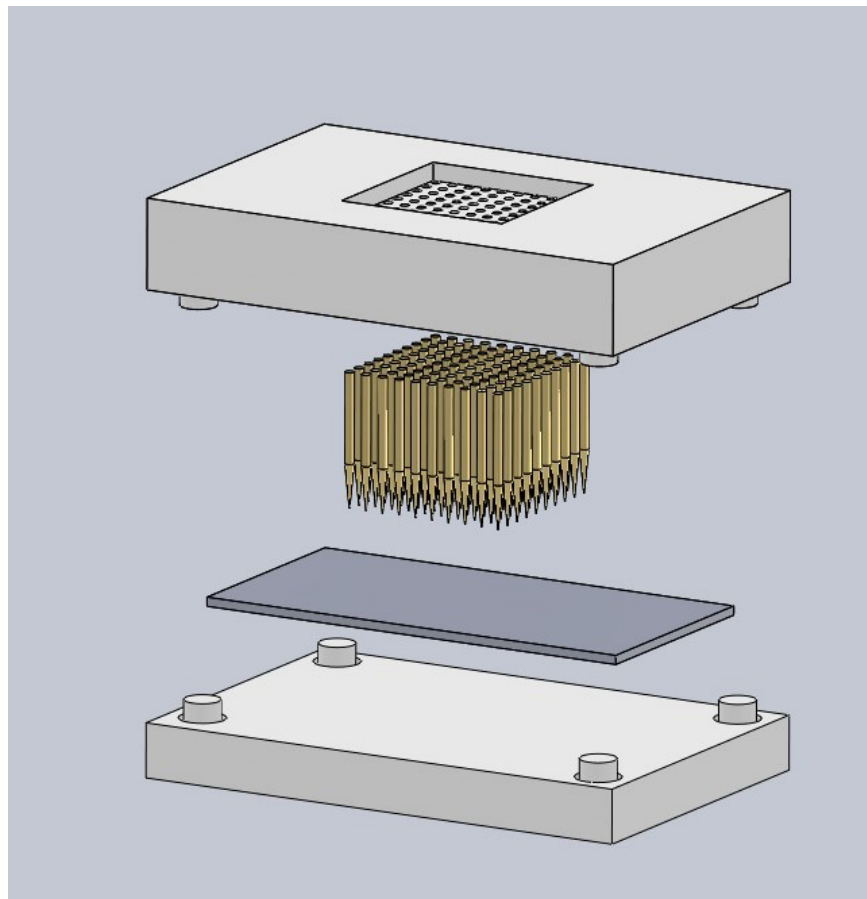


Figure 5-12 A prototype of tip array system

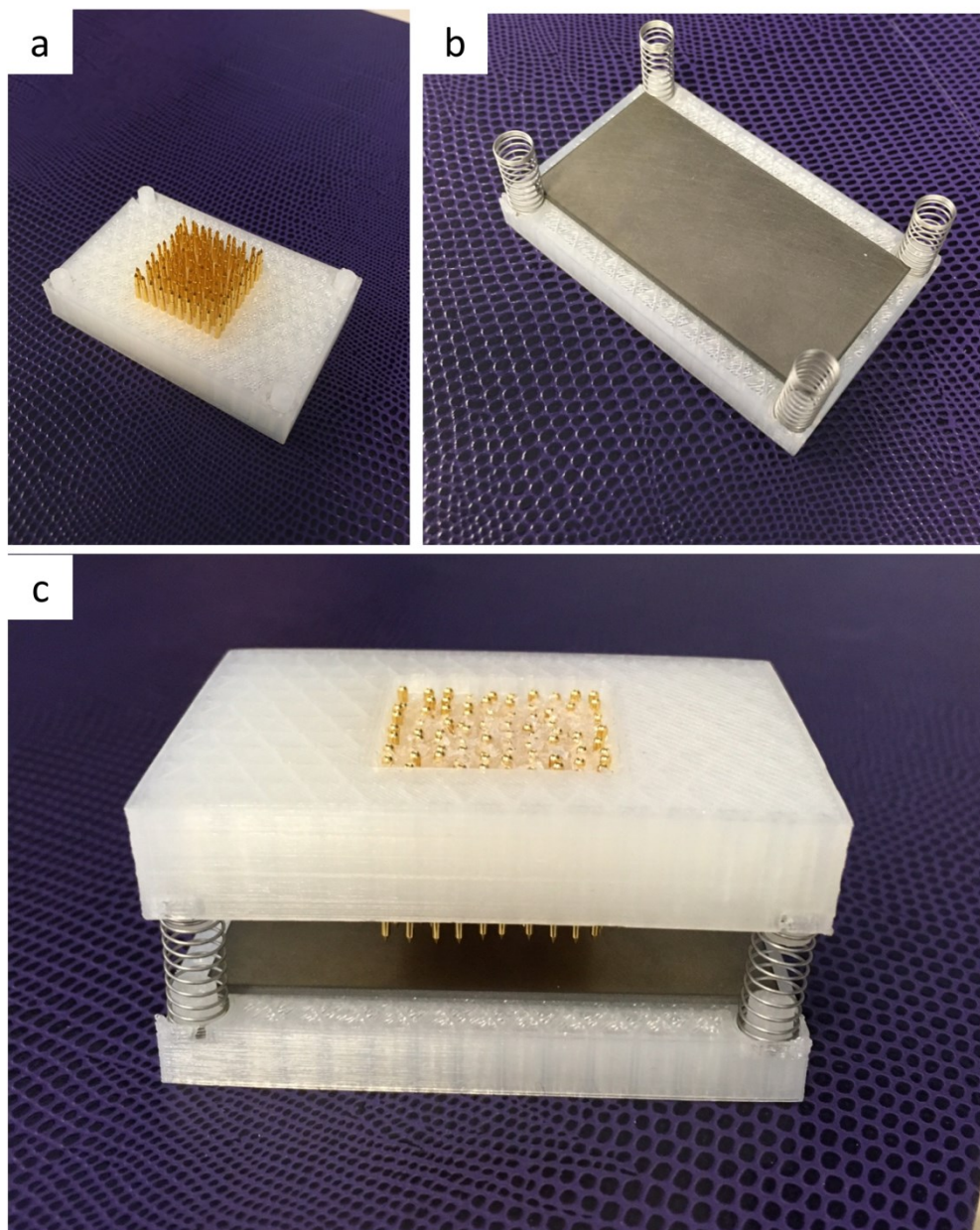


Figure 5-13 3D printed tip array system

Chapter 6 Conclusion and future work

6.1 Conclusion

Converting mechanical energy into direct-current (d.c.) power with sufficient current density is one of the key challenges for mechanical energy harvesting technology. Traditional methods such as piezoelectric or triboelectric generators are known for producing extremely high electric potentials, but not high current. Reported current density in conventional piezoelectric or triboelectric power generation is alternating current (a.c.) and extremely small.

In this thesis, we present the observation of generating high current density through frictional sliding of nanoscale contact on layered MoS₂ thin films (Chapter 3). In this work, we have experimentally measured very high direct current (d.c.) electricity generation (high current density of 10^7 A/m²) during frictional contact of conducting atomic force microscopy (AFM) tip on MoS₂ thin layers with fundamentally different mechanism. The d.c. electricity can be generated without any rectification or external bias. We have systematically characterized this novel phenomenon and the results. We explain the phenomenon using a model based on thermionic emission during frictional sliding. Our experimental results fit very well with the theory. The method is scalable for generating d.c. electricity directly from mechanical motion. This work has been recently published in Nature Nanotechnology (Liu, et al. Nature Nanotech. 2018, DOI: 10.1038/s41565-017-0019-5).

In our first publication, the fundamental mechanism is elusive, and its universality is not clear. In order to further reveal the working principle of the phenomenon, as well as to prove its potential for real application, we have conducted study on oxide thickness-dependent tribo-tunneling

current generation. In Chapter 4, we discovered that facilitating electron tunnelling across a triboelectrically charged thin insulator could produce sustainable current without applying an external bias. We have experimentally proven that the mechanism is electron tunnelling by using nanometer silicon oxide films deposited by using atomic layer deposition (ALD). As a result, a large current density is obtained that could be used for practical applications. Ultrahigh C-AFM J of 10^4 A/m² is observed due to the nano-size probe-induced high electric field. We report our experimental results along with quantum mechanical tunnelling theory where both direct tunnelling and Fowler-Nordheim (F-N) tunnelling take place. We also demonstrate universality and scalability of the phenomenon using nano- (Conductive-AFM) and macroscale metal- sliding contact system. A high current density J of 5 A/m² is experimentally measured in doped silicon materials at macroscale. It has been proved that the d.c triboelectricity can be generated and directly stored at macroscale level without rectification. The easy availability, cost-effectiveness, and naturally presented nanometer surface oxide of silicon materials make it as a promising strategy for mechanical energy harvesting.

In summary, the fundamental significance of this thesis lies in:

- 1) An insight into the non-equilibrium electronic excitation at frictional interface has been provided, which enhanced our understanding of energy dissipation in frictional system.
- 2) A novel approach of harvesting triboelectricity has been discovered, overcoming the low current output limitation faced by traditional methods based on dielectric displacement current generation.

6.2 Future work

From a scientific point of view, developing basic theory for explaining the triboelectric tunneling phenomenon is of great importance. Possible approaches may involve a combination of quantum mechanics theory and solid state physics. Since the driving force of tribo-tunneling is determined by the surface chemistry and physics, it is vital to manipulate surface and interface properties (surface states, surface topography, chemistry, adsorption, etc.), in order to boost the generator performance. It is also apparent that materials properties (interface structure, doping concentration of semiconductor, dielectric properties, *etc.*) play an important role on the power output. Therefore, a systematic material optimization is needed. Moreover, it would be interesting to investigate the interaction of tribo-tunneling phenomenon with other physical parameters, such as photon coupling, temperature, magnetic/electric field.

From an engineering point of view, we would need to explore the scaling-up techniques for this concept, for example, with tip array system, three-dimensional stacked system. The incorporation of the idea with flexible substrates may open the routes for developing self-powered wearable electronics. Integrating the concept with energy storage unit would also be intriguing.

Bibliography

- 1 Priya, S. & Inman, D. J. *Energy harvesting technologies*. Vol. 21 (Springer, 2009).
- 2 Harb, A. Energy harvesting: State-of-the-art. *Renewable Energy* **36**, 2641-2654 (2011).
- 3 Brand, O., Fedder, G. K., Hierold, C., Korvink, J. G. & Tabata, O. *Micro energy harvesting*. (John Wiley & Sons, 2015).
- 4 Conti, J. J. Annual energy outlook 2018. *US Energy Information Administration, Washington, DC* (2018).
- 5 Paish, O. Small hydro power: technology and current status. *Renewable and sustainable energy reviews* **6**, 537-556 (2002).
- 6 Kazmerski, L. L. Photovoltaics: A review of cell and module technologies. *Renewable and sustainable energy reviews* **1**, 71-170 (1997).
- 7 Elsheikh, M. H. *et al.* A review on thermoelectric renewable energy: Principle parameters that affect their performance. *Renewable and Sustainable Energy Reviews* **30**, 337-355 (2014).
- 8 Anton, S. R. & Sodano, H. A. A review of power harvesting using piezoelectric materials (2003–2006). *Smart materials and Structures* **16**, R1 (2007).
- 9 Emilio, M. D. P. *Microelectronic Circuit Design for Energy Harvesting Systems*. (Springer, 2016).
- 10 Wang, Z. L. Triboelectric nanogenerators as new energy technology for self-powered systems and as active mechanical and chemical sensors. *ACS nano* **7**, 9533-9557 (2013).
- 11 Roy, S. C., Varghese, O. K., Paulose, M. & Grimes, C. A. Toward solar fuels: photocatalytic conversion of carbon dioxide to hydrocarbons. *Acs Nano* **4**, 1259-1278 (2010).

- 12 Yang, J., Wang, D., Han, H. & Li, C. Roles of cocatalysts in photocatalysis and photoelectrocatalysis. *Accounts of chemical research* **46**, 1900-1909 (2013).
- 13 Bowen, C. R. *et al.* Pyroelectric materials and devices for energy harvesting applications. *Energy & Environmental Science* **7**, 3836-3856 (2014).
- 14 Bioenergy, I. Bioenergy—a sustainable and reliable energy source. *International Energy Agency Bioenergy, Paris, France* (2009).
- 15 Williams, C. *et al.* Development of an electromagnetic micro-generator. *IEE Proceedings-Circuits, Devices and Systems* **148**, 337-342 (2001).
- 16 Wang, P.-H., Dai, X.-H., Fang, D.-M. & Zhao, X.-L. Design, fabrication and performance of a new vibration-based electromagnetic micro power generator. *Microelectronics Journal* **38**, 1175-1180 (2007).
- 17 Mizuno, M. & Chetwynd, D. G. Investigation of a resonance microgenerator. *Journal of Micromechanics and Microengineering* **13**, 209 (2003).
- 18 Park, K. I. *et al.* Highly - efficient, flexible piezoelectric PZT thin film nanogenerator on plastic substrates. *Advanced materials* **26**, 2514-2520 (2014).
- 19 Park, K.-I. *et al.* Piezoelectric BaTiO₃ thin film nanogenerator on plastic substrates. *Nano letters* **10**, 4939-4943 (2010).
- 20 Roundy, S. & Wright, P. K. A piezoelectric vibration based generator for wireless electronics. *Smart Materials and structures* **13**, 1131 (2004).
- 21 Wang, Z. L. & Song, J. Piezoelectric nanogenerators based on zinc oxide nanowire arrays. *Science* **312**, 242-246 (2006).
- 22 Wang, X., Song, J., Liu, J. & Wang, Z. L. Direct-current nanogenerator driven by ultrasonic waves. *Science* **316**, 102-105 (2007).

- 23 Xu, S. *et al.* Self-powered nanowire devices. *Nature nanotechnology* **5**, 366 (2010).
- 24 Momeni, K., Odegard, G. & Yassar, R. Nanocomposite electrical generator based on piezoelectric zinc oxide nanowires. *Journal of Applied Physics* **108**, 114303 (2010).
- 25 Park, K. I. *et al.* Flexible nanocomposite generator made of BaTiO₃ nanoparticles and graphitic carbons. *Advanced Materials* **24**, 2999-3004 (2012).
- 26 Kim, S. *et al.* Electrochemically driven mechanical energy harvesting. *Nature communications* **7**, 10146 (2016).
- 27 Kim, S. H. *et al.* Harvesting electrical energy from carbon nanotube yarn twist. *Science* **357**, 773-778 (2017).
- 28 Hou, Y. *et al.* Flexible Ionic Diodes for Low - Frequency Mechanical Energy Harvesting. *Advanced Energy Materials* **7** (2017).
- 29 Shao, H., Fang, J., Wang, H., Dai, L. & Lin, T. Polymer - Metal Schottky Contact with Direct - Current Outputs. *Advanced Materials* **28**, 1461-1466 (2016).
- 30 Wang, S., Lin, L. & Wang, Z. L. Triboelectric nanogenerators as self-powered active sensors. *Nano Energy* **11**, 436-462 (2015).
- 31 Wang, Z. L. Triboelectric nanogenerators as new energy technology and self-powered sensors—Principles, problems and perspectives. *Faraday discussions* **176**, 447-458 (2015).
- 32 Zhu, G. *et al.* Toward large-scale energy harvesting by a nanoparticle-enhanced triboelectric nanogenerator. *Nano letters* **13**, 847-853 (2013).
- 33 Wang, S. *et al.* Sliding-triboelectric nanogenerators based on in-plane charge-separation mechanism. *Nano letters* **13**, 2226-2233 (2013).
- 34 Niu, S. *et al.* Theory of sliding - mode triboelectric nanogenerators. *Advanced materials* **25**, 6184-6193 (2013).

- 35 Bai, P. *et al.* Cylindrical rotating triboelectric nanogenerator. *ACS nano* **7**, 6361-6366 (2013).
- 36 Lin, L. *et al.* Segmentally structured disk triboelectric nanogenerator for harvesting rotational mechanical energy. *Nano letters* **13**, 2916-2923 (2013).
- 37 Zhu, G., Chen, J., Zhang, T., Jing, Q. & Wang, Z. L. Radial-arrayed rotary electrification for high performance triboelectric generator. *Nature communications* **5**, 3426 (2014).
- 38 Yang, Y. *et al.* Single-electrode-based sliding triboelectric nanogenerator for self-powered displacement vector sensor system. *Acs Nano* **7**, 7342-7351 (2013).
- 39 Wang, S., Xie, Y., Niu, S., Lin, L. & Wang, Z. L. Freestanding triboelectric - layer - based nanogenerators for harvesting energy from a moving object or human motion in contact and non - contact modes. *Advanced Materials* **26**, 2818-2824 (2014).
- 40 Chen, J. *et al.* Networks of triboelectric nanogenerators for harvesting water wave energy: a potential approach toward blue energy. *ACS nano* **9**, 3324-3331 (2015).
- 41 Wang, Z. L., Jiang, T. & Xu, L. Toward the blue energy dream by triboelectric nanogenerator networks. *Nano Energy* **39**, 9-23 (2017).
- 42 Xi, Y. *et al.* Multifunctional TENG for Blue Energy Scavenging and Self - Powered Wind - Speed Sensor. *Advanced Energy Materials* **7** (2017).
- 43 Wang, X. *et al.* Triboelectric Nanogenerator Based on Fully Enclosed Rolling Spherical Structure for Harvesting Low - Frequency Water Wave Energy. *Advanced Energy Materials* **5** (2015).
- 44 Wen, X., Yang, W., Jing, Q. & Wang, Z. L. Harvesting broadband kinetic impact energy from mechanical triggering/vibration and water waves. *ACS nano* **8**, 7405-7412 (2014).

- 45 Ahmed, A. *et al.* Self - Powered Wireless Sensor Node Enabled by a Duck - Shaped Triboelectric Nanogenerator for Harvesting Water Wave Energy. *Advanced Energy Materials* **7** (2017).
- 46 Xu, L. *et al.* Integrated triboelectric nanogenerator array based on air-driven membrane structures for water wave energy harvesting. *Nano Energy* **31**, 351-358 (2017).
- 47 Zi, Y. *et al.* Triboelectric–pyroelectric–piezoelectric hybrid cell for high - efficiency energy - harvesting and self - powered sensing. *Advanced Materials* **27**, 2340-2347 (2015).
- 48 Yang, Y. *et al.* Silicon-based hybrid energy cell for self-powered electrodegradation and personal electronics. *ACS nano* **7**, 2808-2813 (2013).
- 49 Yang, Y. *et al.* A hybrid energy cell for self-powered water splitting. *Energy & Environmental Science* **6**, 2429-2434 (2013).
- 50 Yang, P.-K. *et al.* based origami triboelectric nanogenerators and self-powered pressure sensors. *ACS nano* **9**, 901-907 (2015).
- 51 Zhang, H. *et al.* Triboelectric nanogenerator for harvesting vibration energy in full space and as self - powered acceleration sensor. *Advanced Functional Materials* **24**, 1401-1407 (2014).
- 52 Chen, J. *et al.* Harmonic - resonator - based triboelectric nanogenerator as a sustainable power source and a self - powered active vibration sensor. *Advanced materials* **25**, 6094-6099 (2013).
- 53 Li, S. *et al.* All-elastomer-based triboelectric nanogenerator as a keyboard cover to harvest typing energy. *ACS nano* **10**, 7973-7981 (2016).

- 54 Lin, Z. H. *et al.* A self - powered triboelectric nanosensor for mercury ion detection. *Angewandte Chemie International Edition* **52**, 5065-5069 (2013).
- 55 Zhang, C. & Wang, Z. L. Tribotronics—A new field by coupling triboelectricity and semiconductor. *Nano Today* **11**, 521-536 (2016).
- 56 Li, A., Zi, Y., Guo, H., Wang, Z. L. & Fernández, F. M. Triboelectric nanogenerators for sensitive nano-coulomb molecular mass spectrometry. *Nature nanotechnology* **12**, 481 (2017).
- 57 Liu, J. *et al.* Direct-current triboelectricity generation by a sliding Schottky nanocontact on MoS₂ multilayers. *Nature nanotechnology* **13**, 112 (2018).
- 58 Lowell, J. & Rose-Innes, A. Contact electrification. *Advances in Physics* **29**, 947-1023 (1980).
- 59 Park, J. Y. & Salmeron, M. Fundamental aspects of energy dissipation in friction. *Chemical reviews* **114**, 677-711 (2013).
- 60 Yoshizawa, H. & Israelachvili, J. Fundamental mechanisms of interfacial friction. 2. Stick-slip friction of spherical and chain molecules. *The Journal of Physical Chemistry* **97**, 11300-11313 (1993).
- 61 Harper, W. R. *Contact and frictional electrification*. (Clarendon Press, 1967).
- 62 Lowell, J. Tunnelling between metals and insulators and its role in contact electrification. *Journal of Physics D: Applied Physics* **12**, 1541 (1979).
- 63 Lee, L.-H. Dual mechanism for metal-polymer contact electrification. *Journal of electrostatics* **32**, 1-29 (1994).

- 64 Apodaca, M. M., Wesson, P. J., Bishop, K. J., Ratner, M. A. & Grzybowski, B. A. Contact electrification between identical materials. *Angewandte Chemie* **122**, 958-961 (2010).
- 65 Sadewasser, S. & Glatzel, T. *Kelvin probe force microscopy: measuring and compensating electrostatic forces*. Vol. 48 (Springer Science & Business Media, 2011).
- 66 Baytekin, H. *et al.* The mosaic of surface charge in contact electrification. *Science* **333**, 308-312 (2011).
- 67 Zhou, Y. S. *et al.* In situ quantitative study of nanoscale triboelectrification and patterning. *Nano letters* **13**, 2771-2776 (2013).
- 68 Zhou, Y. S. *et al.* Manipulating nanoscale contact electrification by an applied electric field. *Nano letters* **14**, 1567-1572 (2014).
- 69 Li, S., Zhou, Y., Zi, Y., Zhang, G. & Wang, Z. L. Excluding contact electrification in surface potential measurement using kelvin probe force microscopy. *ACS nano* **10**, 2528-2535 (2016).
- 70 Lee, K. Y. *et al.* Controllable charge transfer by ferroelectric polarization mediated triboelectricity. *Advanced Functional Materials* **26**, 3067-3073 (2016).
- 71 Popov, V. L. & Gray, J. Prandtl - Tomlinson model: History and applications in friction, plasticity, and nanotechnologies. *ZAMM - Journal of Applied Mathematics and Mechanics/Zeitschrift für Angewandte Mathematik und Mechanik* **92**, 683-708 (2012).
- 72 Persson, B. N. *Sliding friction: physical principles and applications*. (Springer Science & Business Media, 2013).
- 73 Persson, B. & Volokitin, A. Electronic friction of physisorbed molecules. *The Journal of chemical physics* **103**, 8679-8683 (1995).

- 74 Holzzapfel, C., Stubenrauch, F., Schumacher, D. & Otto, A. DC resistivity variation of cold-deposited silver films during gas exposure. *Thin Solid Films* **188**, 7-19 (1990).
- 75 Chabal, Y. Electronic damping of hydrogen vibration on the W (100) surface. *Physical review letters* **55**, 845 (1985).
- 76 Reutt, J., Chabal, Y. & Christman, S. Coupling of H vibration to substrate electronic states in Mo (100)-p (1× 1) H and W (100)-p (1× 1) H: example of strong breakdown of adiabaticity. *Physical Review B* **38**, 3112 (1988).
- 77 Persson, B. & Volokitin, A. Infrared reflection-absorption spectroscopy of dipole-forbidden adsorbate vibrations. *Surface science* **310**, 314-336 (1994).
- 78 Persson, B., Tosatti, E., Fuhrmann, D., Witte, G. & Wöll, C. Low-frequency adsorbate vibrational relaxation and sliding friction. *Physical Review B* **59**, 11777 (1999).
- 79 Witte, G. *et al.* Damping of molecular motion on a solid substrate: evidence for electron-hole pair creation. *Physical review letters* **80**, 121 (1998).
- 80 Stipe, B., Mamin, H., Stowe, T., Kenny, T. & Rugar, D. Noncontact friction and force fluctuations between closely spaced bodies. *Physical review letters* **87**, 096801 (2001).
- 81 Park, J. Y., Qi, Y., Ogletree, D., Thiel, P. A. & Salmeron, M. Influence of carrier density on the friction properties of silicon p n junctions. *Physical Review B* **76**, 064108 (2007).
- 82 Qi, Y., Park, J., Hendriksen, B., Ogletree, D. & Salmeron, M. Electronic contribution to friction on GaAs: An atomic force microscope study. *Physical Review B* **77**, 184105 (2008).
- 83 Tagawa, M., Mori, M., Ohmae, N., Umeno, M. & Takenobu, S. Tribo- and photo-stimulated exoelectron emission from graphite. *Tribology international* **26**, 57-60 (1993).

- 84 Camara, C. G., Escobar, J. V., Hird, J. R. & Putterman, S. J. Correlation between nanosecond X-ray flashes and stick–slip friction in peeling tape. *nature* **455**, 1089 (2008).
- 85 Burton, B., Kang, S., Rhee, S. & George, S. SiO₂ atomic layer deposition using tris (dimethylamino) silane and hydrogen peroxide studied by in situ transmission FTIR spectroscopy. *The Journal of Physical Chemistry C* **113**, 8249-8257 (2009).
- 86 Loh, T. A. & Chua, D. H. Growth mechanism of pulsed laser fabricated few-layer MoS₂ on metal substrates. *ACS applied materials & interfaces* **6**, 15966-15971 (2014).
- 87 Bara, C. *et al.* Surface Science Approaches for the Preparation of Alumina - Supported Hydrotreating Catalysts. *ChemCatChem* **7**, 3422-3440 (2015).
- 88 Bara, C. d. *et al.* Aqueous-Phase Preparation of Model HDS Catalysts on Planar Alumina Substrates: Support Effect on Mo Adsorption and Sulfidation. *Journal of the American Chemical Society* **137**, 15915-15928 (2015).
- 89 Late, D. J. *et al.* Pulsed laser-deposited MoS₂ thin films on W and Si: field emission and photoresponse studies. *ACS applied materials & interfaces* **6**, 15881-15888 (2014).
- 90 Pittenger, B., Erina, N. & Su, C. (Santa Barbara, CA: Bruker Corporation, 2012).
- 91 Zhang, C. *et al.* Rotating - Disk - Based Direct - Current Triboelectric Nanogenerator. *Advanced Energy Materials* **4** (2014).
- 92 Yang, Y., Zhang, H. & Wang, Z. L. Direct - Current Triboelectric Generator. *Advanced Functional Materials* **24**, 3745-3750 (2014).
- 93 Goswami, A. *et al.* Effect of interface on mid-infrared photothermal response of MoS₂ thin film grown by pulsed laser deposition. *Nano Research*, 1-14 (2016).
- 94 Zeng, H., Dai, J., Yao, W., Xiao, D. & Cui, X. Valley polarization in MoS₂ monolayers by optical pumping. *Nature nanotechnology* **7**, 490-493 (2012).

- 95 Lopez-Sanchez, O., Lembke, D., Kayci, M., Radenovic, A. & Kis, A. Ultrasensitive photodetectors based on monolayer MoS₂. *Nature nanotechnology* **8**, 497-501 (2013).
- 96 Karunadasa, H. I. *et al.* A molecular MoS₂ edge site mimic for catalytic hydrogen generation. *Science* **335**, 698-702 (2012).
- 97 Winer, W. Molybdenum disulfide as a lubricant: a review of the fundamental knowledge. *Wear* **10**, 422-452 (1967).
- 98 Chhowalla, M. & Amaratunga, G. A. Thin films of fullerene-like MoS₂ nanoparticles with ultra-low friction and wear. *Nature* **407**, 164-167 (2000).
- 99 Wang, S. *et al.* Shape evolution of monolayer MoS₂ crystals grown by chemical vapor deposition. *Chemistry of Materials* **26**, 6371-6379 (2014).
- 100 Kraya, R., Kraya, L. Y. & Bonnell, D. A. Orientation controlled Schottky barrier formation at Au nanoparticle– SrTiO₃ interfaces. *Nano letters* **10**, 1224-1228 (2010).
- 101 Dai, L. *et al.* Influence of electronic transmission on the electrical transport properties in metal–semiconductor contacts. *physica status solidi (a)* **212**, 2791-2797 (2015).
- 102 Reid, O. G., Munechika, K. & Ginger, D. S. Space charge limited current measurements on conjugated polymer films using conductive atomic force microscopy. *Nano letters* **8**, 1602-1609 (2008).
- 103 Alexe, M. & Hesse, D. Tip-enhanced photovoltaic effects in bismuth ferrite. *Nature Communications* **2**, 256 (2011).
- 104 Gong, C., Colombo, L., Wallace, R. M. & Cho, K. The unusual mechanism of partial Fermi level pinning at metal–MoS₂ interfaces. *Nano letters* **14**, 1714-1720 (2014).

- 105 Butt, H.-J., Cappella, B. & Kappell, M. Force measurements with the atomic force microscope: Technique, interpretation and applications. *Surface science reports* **59**, 1-152 (2005).
- 106 Hoh, J. H. & Engel, A. Friction effects on force measurements with an atomic force microscope. *Langmuir* **9**, 3310-3312 (1993).
- 107 Zhu, H. *et al.* Observation of piezoelectricity in free-standing monolayer MoS₂. *Nature nanotechnology* **10**, 151-155 (2015).
- 108 Sun, C.-H., Linn, N. C. & Jiang, P. Templated fabrication of periodic metallic nanopillar arrays. *Chemistry of Materials* **19**, 4551-4556 (2007).
- 109 Wang, Z. L. Self - Powered Nanosensors and Nanosystems. *Adv. Mater.* **24**, 280-285 (2012).
- 110 Wang, Z. L., Chen, J. & Lin, L. Progress in triboelectric nanogenerators as a new energy technology and self-powered sensors. *Energy Environ Sci.* **8**, 2250-2282 (2015).
- 111 Wang, Z. L., Lin, L., Chen, J., Niu, S. & Zi, Y. *Triboelectric Nanogenerators*. (Springer, 2016).
- 112 Liu, J. *et al.* Direct-current triboelectricity generation by sliding-Schottky nanocontact on MoS₂ multilayers. *Nature Nanotechnology*, doi:10.1038/s41565-017-0019-5 (2017).
- 113 Shao, H., Fang, J., Wang, H., Zhou, H. & Lin, T. Direct current energy generators from a conducting polymer–inorganic oxide junction. *Journal of Materials Chemistry A* **5**, 8267-8273 (2017).
- 114 O'Mara, W., Herring, R. B. & Hunt, L. P. *Handbook of semiconductor silicon technology*. (Crest Publishing House, 2007).

- 115 Cheng, Y. Electronic states at the silicon-silicon dioxide interface. *Prog. Surf. Sci.* **8**, 181-218 (1977).
- 116 Hu, Y. & Wang, Z. L. Recent progress in piezoelectric nanogenerators as a sustainable power source in self-powered systems and active sensors. *Nano Energy* **14**, 3-14 (2015).
- 117 Chiu, F.-C. A review on conduction mechanisms in dielectric films. *Advances in Materials Science and Engineering* **2014** (2014).
- 118 Sze, S. M. & Ng, K. K. Metal - semiconductor contacts. *Physics of semiconductor devices*, 134-196 (2006).
- 119 Paranthaman, M. P., Wong-Ng, W. & Bhattacharya, R. N. *Semiconductor materials for solar photovoltaic cells*. Vol. 218 (Springer, 2015).
- 120 Rankin, D. W. (Taylor & Francis, 2009).
- 121 Bardeen, J. Surface states and rectification at a metal semi-conductor contact. *Phys. Rev.* **71**, 717 (1947).
- 122 Rowe, D. M. *Thermoelectrics handbook: macro to nano*. (CRC press, 2005).
- 123 Meyer, E., Hug, H. J. & Bennewitz, R. *Scanning probe microscopy: the lab on a tip*. (Springer Science & Business Media, 2013).
- 124 Alexe, M. & Hesse, D. Tip-enhanced photovoltaic effects in bismuth ferrite. *Nature Communications* **2**, ncomms1261 (2011).